Development of Innovative Thermal-Insulating and Sound-Absorbing Porous Materials by Materials Model-Based Research (MBR)

（材料 MBR 技術を活用した革新的断熱吸音多孔質部材の開発）

September, 2024

Daiji Katsura

Hiroshima University

Contents

Chapter 1: Introduction

1.   Thermal management and noise control required for automobiles

The automobile is undergoing a major transformation to address critical issues affecting consumers, the global environment, and society. One of the most important challenges is carbon neutral (CN) compliance. To address this issue, innovative technologies for automobile drive sources are being developed, including electrification, alternative fuel technologies for internal combustion engines, and CO_2 capture technologies. In particular, the international market for battery electric vehicles (BEVs) has expanded rapidly in recent years and is projected to grow at a CAGR of approximately 32.5% from 2021 to 2028 [1].

In general, the input/output power and service life of drive batteries for BEVs are highly dependent on temperature and state of charge. If the temperature is outside the appropriate range, not only will the life of the battery be shortened and the charging time lengthened, but the output of the drive motor and the amount of regenerative power generation will also decrease, affecting the driving appeal and cruising range. Strict temperature control of the drive battery is very important for BEVs from the three viewpoints of "using all available input/output power," "stabilizing available input/output power," and "compensating for low available input/output power" [2-3]. Other factors reported by Johnson and Li et al. to have the greatest impact on energy efficiency consumed during driving are internal air conditioning [4-5]. The use of in-vehicle air conditioning increases energy use by an average of 9% per year (at an average annual temperature of 15°C, using Tokyo temperature data), regardless of drive type, such as BEVs, fuel cell vehicles (FCVs), hybrid vehicles (HEVs), and internal combustion engine vehicles (ICEVs) [6-7]. BEVs are severely adversely affected by both battery temperature and cabin air conditioning during the winter months, resulting in significantly reduced range [5]. The importance of thermal management is not limited to BEVs. Since the

combustion efficiency of ICEs has improved significantly in recent years, less thermal energy is available for warming up in winter, and how to effectively utilize the limited thermal energy is an important point [8-9]. Warming increases the cooling water temperature and brings the engine and transmission to the proper temperature, thereby maintaining combustion conditions and oil viscosity for good fuel economy. It also supplies the energy required from the air conditioning to the heater core for heating via the cooling water. There are four perspectives in these thermal management: "Bringing the optimum temperature closer to the ambient temperature, expanding the range of optimum temperatures (relaxing requirements)", "Shorten the time required to reach the optimum temperature (concentration of energy, reduction of thermal capacity)", " Reduce energy loss required to maintain the optimum temperature during operation (thermal insulation)," and "Maintaining the proper temperature from the time of shutdown to the time of restart (heat retention)". Porous thermal-insulating material is used to improve the latter two of these.

Also, BEVs generally weigh significantly more than HEVs and ICEVs in the same class category because of the drive battery. In addition, the absence of engine noise makes road noise generated during driving noticeable as a grating sound from low-speed range [10-11]. PHEVs equipped with an ICE as a generator are required to operate widely in EV driving mode by minimizing the frequency of ICE operation (power generation time) in hybrid driving mode after the battery charge level drops. To achieve this, the amount of electricity generated at one time should be large, but the higher the power generation output, the louder the sound during power generation becomes, resulting in inconsistency with the driving noise predicted by the driver from the vehicle speed, which becomes noticeable as a grating sound [12]. In ICEVs, a new combustion (Spark Controlled Compression Ignition, SPCCI) technology has been developed to control compression auto-ignition by spark ignition propagation combustion to significantly improve torque and combustion efficiency [13-14]. Compared to conventional spark ignition combustion (Spark Ignition Combustion, SI), SPCCI combustion has a

shorter combustion period and a steeper heat generation rate slope. In general, such combustion produces an impulsive blow to the piston and intermittent combustion noise [15]. The radiated combustion noise propagates from the engine compartment to the interior of the vehicle and becomes noticeable as a grating sound when louder than the driving noise [16]. As a countermeasure against these noises, porous sound-absorbing materials have been used to reduce the grating sound by placing them near the sound source or inside the vehicle cabin [16-20].

However, it is difficult to meet all of these requirements in the limited space of a car, and porous materials with both high thermal insulation and high sound absorption properties are required.

2. Sound absorption and thermal insulation mechanism of porous materials

The sound absorption coefficient is a key indicator of the performance of sound-absorbing materials. As shown in **Figure 1-1a**, a porous sound-absorbing material absorbs sound by converting the energy of sound waves entering the material into thermal energy through viscoelastic damping in the solid phase and through viscous damping and heat dissipation at the boundary between the fluid and solid phases. Therefore, it is recognized that the sound absorption coefficient of a sound-absorbing material depends on the structure inside the material [21-25]. Specifically, to improve viscoelastic damping in solids, the loss factor of the solid should be increased, or the solid should be more easily distorted. Furthermore, to improve viscous damping and heat dissipation at the boundary between gas and solid, the boundary area between gas and solid should be increased, or the path of the gas through which sound waves pass should be lengthened. Increasing the boundary area between gas and solid inside the material or lengthening the path of the gas makes it more difficult for sound waves to penetrate the material. Balancing the two, the diameter of porosity and bubbles should be reduced from tens of micrometers to several millimeters in diameter, and each space should be connected to form a flow path for sound waves to pass through.

3

On the other hand, thermal conductivity is a key indicator of the performance of thermal-insulating materials. As shown in **Figure 1-1b**, a porous thermal-insulating material insulates by decreasing contributions from the heat propagation paths inside the material: heat conduction in the solid and fluid phases, heat radiation, and heat convection. Therefore, it is recognized that, as with sound-absorbing material, the thermal conductivity of a thermal-insulating material depends on the structure inside the material [26-28]. Specifically, the porosity or bubble ratio should be increased to reduce heat conduction in solids, or heat conduction path of solids should be lengthened. Furthermore, to reduce heat conduction in gases, heat conduction in gases, and heat radiation, the diameter of porosity and bubbles should be reduced from tens of nanometers to tens of micrometers, or each space should be made independent of the other. Thus, in general, high-performance porous thermal-insulating materials do not function as sound absorbers because they do not have channels through which sound waves can pass, or the spaces in the fluid phase are too minute for sound waves to penetrate. Therefore, achieving both high sound absorption and high thermal insulation in the same material using the conventional approach is difficult.
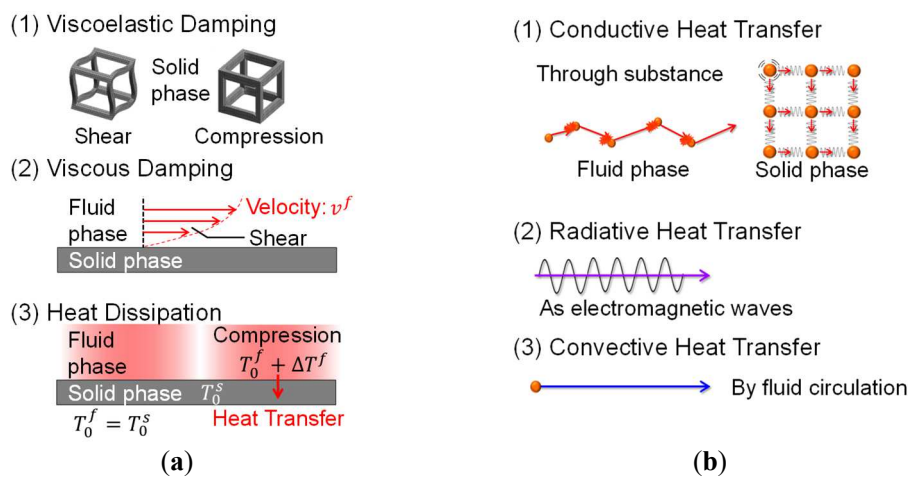
Figure 1-1. Mechanisms inside porous materials: (a) sound absorption and (b) heat transfer.

In recent years, experimental studies have been conducted on nanofiber-based composite materials that achieve both thermal and acoustic properties: Polyvinylidene fluoride by Wu et al. (2016) [29], cellulose by Shen et al. (2021) [30], polyurethane by Zhao et al. (2021) [31], thermoplastic polyurethane (TPU)/polystyrene (PS) by Karaca et al. (2022) [32], polyacrylonitrile (PAN) by Farahani et al. (2022) [33], and other materials have been studied. For example, a study by Karaca et al. on TPU/PS-BSE nanofibers prepared using electrospinning solutions [32] showed that they achieve both 0.050 W/(m·K) as thermal conductivity and 0.5–0.6 as the sound absorption coefficient at about 1000 Hz. Experimental studies have also been conducted on silica aerogel-based materials that achieve both thermal and acoustic properties. With regard to silica and silica–polymer hybrid aerogels, polyimide–silica aerogel composites by Yan et al. (2014) [34], sodium dodecyl sulfate-doped gelatin–silica hybrid aerogels by Sachithanadam et al. (2016) [35], monolithic aerogels and granular aerogels by Merli et al. (2018) [36], and other materials have been studied. With regard to silica aerogel–textiles composites, non-woven polyethylene terephthalate (PET)–silica aerogel blankets by Oh et al. (2009) [37], non-woven PET–aerogel composites by Küçük et al. (2012) [38], cotton non-woven fabric–silica aerogel blanket by Motahari et al. (2015) [39], silica aerogel blanket prepared from sols with varying silica content by Ramamoorthy et al. (2017) [40], aerogel–polyethylene (PE)/PET non-woven bonded blankets by Yang et al. (2019) [41], in situ synthetic silica aerogel/PET blankets by Talebi et al. (2019) [42], glass fiber blankets impregnated with aerogel powder (2–40 μm particle size) by Zahra et al. (2021) [43], and other materials have been studied. For example, a study by Zahra et al. on glass fiber blankets impregnated with aerogel powder [43] showed that the sound absorption coefficient above 1000 Hz can only reach about 0.4 at a thickness of 10 mm.

Therefore, the author aimed to realize a new organic-inorganic composite porous material that combines high sound absorption in the frequency range above 1000 Hz (sound absorption coefficient of above 0.5) and high thermal insulation equivalent to still air (0.026 W/(m·K)).

3. Visualization of 3D microstructures in porous materials

As shown in Section 2, it is recognized that both sound absorption and thermal conductivity depend on the internal structure of the material. Therefore, it is very important to visualize the 3D microstructures in porous materials and to quantitatively analyze the characteristics of the structure to develop porous materials that exhibit excellent sound absorption and thermal insulation properties.

X-ray computed tomography (CT) is a powerful technique for visualizing internal 3D microstructures in materials. It is extensively used to generate high-resolution CT images of inorganic materials that absorb X-ray efficiently. X-ray CT has been also used for organic polymeric materials even though these materials poorly absorb X-ray [44]. For instance, Garcea et al. described that the challenge for 3D imaging techniques of polymer composites with high resolution and high contrast. [45]. Using X-ray CT, Takahashi and coworkers acquired cross-sectional images of unidirectional carbon fiber-reinforced plastics to determine fiber positions [46]. Zwanenburg et al. reported the X-ray CT imaging of carbon fiber composite materials under optimized conditions [47]. Because organic polymers are composed of light elements with weak X-ray absorption (carbon, hydrogen, and oxygen), their CT images often have low contrast. Consequently, numerous approaches have been developed to enhance the contrast of X-ray CT images for organic polymers [48]. The incorporation of established X-ray contrast agents such as $BaCl_2$ and $AgNO_3$ into polymers is a well-known strategy for boosting X-ray CT image contrast. Hexamethyldisilazane is also employed as a convenient contrast reagent that readily reacts with OH groups to form $O-SiMe_3$ bonds. This substitution introduces relatively heavy silicon atoms, enhancing CT image contrast. However, these contrast agents are applicable only to polymers with suitable coordination or reaction sites, such as chitin, gelatin/poly(vinyl alcohol) composites, and polyacrylamide, but not to polymers such as poly(ethylene terephthalate) (PET) and polypropylene (PP), which lack the necessary interaction sites. It was also reported that nanoparticles prepared by cross-linking iodine-containing iohexol with hexamethylene diisocyanate coprecipitated

with mPEG-polylactide to enhance the CT contrast [49]. Lex et al. demonstrated the synthesis of iodine-containing polyesters exhibiting high X-ray CT image contrast via ring-opening polymerization of iodine-containing cyclic monomers and verified their potential as bioimaging contrast agents [50]. However, for widely used polymers lacking suitable interaction sites, effective methods for enhancing their CT images remain elusive. Physically adsorbed contrast agents such as iodine-containing sodium diatrizoate hydrate and KI in aqueous media offer limited applicability as they are effective primarily for porous materials [51]. Mixing organic polymer materials with heavy element salts like $BaSO_4$ or Bi(III) in the molding process has been explored [52-54]. Nonetheless, the tendency of these inorganic salts to aggregate within nonpolar organic polymers hinders homogeneous X-ray CT image contrast enhancement.

Gamma-ray irradiation is a well-established method for inducing radical graft polymerization in organic polymers [55–60]. This approach has been successfully applied, for instance, in the grafting of polystyrene onto PET via gamma irradiation in dichloromethane. The process, initiated by gamma-ray-induced radical formation on the ethylene carbon of PET, enables grafting even for solid PET materials [56, 59, 60]. Grafting acrylate on PET films or resin granules by gamma-ray irradiation has also been reported [58, 61].

Therefore, the author aimed to obtain high-contrast CT images by inducing radical graft polymerization in organic polymers by gamma-ray irradiation.

4. Computational microstructure modeling approach applied to sound-absorbing Porous Materials

As shown in Section 2, both sound absorption coefficient and thermal conductivity depend on the internal structure of the material, but the structure required for high performance is different for each. Therefore, it has been difficult to achieve both high sound absorption and high thermal insulation

with the same material using conventional trial-and-error research and development methods. To break through the inconsistent efficiently and effectively, it is important to predict and calculate the sound absorption coefficient and thermal conductivity of a porous material based on the three-dimensional microstructure inside the material. In particular, the sound absorption coefficient has no linear relationship with the shape and thickness of the product when it is made into a product, and it is very difficult to study the product performance, so the predictive calculation is even more important.

Various studies have been conducted on methods to predict the dynamic properties of porous sound absorbers. Recently, Kang and Bolton [62], Easwaran [63] et al. or Attala et al. [64] have proposed finite element analysis methods, which allow numerical analysis considering arbitrary shapes and boundary conditions. In all of these studies, the model proposed by Biot [65, 66] was applied. Biot's model was initially proposed to describe the dynamic properties of soils and bedrock, where solid and fluid phases are mixed. Each phase is modeled using macroscopic properties, with the solid phase represented by linear elasticity and the fluid phase by viscous fluid properties. Since the medium of the fluid phase was assumed to be liquid, only viscous damping was considered as a property. However, models have been proposed by Johnson [67], Champoux [68], and Allard et al [69] that also consider attenuation due to heat dissipation so that it can be applied when the medium is gas. This model is currently often applied to porous sound-absorbing materials. However, in Biot's model, the properties of the fluid phase are derived based on a theoretical solution for the behavior of a viscous fluid in a microcircular tube, which lacks mathematical rigor when expanded to channels with arbitrary cross-sectional shapes. In addition, the nine macro parameters included in the Biot model, such as flow resistance, must currently be identified by experimentation. On the other hand, studies have been conducted to apply the homogenization method to the microstructure of porous materials and to derive equivalent property values at the macro scale. For example, for the problem of seepage flow, Auliault et al [70] derived macroscopic permeability coefficients for the case where the solid phase of a porous

material is rigid-walled, and confirmed them experimentally. Terada et al [71] also formulated the system as a coupled solid and fluid phase system. Burridge et al [72] derived equivalent property values at the macro scale from equilibrium and constitutive equations at the micro scale for porous sound absorbers and compared them to the property values in Biot's model. However, it does not consider the decay of heat generated in the fluid phase due to dissipation to the solid phase, and the volumetric modulus, one of the properties of the fluid phase, is evaluated larger than it actually is.

Therefore, as suggested by Yamamoto et al [73], the author applies the asymptotic expansion homogenization method to the microstructure of porous sound absorbers, considering both viscosity in the fluid phase and attenuation due to heat dissipation. And directly obtains the equivalent properties necessary to predict the dynamic properties of porous sound absorbers from the microstructures. By applying the equivalent properties obtained here to a model of porous sound absorbing material, macroscopic properties such as sound absorption coefficient can be obtained [74]. The Biot parameters can be identified from the obtained macro properties, and the optimal design of the microstructure can be performed by relating the Biot parameters to dimensional parameters that characterize the microstructure, such as pore diameter, fiber diameter, and fiber-to-fiber distance [75]. Furthermore, the mechanism of sound absorption can be clarified by analytically determining each dissipated energy using the theoretical solution of the wave equation for sound waves propagating in a one-dimensional tube, limited to the case of normal-incidence sound absorption coefficient [76].

5.   Overview of this thesis

In this thesis, by utilizing the fundamental technologies shown in Sections 3 and 4 of Chapter 1, the author efficiently developed a high-performance thermal-insulating and sound-absorbing porous material with the target performance shown in Section 2 of Chapter 1. This modeling approach (**Figure 1-2**), in which materials with the targeted performance are efficiently developed by backcasting from

the required functions of the product and by predictive calculation of the microstructure inside the material, is called materials model-based research (MBR) [77-80].

High-performance thermal insulation porous materials require the space of the fluid phase to be narrow to suppress heat conduction in gases. On the other hand, the fluid phase space is too narrow for sound waves to penetrate, so it cannot function as a sound-absorbing material. Therefore, the author considered and confirmed a structure in which sound waves do not need to penetrate the porous material, and sound absorption occurs only when sound waves collide with the porous material. The author also divided the space inside the porous material into two spaces, one where sound waves cannot penetrate and the other where sound waves can penetrate, and developed a structure that creates thermal insulation properties in the space where sound waves cannot penetrate and sound absorption properties by complicating the paths in the space where sound waves can penetrate. Furthermore, the author considered and confirmed a structure that improves sound absorption by controlling the flow resistance of sound waves on the surface of the porous material.
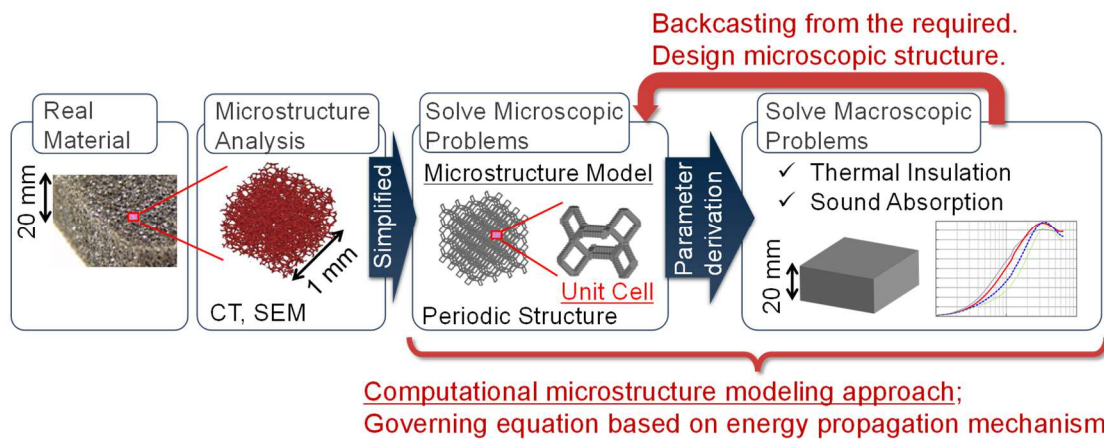
Figure 1-2. Development of high-performance multifunctional materials using materials model-based research.

Chapter 2 describes a new method to enhance the contrast of X-ray CT images of organic polymer materials. The author demonstrates that gamma-ray irradiation of poly (ethylene terephthalate) (PET) fibers in dichloromethane containing 2-bromoethyl methacrylate, 2-chloroethyl methacrylate, or 4-bromostyrene results in the grafting of halogen-containing oligomeric chains onto the PET fibers (**Figure 1-3**). Focused ion beam scanning electron microscopy (FIB-SEM) and time-of-flight secondary ion mass spectrometry (TOF-SIMS) analyses revealed a homogeneous distribution of bromine atoms within the 2-bromoethyl methacrylate-modified PET fibers, not only on the surface. This uniform incorporation translated to a significant improvement in X-ray CT image contrast compared with pristine fibers. Similar treatment of polypropylene pellets also enhanced the contrast of their X-ray CT images. This is a new simple and effective method to enhance the X-ray CT image contrast and potentially applicable to various polymer materials including polymer composites and porous polymer materials, readily allowing the observation of their 3D microstructures finely.

Figure 1-3. Radical graft polymerization of styrene onto PET by gamma-ray irradiation.

Chapter 3 describes a hydrophobic cellulose nanofiber–poly(methylsiloxane) xerogel composite developed using computational microstructure modeling. By applying computational microstructure modeling to porous materials, the sound absorption performance can be improved by increasing the resonance amplitude of the ligament (solid phases) and amplifying the viscous damping at the

boundary between the fluid and solid phases, thereby verifying the concept of a sound absorption mechanism without sound wave penetration (**Figure 1-4**). The porous material was found to have both high sound absorption in the frequency range above 1000 Hz (sound absorption coefficient of above 0.44) and high thermal insulation equivalent to still air (0.026 W/(m·K)).

(a)   (b)

(c)
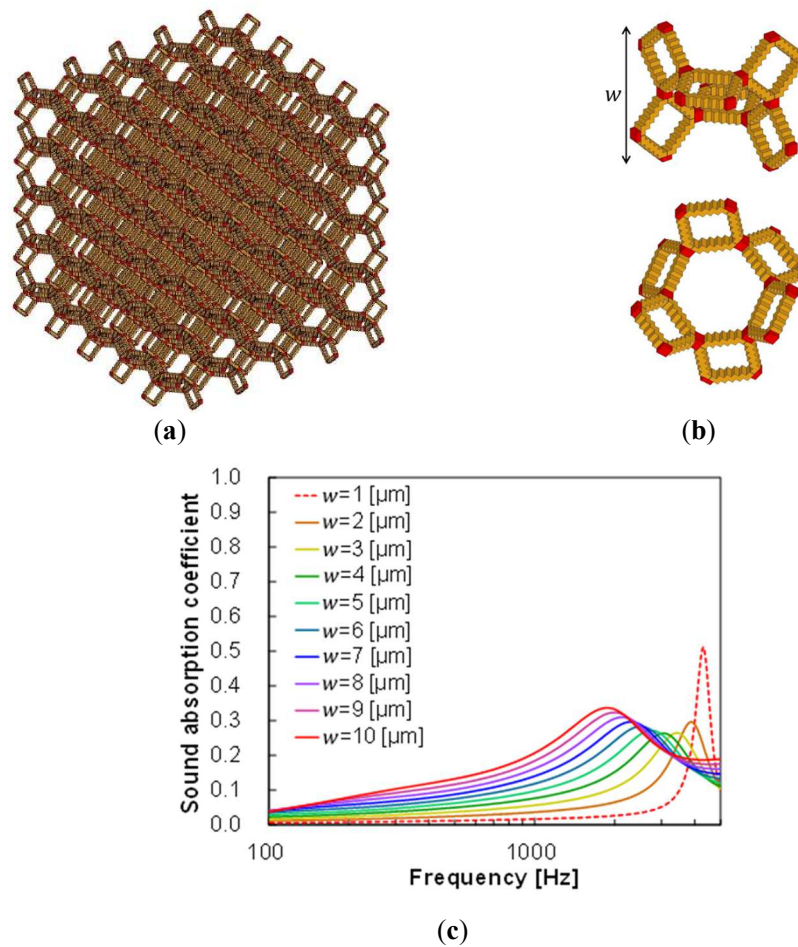
Figure 1-4. Calculation model of the microstructure of simulated porous material: (a) periodic structure; (b) unit cell and (c) Spectra of predicted sound absorption coefficients of simulated porous material.

Chapter 4 describes a non-woven fabric composed of flattened ellipsoidal particles with nano-porosity developed using computational microstructure modeling. In this material, the thermal

insulation property was created by particles with nano-porosity through which sound waves cannot penetrate, and the sound absorption property was created by making other spaces where sound waves can penetrate. By making the particles flat, the path of the space through which sound waves can penetrate is extended in a complex manner, thereby improving sound absorption. This mechanism was confirmed by applying computational microstructure modeling to porous materials and changing the shape of the composite particles (**Figure 1-5** and **1-6**). This porous material was found to have both high sound absorption in the frequency range above 1000 Hz (sound absorption coefficient of above 0.35) and high thermal insulation equivalent to still air (0.026 W/(m·K)). Furthermore, it was confirmed that the sound absorption coefficient was improved by laminating this porous material with a high-airflow-resistance skin material (thickness: 0.20 mm) [81], developed jointly with MAEDAKOSEN CO., LTD. (**Figure 1-7**). This porous material laminated with the high-airflow-resistance skin material was found to have both high sound absorption in the frequency range above 1000 Hz (sound absorption coefficient of above 0.5) and high thermal insulation equivalent to still air (0.026 W/(m·K)), achieving the target performance shown in Section 2.

Finally, in Chapter 6, the conclusions of this thesis are described.

| **(a)** | **(b)** | **(c)** |
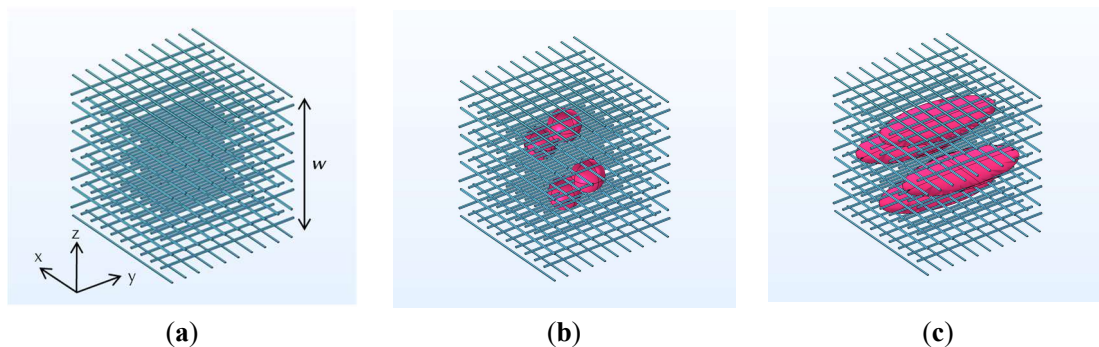
Figure 1-5. Computational geometry: (a) non-woven fabric; (b) composite 1 (spherical particles mixed non-woven fabric) and (c) composite 2 (flattened ellipsoidal particles mixed non-woven fabric).
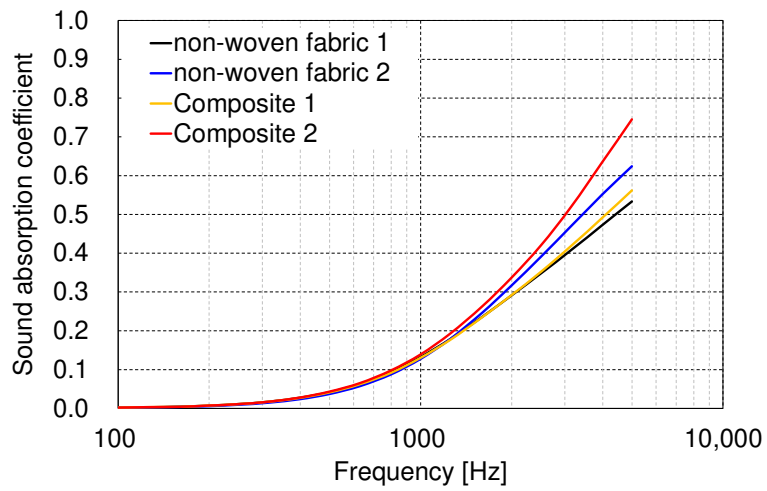
Figure 1-6. Spectra of predicted sound absorption coefficients of the computational geometry.
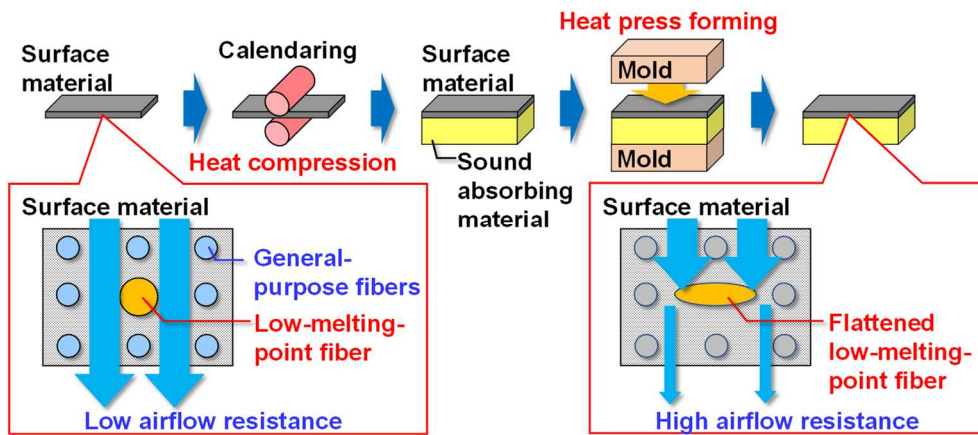
Figure 1-7. High-airflow-resistance skin material laminated to this porous material.

6. References

[1] Electric Passenger Cars Market Size, Share & trends analysis report by product (battery electric vehicle, plug-in hybrid electric vehicle), by region, and segment forecasts, 2021-2028. Accessed on July 2022.

[2] A. Hashizaka; N. Wakayama; K. Ezumi; K. Tanaka; N. Tsukamoto; K. Okada. Maximizing Battery Performance for BEVs. Mazda technical review. 2021, No.38, 32-37.

[3] K. Oji; S. Tomioka; A. Yoshimoto; T. Yasunaga; A. Shoji; H. Fujita. Development of LIB Internal Thermal Modeling Technology. Mazda technical review. 2023, No.40, 130-136.

[4] Johnson, V. H. Fuel Used for Vehicle Air Conditioning: A State-by-State Thermal Comfort-Based Approach. SAE Technical Paper. 2002, No. 2002-01-1957.

[5] Wen Li; Patrick Stanula; Patricia Egede; Sami Kara; Christoph Herrmann. Determining the Main Factors Influencing the Energy Consumption of Electric Vehicles in the Usage Phase. Procedia CIRP. 2016, 48, 352-357.

[6] Keita ISHIZAKI; Masaru NAKANO. The environmental performance of current mass-produced passenger vehicles in Japan. Transactions of the JSME. 2018, Vol.84, No.866.

[7] Keita ISHIZAKI; Masaru NAKANO. A comparative LCCO$_2$ emissions analysis of mass-produced ICEV, HEV, BEV and FCV with the use of HVAC system. Manufacturing Systems Division Conference. 2018, (0), 306.

[8] R. Yamamoto; H. Yokohata; H. Tsunoda; K. Marui; E. Wada; S. Sumi. Simulation Technique of Cylinder Wall Temperature to Apply for High Thermal Efficiency Combustion Development. Mazda technical review. 2018, No.35, 9-14.

[9] M. Koutoku; M. Hayakawa; K. Miyamoto; T. Ishihara; K. Okamura; K. Sugasaki; S. Hikitani; T. Takahata. Thermal Management Technology for SKYACTIV-X. Mazda technical review. 2019, No.36, 32-37.

[10] Antonio Pascale; Simona Mancini; Eloísa Macedo; Paulo Fernandes; Margarida C. Coelho; Claudio Guarnaccia. Single vehicles' noise emission curves analysis by means of first and second derivatives. Applied Acoustics. Volume 211, August 2023, 109526.

[11] M. Yamada; Y. Matsuda; H. Kubota; T. Zenitani; M. Morimoto; N. Mitsuishi; H. Goto. Development of BEV Model and B Pillarless Body Structure for All-New Mazda MX-30. Mazda technical review. 2021, No.38, 57-61.

[12] T. Kawada; Y. Soeda; I. Edahiro; T. Shiraishi; S. Mitsunaga. Powertrain Control for MX-30 Rotary-EV. Mazda technical review. 2023, No.40, 66-69.

[13] R. Isobe; K. Endo; M. Sueoka. New-Generation Gasoline Engine "SKYACTIV-X". Mazda technical review. 2019, No.36, 16-23.

[14] T. Urushihara; K. Matsumoto; M. Sueoka; A. Inoue; K. Maruyama; N. Yamaguchi; H. Morimoto; Y. Matsuo. The Combustion Technology Enabling the SKYACTIV-X Performance. Mazda technical

review. 2019, No.36, 24-31.

[15] Gen Shibata; Koki Ishi; Hirooki Ushijima; Yushi Shibaike; Hideyuki Ogawa; David E. Foster. Optimization of Heat Release Shape and the Connecting Rod Crank Radius Ratio for Low Engine Noise and High Thermal Efficiency of Premixed Diesel Engine Combustion. SAE Paper. 2015, 2015-01-0825.

[16] Y. Kanda; S. Fujikawa; T. Masuoka; Y. Sudo; M. Nitta; T. Yamamoto; M. Matsumoto. Innovative NVH Technology for SKYACTIV-X. Mazda technical review. 2019, No.36, 38-43.

[17] H. Yamamoto; K. Suekuni. Development of Sound Insulation Performance and Lightweight Technology for New Roadster. Mazda technical review. 2015, No.32, 154-157.

[18] K. Shimizu; D. Kusuki; K. Kumamoto; M. Awane; H. Nakayama; K. Yamamoto. Quietness Development for New CX-9. Mazda technical review. 2016, No.33, 33-38.

[19] K. Nagamoto; T. Katsuragawa; M. Awane; T. Fujita. Quietness Development for All-New CX-5. Mazda technical review. 2017, No.34, 20-24.

[20] K. Mutsura; K. Wakamatsu; H. Yamanaka; K. Hirao; T. Nishijima; Y. Teshima. Development of Sound for All-New Mazda3. Mazda technical review. 2019, No.36, 119-124.

[21] Shrestha, S.S.; Tiwari, J.; Rai, A.; Hun, D.E.; Howard, D.; Desjarlais, A.O.; Francoeur, M.; Feng, T. Solid and gas thermal conductivity models improvement and validation in various porous insulation materials. Int. J. Therm. Sci. 2023, 187, 108164.

[22] Zhou, Y.; Huang, B.; Cao, B.-Y. Vibrational modes with long mean free path and large volumetric heat capacity drive higher thermal conductivity in amorphous zeolitic imidazolate Framework-4. Mater. Today Phys. 2021, 21, 100516.

[23] Qiu, B.; Bao, H.; Zhang, G.; Wu, Y.; Ruan, X. Molecular dynamics simulations of lattice thermal conductivity and spectral phonon mean free path of PbTe: Bulk and nanostructures. Comput. Mater. Sci. 2012, 53, 278–285.

[24] Gao, K.; van Dommelen, J.A.W.; Geers, M.G.D. Investigation of the effects of the microstructure on the sound absorption performance of polymer foams using a computational homogenization approach. Eur. J. Mech. A Solids 2017, 61, 330–344.

[25] Gao, K.; van Dommelen, J.A.W.; Göransson, P.; Geers, M.G.D. A homogenization approach for characterization of the fluid–solid coupling parameters in Biot's equations for acoustic poroelastic materials. J. Sound. Vib. 2015, 351, 251–267.

[26] Zieliński, T.G. Microstructure-based calculations and experimental results for sound absorbing porous layers of randomly packed rigid spherical beads. J. Appl. Phys. 2014, 116. https://doi.org/10.1063/1.4890218.

[27] Perrot, C.; Chevillotte, F.; Tan Hoang, M.; Bonnet, G.; Bécot, F.-X.; Gautron, L.; Duval, A. Microstructure, transport, and acoustic properties of open-cell foam samples: Experiments and three-dimensional numerical simulations. J. Appl. Phys. 2012, 111. https://doi.org/10.1063/1.3673523.

[28] Lee, C.-Y.; Leamy, M.J.; Nadler, J.H. Frequency band structure and absorption predictions for multi-periodic acoustic com-posites. J. Sound. Vib. 2010, 329, 1809–1822.

[29] Wu, C.M.; Chou, M.H. Polymorphism, piezoelectricity and sound absorption of electrospun PVDF membranes with and without carbon nanotubes. Compos. Sci. Technol. 2016, 127, 127–133.

[30] Shen, L.; Zhang, H.; Lei, Y.; Chen, Y.; Liang, M.; Zou, H. Hierarchical pore structure based on cellulose nanofiber/melamine composite foam with enhanced sound absorption performance. Carbohydr. Polym. 2021, 255, 117405.

[31] Zhao-Xuan, D.; Ying, W. Optimization and characterization of polyurethane electro-spun nano-membranes used for the surfaces of sound absorbent multi-layer sheets. J. Macromol. Sci. B 2021, 60, 647–662.

[32] Neslihan, K.; Ilkay, O.Y.; Nuray, U.; Aysen, O.; Cafer, K. Sound absorption and thermal insulation properties of composite thermoplastic polyurethane/polystyrene (TPU/PS) nanofiber web and TPU nanofiber web and PS-extracted TPU/PS microfiber web. J. Ind. Text. 2022, 51, 7963S–7982S.

[33] Davoudabadi Farahani, M.; Jamshidi Avanaki, M.; Jeddi, A.A. Sound absorption of warp knitted spacer fabrics based on knit structure and nanofiber enhancement. J. Ind. Text. 2022, 51, 1539–1557.

[34] Yan, P.; Zhou, B.; Du, A. Synthesis of polyimide cross-linked silica aerogels with good acoustic performance. RSC Adv. 2014, 4, 58252–58259.

[35] Sachithanadam, M.; Joshi, S.C. Effect of granule sizes on acoustic properties of protein-based silica aerogel composites via novel inferential transmission loss method. Gels 2016, 2, 11.

[36] Merli, F.; Anderson, A.M.; Carroll, M.K.; Buratti, C. Acoustic measurements on monolithic aerogel samples and application of the selected solutions to standard window systems. J. Appl. Acoust. 2018, 142, 123–131.

[37] Oh, K.W.; Kim, D.K.; Kim, S.H. Ultra-porous flexible PET/Aerogel blanket for sound absorption and thermal insulation. Fibers Polym. 2009, 10, 731–737.

[38] Küçük, M.; Korkmaz, Y. The effect of physical parameters on sound absorption properties of natural fiber mixed nonwoven composites. Text. Res. J. 2012, 82, 2043–2053.

[39] Motahari, S.; Javadi, H.; Motahari, A. Silica-aerogel cotton composites as sound absorber. J. Mater. Civ. Eng. 2015, 27, 04014237.

[40] Ramamoorthy, M.; Pisal, A.; Rengasamy, R.; Rao, A.V. In-situ synthesis of silica aerogel in polyethylene terephthalate fibre nonwovens and their composite properties on acoustical absorption behavior. J. Porous Mater. 2018, 25, 179–187.

[41] Yang, T.; Xiong, X.; Venkataraman, M.; Mishra, R.; Nov, J.; Militký, J. Investigation on sound absorption properties of aero-gel/polymer nonwovens. J. Text. I 2019, 110, 196–201.

[42] Talebi, Z.; Soltani, P.; Habibi, N.; Latifi, F. Silica aerogel/polyester blankets for efficient sound absorption in buildings. Constr. Build. Mater. 2019, 220, 76–89.

[43] Mazrouei-Sebdani, Z.; Begum, H.; Schoenwald, S.; Horoshenkov, K.V.; Malfait, W.J. A review

on silica aerogel-based materials for acoustic applications. J. Non-Crystal Solids 2021, 562, 120770.

[44] F. De Pascalis, M. Nacucchi, M. Scatto, R. Albertoni. Quantitative characterisation of low-density, high performance polymeric foams using high resolution X-ray computed tomography and laser confocal microscopy. NDT E Int., 2016, 83, 123-133.

[45] S. C. Garcea, Y. Wang, P. J. Withers. X-ray computed tomography of polymer composites. Compos. Sci. Technol. 2018, 156, 305-319.

[46] T. Takahashi, M. Ueda, K.e Iizuka, A. Yoshimura, T. Yokozeki. Simulation on kink-band formation during axial compression of a unidirectional carbon fiber-reinforced plastic constructed by X-ray computed tomography images. Adv. Compos. Mater., Vol. 28, No. 4, 2019, 347-363.

[47] E.A. Zwanenburg, D.G. Norman, C. Qian, K.N. Kendall, M.A. Williams, J.M. Warnett. Effective X-ray micro computed tomography imaging of carbon fibre composites. Composites Part B, 2023, 258, 110707.

[48] L. E. Crica, J. Wengenroth, H. Tiainen, M. Ionita, H. J. Haugen. Enhanced X-ray absorption for micro-CT analysis of low density polymers. J. Biomater. Sci. Polym. Ed. 2016, 27, 805.

[49] Q. Yin, F. Y. Yap, L. Yin, L. Ma, Q. Zhou., L. W. Dobrucki, T. M. Fan, R. C. Gaba and J. Cheng. Poly(iohexol) nanoparticles as contrast agents for in vivo X-ray computed tomography imaging. J. Am. Chem. Soc. 2013, 135, 37, 13620–13623.

[50] T. R. Lex, B. R. Brummel, M. F. Attia, L. N. Giambalvo, K. G. Lee, B. A. V. Horn, D. C. Whitehead, F. Alexis. Iodinated Polyesters with Enhanced X-ray Contrast Properties for Biomedical Imaging. Sci. Rep. 2020, 10, 1508.

[51] A. Martinez, M. Kuhn, H. Briesen, D. Hekmat. Enhancing the X-ray contrast of polymeric biochromatography particles for three-dimensional imaging. J. Chromatogr. A 2019, 1590, 65.

[52] P. Diós, K. Szigeti, F. Budán, M. Pócsik, D. S. Veres, D. Máthé, S. Pál, A. Dévay, S. Nagy. Influence of barium sulfate X-ray imaging contrast material on properties of floating drug delivery tablets. Eur. J. Pharm. Sci., 2016, 95, 46.

[53] E. J. Rivera, L. A. Tran, M. H. Rivera, D. Yoon, A. G. Mikos, I. A. Rusakova, B. Y. Cheong, M. G. C. Hansen, J. T. Willerson, E. C. Perine and L. J. Wilson. Bismuth@US-tubes as a potential contrast agent for X-ray imaging applications. J. Mater. Chem. B, 2013, 1, 4792–480.

[54] M. H. Rivera, Ish Kumar, Stephen Y. Cho, B. Y. Cheong, M. X. Pulikkathara, S. E. Moghaddam, K. H. Whitmire, and L. J. Wilson. High-Performance Hybrid Bismuth–Carbon Nanotube Based Contrast Agent for X-ray CT Imaging. ACS Appl. Mater. Interfaces, 2017, 9, 7, 5709–5716.

[55] R. L Clough. High-energy radiation and polymers: A review of commercial processes and emerging applications. Nucl. Instr. and Meth. Phys. Res. B, 2001, 185, 8.

[56] X. Ping, M. Wang, X. Ge. The study on grafting comonomer of n-butyl acrylate and styrene onto poly(ethylene terephthalate) film by gamma-ray induced graft copolymerization. Radiat. Phys. Chem. 2010, 79, 941.

[57] X. Ping, M. Wang, X. Ge. Surface modification of poly(ethylene terephthalate) (PET) film by gamma-ray induced grafting of poly(acrylic acid) and its application in antibacterial hybrid film. Radiat. Phys. Chem. 2011, 80, 567.

[58] L. Ma, M. Wang, X. Ge. Surface treatment of poly(ethylene terephthalate) by gamma-ray induced graft copolymerization of methyl acrylate and its toughening effect on poly(ethylene terephthalate)/elastomer blend. Radiat. Phys. Chem. 2013, 90, 92.

[59] M. Khayet, M. M. Nasef, J. I. Mengual. Radiation grafted poly(ethylene terephthalate)-graft-polystyrene pervaporation membranes for organic/organic separation. J. Membr. Sci. 2005, 263, 77.

[60] M. M. Nasef. Gamma radiation-induced graft copolymerization of styrene onto poly(ethyleneterephthalate) films. J. Appl. Polym. Sci. 2000, 77, 1003.

[61] L. Xie, Y. Xie, Q. Wu, M. Wang, Q. Wu, X. Zhou, X. Ge. Effect of Poly(acrylic acid)-Modified Poly(ethylene terephthalate) on Improving the Integrated Mechanical Properties of Poly(ethylene terephthalate)/Elastomer Blend. Ind. Eng. Chem. Res. 2015, 54, 4748.

[62] Kang, Y. J. and Bolton, J. S. Finite element modeling of isotropic elastic porous materials coupled with acoustical finite elements. Journal of Acoustical Society of America, Vol. 98 (1995), pp. 635 – 643.

[63] Easwaran, V., Lauriks,W. and Coyette, J. P. Displacement–based finite element method for guided wave propagationproblems: Application to poroelastic media. Journal of Acoustical Society of America, Vol. 100 (1996), pp. 2989 –3002.

[64] Atalla, N., Panneton, R. and Debergue, P. A mixed displacement-pressure formulation for poroelastic materials. Journal of Acoustical Society of America, Vol. 104 (1998), pp. 1444 – 1452.

[65] Biot, M. A. Theory of propagation of elastic waves in a fluid-saturated porous solid. I.Low-frequency range. Journal of Acoustical Society of America, Vol. 28 (1956), pp. 168 – 178.

[66] Biot, M. A. Theory of propagation of elastic waves in a fluid-saturated porous solid. II. Higher frequency range. Journal of Acoustical Society of America, Vol. 28 (1956), pp. 179 – 191.

[67] Johnson, D. L., Koplik, J. and Dashen, R. Theory of dynamic permeability and tortuosity in fluid-saturated porous media. Journal of Fluid Mechanics, Vol. 176 (1987), pp. 379 – 402.

[68] Champoux, Y. and Allard, J. F. Dynamic tortuosity and bulk modulus in air–saturated porous media. Journal of Applied Physics, Vol. 70 (1991), pp. 1975 – 1979.

[69] Allard, J. F. Propagation of Sound in Porous Media. (1993), Elsevier Applied Science.

[70] Auriault, J. L., Borne, L. and Chambon, R. Dynamics of porous saturated media, checking of the generalized law of darcy. Journal of Acoustical Society of America, Vol. 77 (1985), pp. 1641 – 1650.

[71] Terada, K., Ito, T. and Kikuchi, N. Characterization of the mechanical behaviours of solid-fluid mixture by the homogenization method. Computer Methods in Applied Mechanics and Engineering, Vol. 153 (1998), pp. 223 – 257.

[72] Burridge, R. and Keller, J. B. Poroelasticity equations derived from microstructure. Journal of

Acoustical Society of America, Vol. 70 (1981), pp. 1140 – 1146.

[73] T. Yamamoto, S. Maruyama, K. Izui, S. Nishiwaki and K. Terada. Equivalent Properties of Sound Absorbing Poroelastic Material Using the Homogenization Method. Transactions of the JSME (in Japanese), Vol. 77, No. 773, pp. 75 - 88, 2011.

[74] T. Yamamoto, S. Maruyama, K. Izui, S. Nishiwaki and K. Terada. A Model for Sound – Absorbing Pomelastic Material Using Multiscale Analysis. Transactions of the JSME (in Japanese), Vol. 76, No. 768, pp. 2039 - 2048, 2010.

[75] T. Yamamoto, D. Katsura and H. Kubota. Sizing optimization of microstructure of sound-absorbing poroelastic material by homogenization method. Transactions of the JSME (in Japanese), Vol. 86, No. 889, pp. 20 - 00073, 2020.

[76] T. Yamamoto, D. Katsura and H. Kubota. Dissipation energy in sound-absorbing poroelastic material. Transactions of the JSME (in Japanese), Vol. 86, No. 887, pp. 19 - 00415, 2020.

[77] Yamamoto, T.; Katsura, D.; Kubota, H. Optimization of microstructure of sound-absorbing poroelastic material by homogenization method. In JSAE Annual Congress (Spring) Proceedings, 2018; p. 20185332.

[78] Yamakawa, K.; Yamamoto, T.; Katsura, D. Acoustic modelling technique of internal structures of a sound-absorbing foamed resin by homogenization method. In JSAE Congress (Autumn) Proceedings, 2019; p. 20196290.

[79] Katsura, D.; Yamamoto, T.; Yamakawa, K.; Hatakeyama, N.; Miura, R.; Okajima, J.; Inaba, K.; Ishizawa, Y.; Ochiai, H.; Yukawa, H.; Murashige, K.; Katagihara, J.; Tomotsu, J.; Ishimoto, T.; Ohshita, J. Development of thermal management and noise/vibration control material model technology by model-based research (MBR) 1st report. JSAE Annual Congress (Spring) Proceedings, 2021; p. 20215301.

[80] Yamakawa, K.; Yamamoto, T.; Katsura, D.; Inoue, M.; Hatakeyama, N.; Miura, R.; Okajima, J.; Inaba, K.; Ishizawa, Y.; Yukawa, H.; Ito, H.; Ishimoto, T.; Ohshita, J. Development of thermal management and noise/vibration control material model technology by model-based research (MBR) (2nd report). JSAE Annual Congress (Spring) Proceedings, 2022; p. 20225223.

[81] D. Katsura; K. Yamakawa. Development of flow resistance control technology for sound absorbing material surface by model-based research (MBR); JSAE Annual Congress (Spring) proceedings, 2023; p. 20235296.

Chapter 2: Gamma-ray-induced modification of poly(ethylene terephthalate) and polypropylene solid materials with halogen-containing olefins for X-ray CT image contrast enhancement

1. Introduction

X-ray computed tomography (CT) is a powerful technique for visualizing internal 3D microstructures in materials. It is extensively used to generate high-resolution CT images of inorganic materials that absorb X-ray efficiently. X-ray CT has been also used for organic polymeric materials even though these materials poorly absorb X-ray [1]. For instance, Garcea et al. described that the challenge for 3D imaging techniques of polymer composites with high resolution and high contrast. [2]. Using X-ray CT, Takahashi and coworkers acquired cross-sectional images of unidirectional carbon fiber-reinforced plastics to determine fiber positions [3]. Zwanenburg et al. reported the X-ray CT imaging of carbon fiber composite materials under optimized conditions [4]. Because organic polymers are composed of light elements with weak X-ray absorption (carbon, hydrogen, and oxygen), their CT images often have low contrast. Consequently, numerous approaches have been developed to enhance the contrast of X-ray CT images for organic polymers [5]. The incorporation of established X-ray contrast agents such as $BaCl_2$ and $AgNO_3$ into polymers is a well-known strategy for boosting X-ray CT image contrast. Hexamethyldisilazane is also employed as a convenient contrast reagent that readily reacts with OH groups to form $O-SiMe_3$ bonds. This substitution introduces relatively heavy silicon atoms, enhancing CT image contrast. However, these contrast agents are applicable only to polymers with suitable coordination or reaction sites, such as chitin, gelatin/poly(vinyl alcohol) composites, and polyacrylamide, but not to polymers such as poly(ethylene terephthalate) (PET) and polypropylene (PP), which lack the necessary interaction sites. It was also reported that nanoparticles prepared by cross-linking iodine-containing iohexol with hexamethylene diisocyanate coprecipitated

with mPEG-polylactide to enhance the CT contrast [6]. Lex et al. demonstrated the synthesis of iodine-containing polyesters exhibiting high X-ray CT image contrast via ring-opening polymerization of iodine-containing cyclic monomers and verified their potential as bioimaging contrast agents [7]. However, for widely used polymers lacking suitable interaction sites, effective methods for enhancing their CT images remain elusive. Physically adsorbed contrast agents such as iodine-containing sodium diatrizoate hydrate and KI in aqueous media offer limited applicability as they are effective primarily for porous materials [8]. Mixing organic polymer materials with heavy element salts like $BaSO_4$ or Bi(III) in the molding process has been explored [9-11]. Nonetheless, the tendency of these inorganic salts to aggregate within nonpolar organic polymers hinders homogeneous X-ray CT image contrast enhancement.

Gamma-ray irradiation is a well-established method for inducing radical graft polymerization in organic polymers [12–17]. This approach has been successfully applied, for instance, in the grafting of polystyrene onto PET via gamma irradiation in dichloromethane. The process, initiated by gamma-ray-induced radical formation on the ethylene carbon of PET, enables grafting even for solid PET materials (**Scheme 2-1**) [13, 16, 17]. Grafting acrylate on PET films or resin granules by gamma-ray irradiation has also been reported [15, 18]. To provide a simple and effective method to improve the X-ray CT images of organic polymeric materials, we report here the introduction of heavy elements, bromine and chlorine into PET fibers and PP pellets by similar reactions under gamma-ray irradiation in dichloromethane containing 2-bromoethyl methacrylate (1), 2-chloroethyl methacrylate (2), or 4-bromostyrene (3). This is a new method for enhancing X-ray CT image contrast in polymers that lack suitable interaction sites, paving the way for improved characterization of these materials.

22
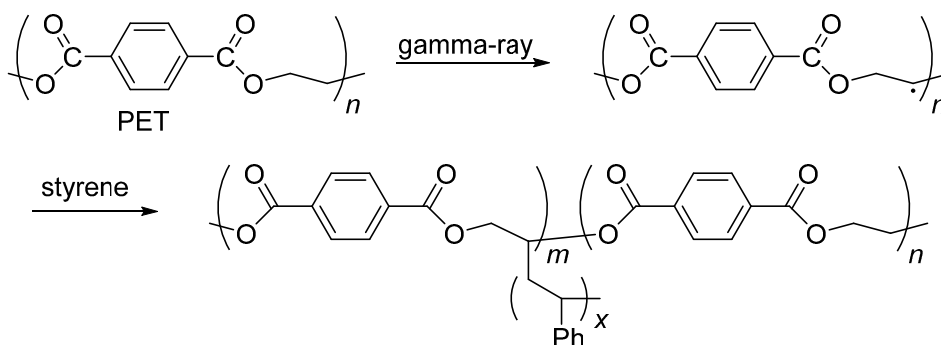
Scheme 2-1. Radical graft polymerization of styrene onto PET by gamma-ray irradiation.

2. Experimental

2.1 General

PET fibers (20 μm diameter, YPS 6.6Dtex) and PP pellets (4–4.5 mm) were purchased from Yamaichi Corp. and Japan Polypropylene Corp., respectively. Both materials were subjected to a cleaning process to remove process oils. This involved either hot water extraction in a Soxhlet apparatus for 3 h or ultrasonic irradiation in ethanol at room temperature for 30 min, followed by air-drying at 60 ℃ for 24 h. Dichloromethane (FUJIFILM Wako Pure Chemical Co., Ltd.) was used as the reaction solvent. Reagents, 1, 2, and 3 were purchased from Tokyo Chemical Industry Co., Ltd. and freshly distilled immediately before use. Gamma-ray irradiation was performed using a cobalt-60 (^{60}Co) source at the Radiation Research Facility, Hiroshima University. Solid-state ^{13}C NMR analysis was carried out using a Varian 600PS spectrometer equipped with a magic angle spinning (MAS) probe. The samples were placed in a zirconia-cylindrical rotor (3.2 mm ϕ) and spun at 15 kHz. Peak positions were referenced to the external standard hexamethylbenzene methyl peak (17.17 ppm). ^{13}C cross-polarization- magic angle spinning (CP-MAS) NMR measurements were conducted using ^{13}C–^{1}H dipolar coupling. The experiment utilized a proton 90° pulse duration of 2.55 μs, and a carbon 90° pulse duration of 3.0 μ s, an acquisition time of 0.02 s, a recycle delay of 3 s, a contact time of 10 ms, and 6000 scans accumulated at 25 °C. ^{13}C direct polarization-MAS (DP-MAS) NMR measurements

were conducted using an acquisition time of 0.02 s, a recycle delay of 30 s, and 1500 scans accumulated at 25 °C. X-ray CT analysis of the polymer samples was performed using a Rigaku nano3DX apparatus equipped with a high-resolution L1080 lens (2.53μ/voxel). The samples were placed within a 1.0 mm polyimide tube during the CT analysis that utilized a Cr target with an accelerating voltage of 35 kV and an emission current of 20 mA. Binning 1 was applied to the present measurements as binning 1 produced the highest resolution instead of the brightest image compared to the other binning modes. Image J software (National Institutes of Health, Bethesda, Maryland, USA) was used to quantify the CT image brightness. For further characterization of the modified polymers, focused ion beam scanning electron microscopy (FIB-SEM) and time-of-flight secondary ion mass spectrometry (TOF-SIMS) analysis of the modified polymer materials were carried out on Xe Plasma FIB-SEM and Tofwerk AG with 30 kV accelerating voltage and 0.10 nA emission current, respectively.

2.2 Modification of PET fibers and PP pellets via gamma-ray irradiation

PET fibers (7 denier, 50 mg) and a 2.0 mL dichloromethane solution of reagent 1 (5.7 M) (Table 1, run 1) were placed in a brown ampule for gamma-ray irradiation. After bubbling the solution with dry argon for 10 min to remove oxygen, the ampule was sealed and irradiated at ambient temperature for 4.3 h with a dose of approximately 10 kGy (dose-rate: 2.31 kGy/h), where the dose corresponds to the absorbed dose of alanine. Following irradiation, the PET fibers were thoroughly washed with THF under ultrasonic irradiation at 30 ºC to remove unreacted olefin 1 and its homopolymers.

3. Results and discussion

3.1 Modification and characterization of PET fibers

PET fibers were immersed in dichloromethane solutions containing varying concentrations of

reagent 1 as described in Materials and Methods (**Table 2-1**, runs 1 and 2). After gamma-ray irradiation (4.3 h, 10 kGy), the modified fibers were thoroughly washed with THF to remove unreacted reagent 1 and its homopolymer. The chemical structures of the modified PET fibers were analyzed using CP-MAS and DP-MAS ^{13}C NMR spectroscopy. The spectra before and after the reaction (run 2) are presented in **Figures 2-1**, respectively. Consistent with a previous report [19], the ^{13}C NMR spectrum of pristine PET displayed distinct peaks for carbonyl, phenyl, and ethylene carbons. Furthermore, a shoulder peak at 63 ppm was also observed, which could be assigned to terminal $HOCH_2CH_2$- groups at the polymer ends (**Figure 2-1a**). The signals of the modified PET are assigned as shown in **Figure 2-1b**. The introduction of an alkyl group into the PET ethylene shifted the corresponding ^{13}C NMR signal to a lower field. The peak at 65 ppm in the modified PET spectrum (**Figure 2-1b**) is likely due to the modified ethylene carbons (f, g, and h) [20]. Additionally, the signal for Br-substituted carbon (i) appeared around 26 ppm, consistent with the literature report [21]. Moreover, the sharp peak at 45 ppm can be assigned to highly crystalline sp3 carbons, potentially arising from ethylene units in the grafted chain [20, 22].
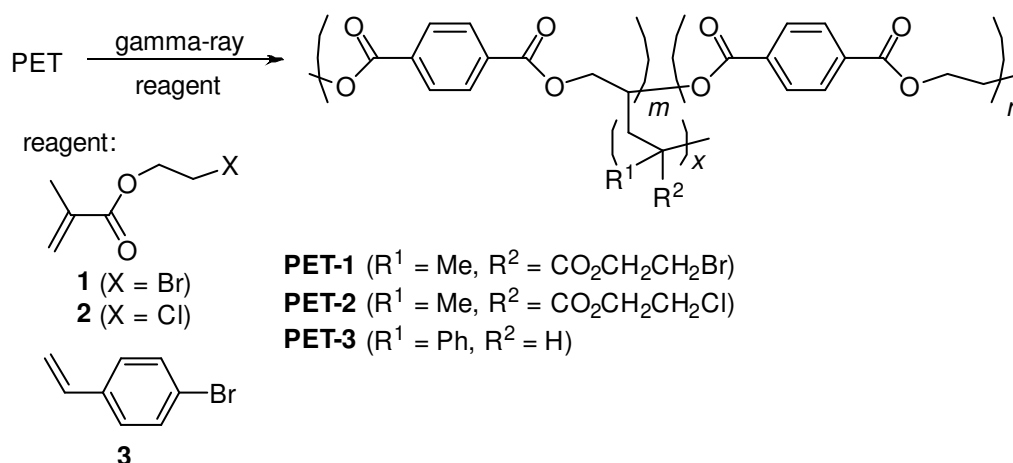
Scheme 2-2. Gamma-ray-induced graft polymerization of reagents 1–3 onto PET.

Table 2-1. Gamma-ray-induced graft polymerization of reagents onto PET fibers.

Run	Polymer	Dose/kGy	Monomer (amt/mol%[a])	Graft ratio[b]
1	**PET-1**	10	**1** (5.7)	0.06
2		10	**1** (20)	1.80
3	**PET-2**	10	**2** (5.7)	0.18
4	**PET-3**	10	**3** (5.7)	trace
5		10	**3** (21.4)	0.13
6	**PP-3**	10	**3** (5.7)	trace

[a] Monomer concentration in the reaction solvent.

[b] Incorporation ratio of grafted units ([reagent-based unit]/[PET repeating unit]) determined by DP-MAS ^{13}C NMR spectroscopy.

The incorporation ratios of reagent 1 into the PET backbone were quantified using the peak area ratios in the DP-MAS ^{13}C NMR spectrum (**Figure 2-2 and 2-3**). As summarized in **Table 2-1**, increasing the concentration of reagent 1 from 5.7 mol% (run 1) to 20 mol% (run 2) resulted in an approximately 30-fold increase in the incorporation ratio. Interestingly, this change coincided with a weakening of the PET ethylene signal at 62 ppm and the appearance of a new peak at around 65 ppm in the DP-MAS ^{13}C NMR spectrum. The similar peak area ratios of the signals at 62 ppm and 65 ppm to the incorporation ratios of reagent-derived units for both runs 1 and 2 suggest short grafting lengths (x) of the reagent. Whereas a broad, unidentified signal around 55 ppm was present in the DP-MAS ^{13}C NMR spectrum, its low intensity (peak area ratio) suggests minimal contribution. Similar trends were observed for reagents 2 and 3 (**Figures 2-4**, **2-5**, **2-6** and **2-7**, runs 3 and 4). While only trace amounts of the 3-derived unit were incorporated into the PET-3 fibers at 5.7 mol% (run 4), increasing reagent concentration to 21.4 mol% (run 5) led to a significant rise in the incorporation ratio to 0.13.
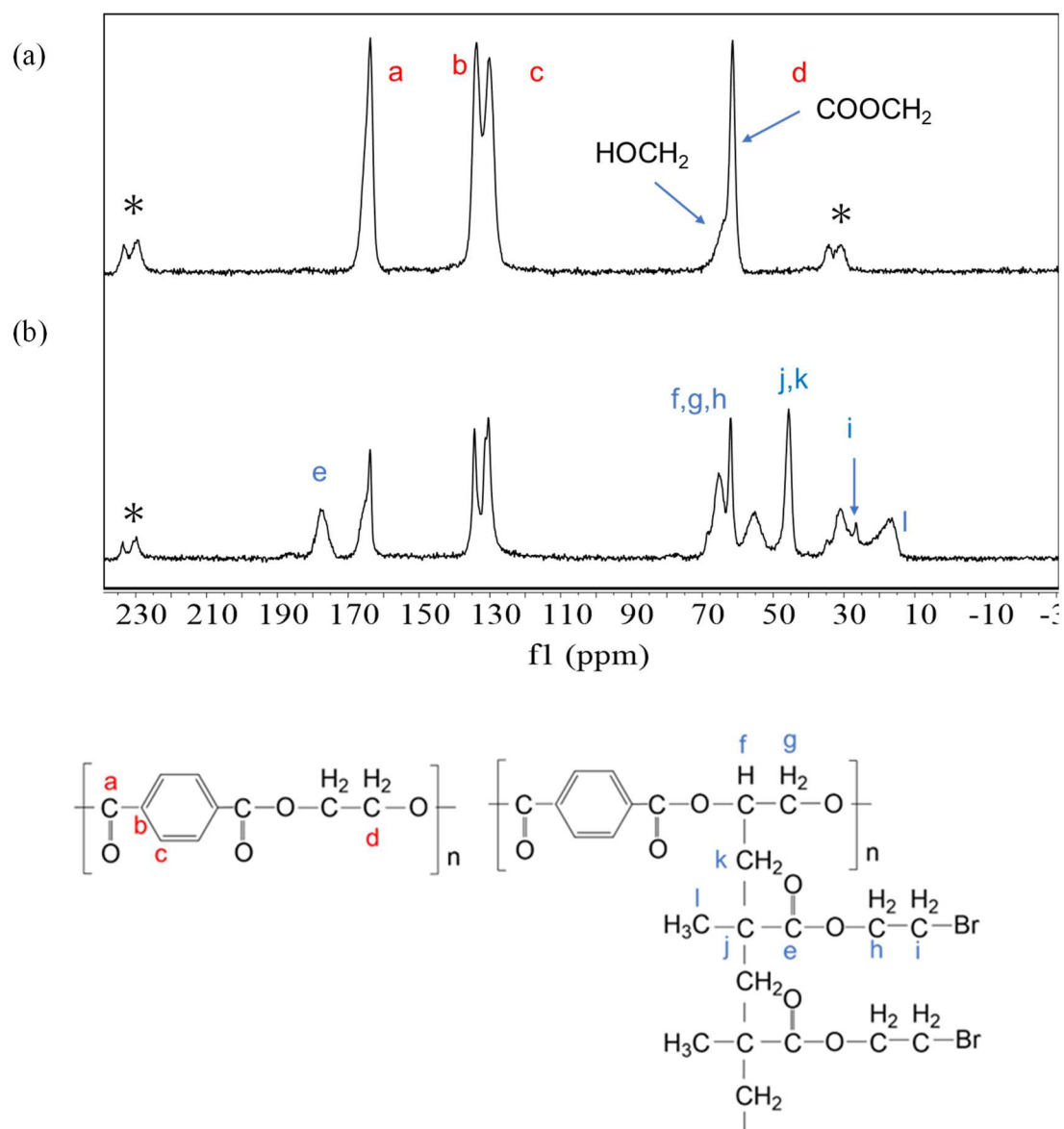
Figure 2-1. Solid-state CP-MAS ^{13}C NMR spectra of (a) pristine PET fibers and (b) PET-1 fibers (run 2) with peak assignments. Asterisks indicate spinning sidebands.
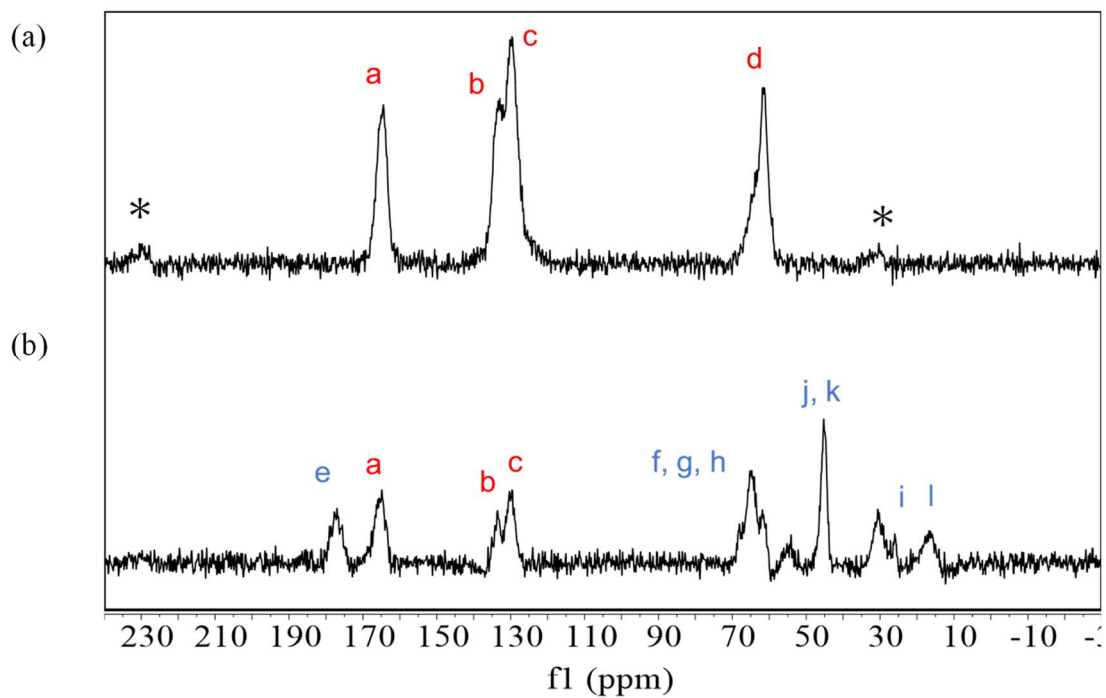
Figure 2-2. Solid-state DP-MAS ^{13}C NMR spectra of (a) pristine PET fibers and (b) PET-1 fibers (run 2) with peak assignments. Asterisks indicate spinning sidebands.
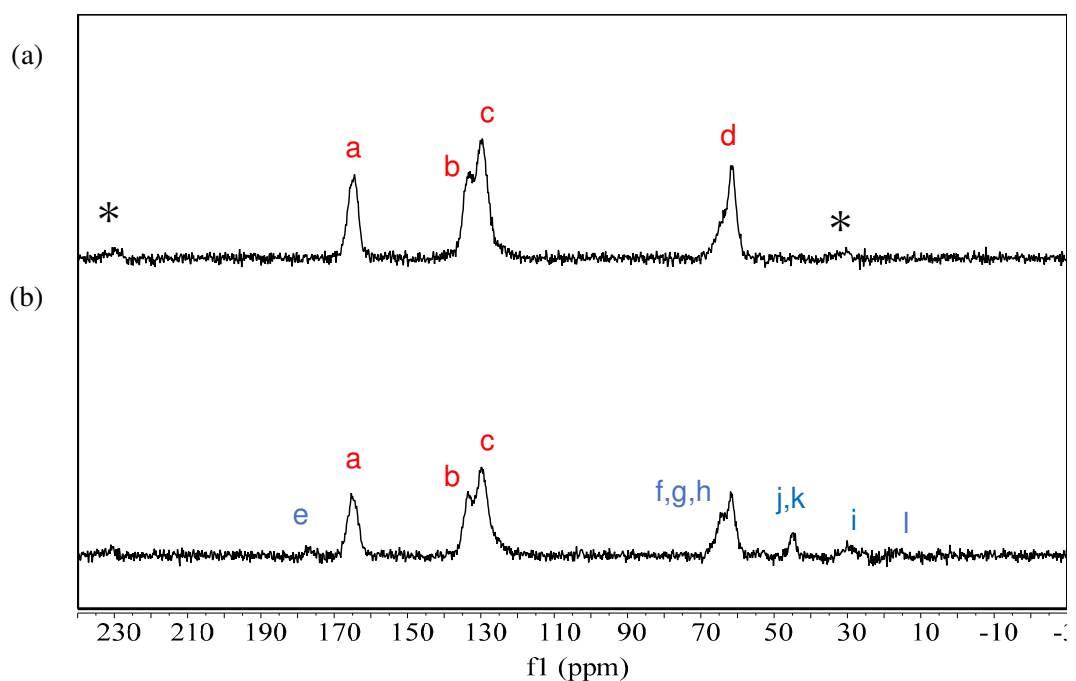
Figure 2-3. Solid-state DP-MAS ^{13}C NMR spectra of (a) pristine PET fibers and (b) PET-1 fibers (run 1) with peak assignments. Asterisks indicate spinning side bands.
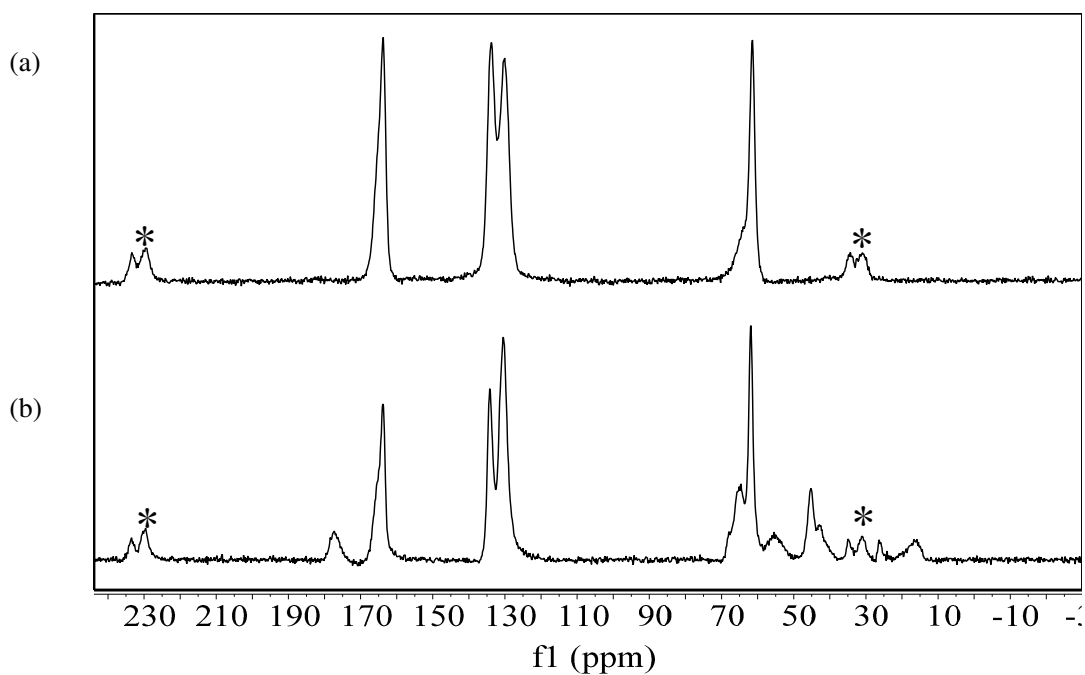
Figure 2-4. Solid-state CP-MAS ^{13}C NMR spectra of (a) pristine PET fibers and (b) PET-2 fibers (run 3) with peak assignments. Asterisks indicate spinning side bands.
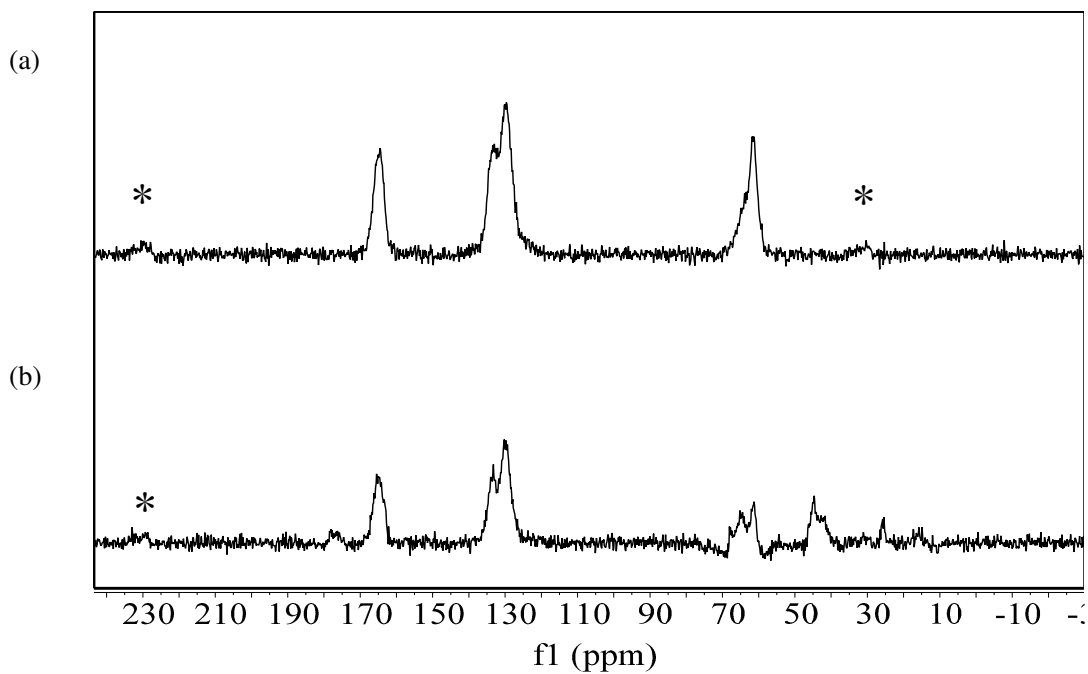
Figure 2-5. Solid-state DP-MAS ^{13}C NMR spectra of (a) pristine PET fibers and (b) PET-2 fibers (run 3) with peak assignments. Asterisks indicate spinning side bands.
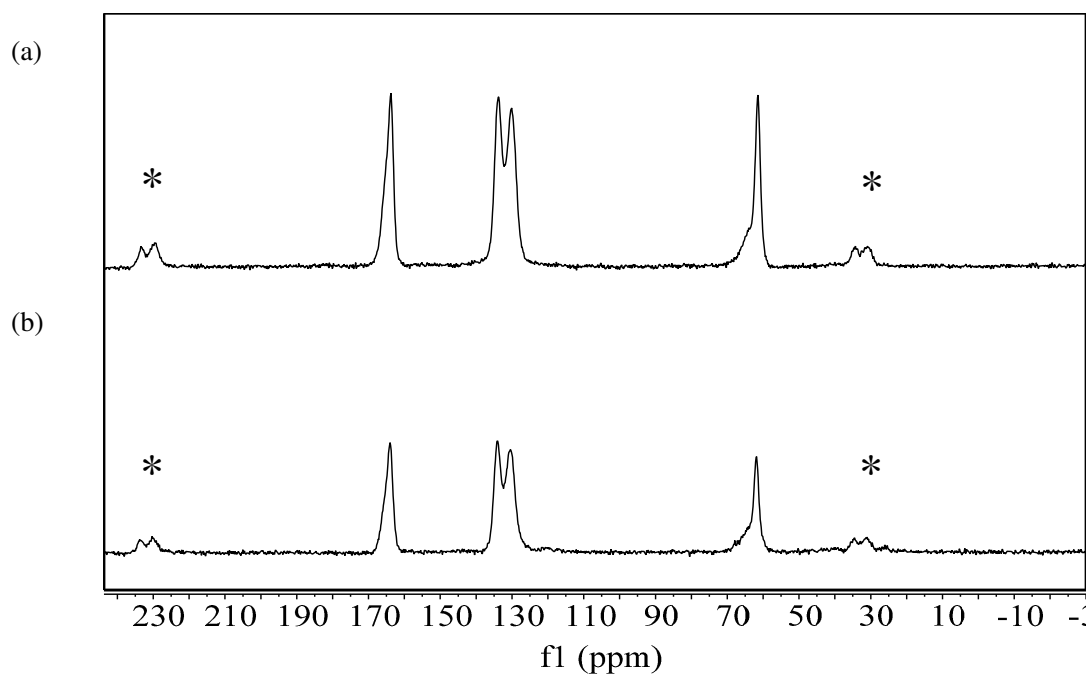
Figure 2-6. Solid-state CP-MAS ^{13}C NMR spectra of (a) pristine PET fibers and (b) PET-3 fibers (run 4) with peak assignments. Asterisks indicate spinning side bands.
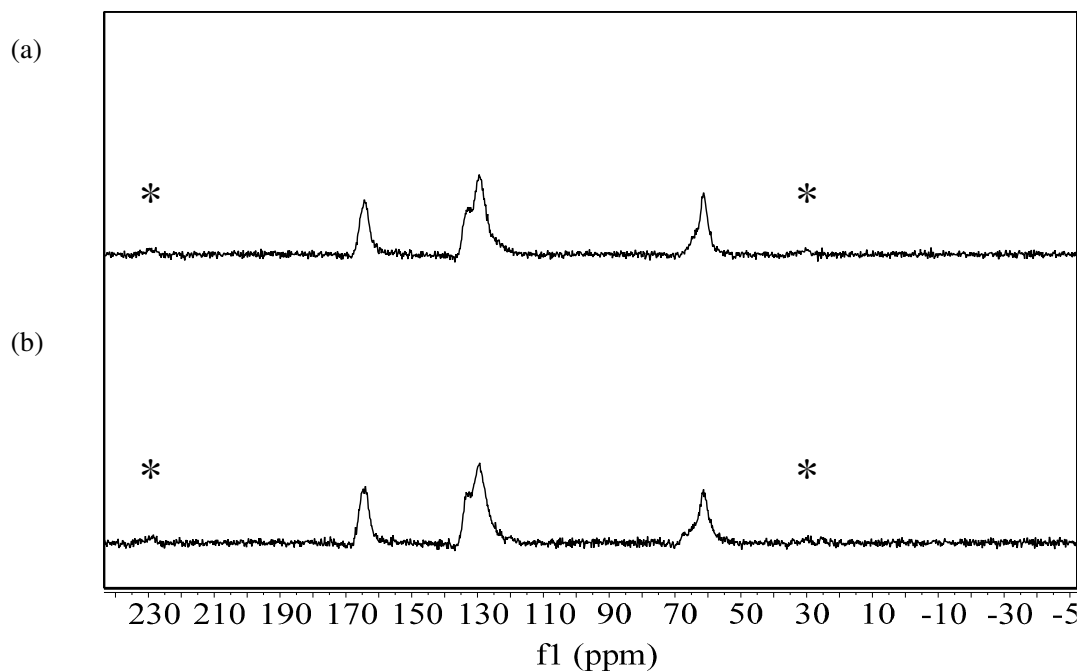
Figure 2-7. Solid-state DP-MAS ^{13}C NMR spectra of (a) pristine PET fibers and (b) PET-3 fibers (run 4) with peak assignments. Asterisks indicate spinning side bands.

To gain insight into the spatial distribution of halogen atoms, we performed FIB-SEM and TOF-SIMS analysis on a PET-1 fiber from run 1 (**Figure 2-8**). The results show a uniform distribution of bromine atoms across the fiber cross section, suggesting no significant accumulation near the surface.
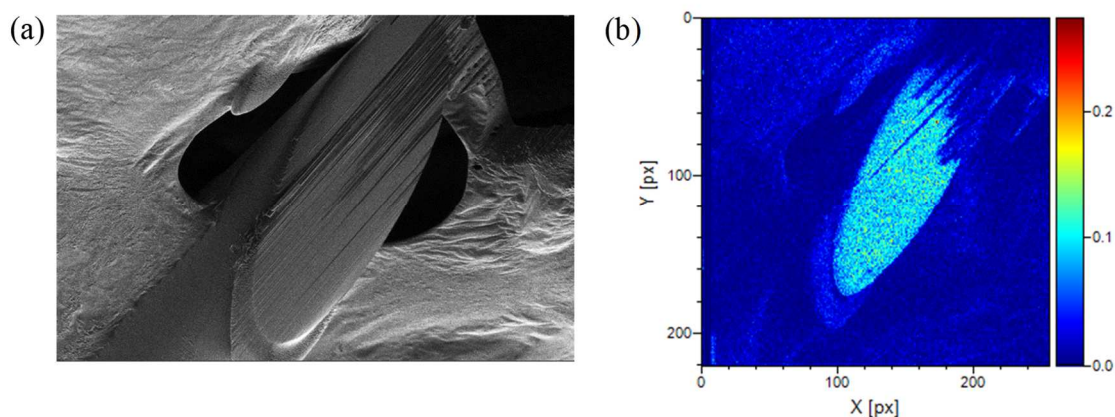
Figure 2-8. Analysis of PET-1 fibers (run 1) using FIB-SEM and TOF-SIMS. A cross-sectional SEM image of a PET-1 fiber prepared by FIB milling (a) and the TOF-SIMS distribution map of bromine across the fiber cross section (b).

3.2 X-ray CT analysis of modified PET fibers

Since the mass attenuation coefficient is larger for elements with larger atomic numbers, modification of the polymer samples with halogen-containing olefins were expected to exhibit improved X-ray CT images with enhanced contrasts. To evaluate potential changes in internal morphology, pristine and modified PET fibers were co-analyzed using X-ray CT (**Figure 2-9**). As shown in **Figures 2-9a** and **2-9b**, the incorporation of reagent 1 into PET-1 fibers led to a marked enhancement in image contrast compared with the pristine fibers. This finding is consistent with the homogeneous distribution of bromine observed by FIB-SEM and TOF-SIMS analysis (**Figure 2-8**), implying a uniform modification within the fiber. In contrast, PET-1 fibers from run 2, containing a

higher concentration of reagent 1 (**Table 2-1**), exhibited enhanced contrast primarily near the fiber surface compared with the fiber inside (**Figure 2-9b**). This observation suggests a preferential localization of bromine atoms at the surfaces. Additionally, these fibers displayed a roughly threefold increase in diameter compared with pristine PET fibers (**Figure 2-9b**), potentially indicating an overreaction of reagent 1 with PET. However, the diameter of PET-1 fibers from run 1 remained comparable to that of pristine PET fibers. This suggests that the 10 kGy irradiation dose and 5.7 mol% reagent concentration effectively enhanced the CT image contrast without changing the fiber shapes. In contrast to PET-1, PET-2 fibers modified with chlorine-containing reagent 2 exhibited no significant improvement in CT image contrast compared with pristine PET (**Figure 2-9c**). Despite a low incorporation ratio of reagent 3 (runs 4 and 5), PET-3 fibers displayed enhanced contrast in the CT images (**Figures 2-9d** and **2-9e**). Interestingly, this enhancement of the X-ray CT image contrast was observed for PET-1 fibers with a low incorporation of reagent 1 (run 1). To illustrate the utility of this approach, **Figure 2-10** presents both a longitudinal cross section and a 3D X-ray CT image of PET-1 (run 2).
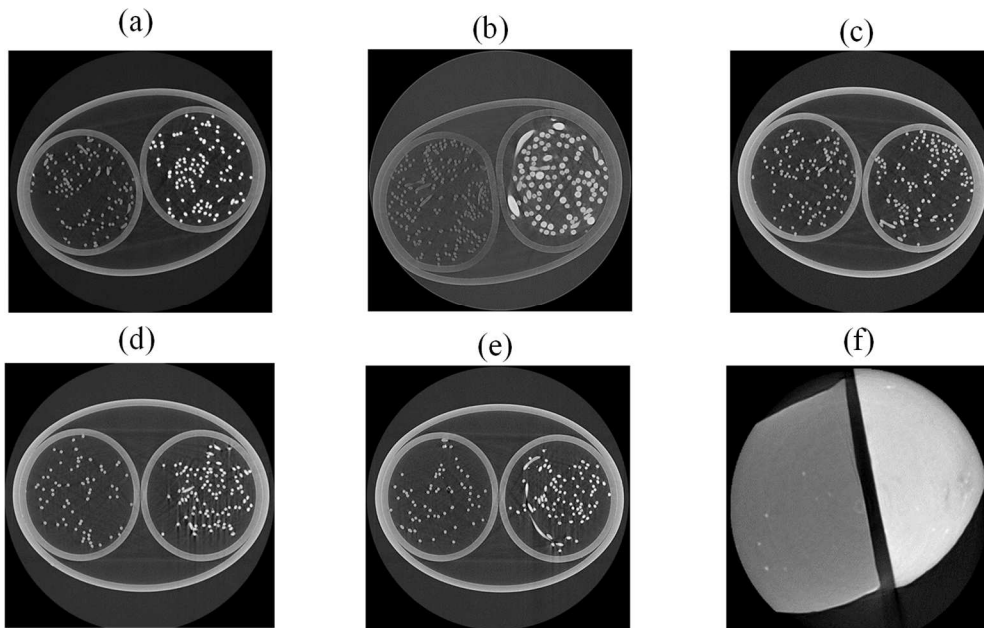
Figure 2-9. X-ray CT cross-sectional images (perpendicular to the longitudinal direction) of modified polymer samples in Kapton tubes: (a) PET-1 (run 1), (b) PET-1 (run 2), (c) PET-2 (run 3), (d) PET-3 (run 4), (e) PET-3 (run 5), and (f) PP-3 (run 6). Pristine PET fibers or a PP pellet are shown on the left side of each image for comparison.
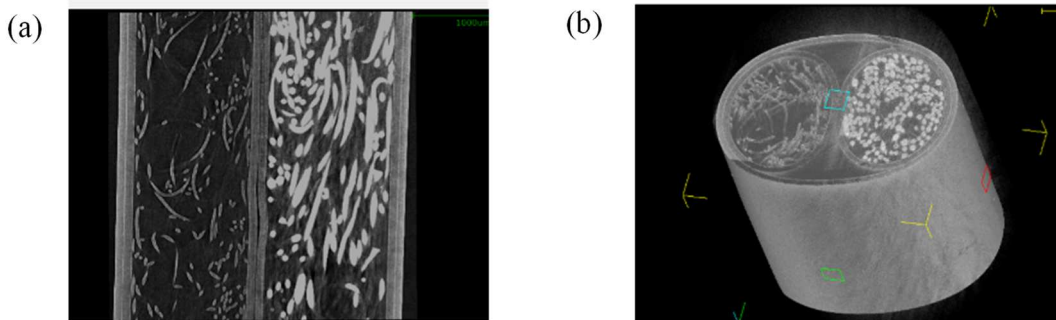
Figure 2-10. X-ray CT images of pristine PET and PET-1 (run 2) fibers in Kapton tubes: (a) longitudinal cross-sectional image and (b) 3D volume reconstruction.

Remarkably, PP pellets could also be modified under the same conditions established for PET. PP pellets (3.0 mm) were irradiated with gamma ray in dichloromethane containing reagent 3 and then washed with THF, resulting in PP-3 pellets with a significant improvement in CT image contrast, as evidenced by the homogeneous contrast enhancement observed in **Figure 2-9f**.

4. Conclusions

Our approach demonstrates the successful modification of PET and PP solids using bromine-containing olefin reagents via gamma-ray irradiation in dichloromethane. This process significantly enhances X-ray CT image contrast. The modification achieving penetration into took place not only on the surface of the material but also inside the solids, unless excessive irradiation doses are used. Consequently, homogeneous contrast enhancement is achieved, offering a valuable tool for analyzing polymer materials that lack binding sites for conventional contrast agents such as heavy metal salts. Furthermore, this approach offers minimal alteration to the size and shape of the modified solids, making it a valuable post-processing technique for achieving robust X-ray CT image contrast enhancement. This new simple method to effectively enhance the X-ray CT image contrast is potentially applicable to various polymer materials including polymer composites and porous polymer materials, readily allowing the observation of their 3D microstructures finely.

5. References

[1] F. De Pascalis, M. Nacucchi, M. Scatto, R. Albertoni. Quantitative characterisation of low-density, high performance polymeric foams using high resolution X-ray computed tomography and laser confocal microscopy. NDT E Int., 2016, 83, 123-133.

[2] S. C. Garcea, Y. Wang, P. J. Withers. X-ray computed tomography of polymer composites. Compos. Sci. Technol. 2018, 156, 305-319.

[3] T. Takahashi, M. Ueda, K.e Iizuka, A. Yoshimura, T. Yokozeki. Simulation on kink-band formation during axial compression of a unidirectional carbon fiber-reinforced plastic constructed by X-ray computed tomography images. Adv. Compos. Mater., Vol. 28, No. 4, 2019, 347-363.

[4] E.A. Zwanenburg, D.G. Norman, C. Qian, K.N. Kendall, M.A. Williams, J.M. Warnett. Effective X-ray micro computed tomography imaging of carbon fibre composites. Composites Part B, 2023, 258, 110707.

[5] L. E. Crica, J. Wengenroth, H. Tiainen, M. Ionita, H. J. Haugen. Enhanced X-ray absorption for micro-CT analysis of low density polymers. J. Biomater. Sci. Polym. Ed. 2016, 27, 805.

[6] Q. Yin, F. Y. Yap, L. Yin, L. Ma, Q. Zhou., L. W. Dobrucki, T. M. Fan, R. C. Gaba and J. Cheng. Poly(iohexol) nanoparticles as contrast agents for in vivo X-ray computed tomography imaging. J. Am. Chem. Soc. 2013, 135, 37, 13620–13623.

[7] T. R. Lex, B. R. Brummel, M. F. Attia, L. N. Giambalvo, K. G. Lee, B. A. V. Horn, D. C. Whitehead, F. Alexis. Iodinated Polyesters with Enhanced X-ray Contrast Properties for Biomedical Imaging. Sci. Rep. 2020, 10, 1508.

[8] A. Martinez, M. Kuhn, H. Briesen, D. Hekmat. Enhancing the X-ray contrast of polymeric biochromatography particles for three-dimensional imaging. J. Chromatogr. A 2019, 1590, 65.

[9] P. Diós, K. Szigeti, F. Budán, M. Pócsik, D. S. Veres, D. Máthé, S. Pál, A. Dévay, S. Nagy. Influence of barium sulfate X-ray imaging contrast material on properties of floating drug delivery tablets. Eur. J. Pharm. Sci., 2016, 95, 46.

[10] E. J. Rivera, L. A. Tran, M. H. Rivera, D. Yoon, A. G. Mikos, I. A. Rusakova, B. Y. Cheong, M. G. C. Hansen, J. T. Willerson, E. C. Perine and L. J. Wilson. Bismuth@US-tubes as a potential contrast agent for X-ray imaging applications. J. Mater. Chem. B, 2013, 1, 4792–480.

[11] M. H. Rivera, Ish Kumar, Stephen Y. Cho, B. Y. Cheong, M. X. Pulikkathara, S. E. Moghaddam, K. H. Whitmire, and L. J. Wilson. High-Performance Hybrid Bismuth–Carbon Nanotube Based Contrast Agent for X-ray CT Imaging. ACS Appl. Mater. Interfaces, 2017, 9, 7, 5709–5716.

[12] R. L Clough. High-energy radiation and polymers: A review of commercial processes and emerging applications. Nucl. Instr. and Meth. Phys. Res. B, 2001, 185, 8.

[13] X. Ping, M. Wang, X. Ge. The study on grafting comonomer of n-butyl acrylate and styrene onto poly(ethylene terephthalate) film by gamma-ray induced graft copolymerization. Radiat. Phys. Chem. 2010, 79, 941.

[14] X. Ping, M. Wang, X. Ge. Surface modification of poly(ethylene terephthalate) (PET) film by gamma-

ray induced grafting of poly(acrylic acid) and its application in antibacterial hybrid film. Radiat. Phys. Chem. 2011, 80, 567.

[15] L. Ma, M. Wang, X. Ge. Surface treatment of poly(ethylene terephthalate) by gamma-ray induced graft copolymerization of methyl acrylate and its toughening effect on poly(ethylene terephthalate)/elastomer blend. Radiat. Phys. Chem. 2013, 90, 92.

[16] M. Khayet, M. M. Nasef, J. I. Mengual. Radiation grafted poly(ethylene terephthalate)-graft-polystyrene pervaporation membranes for organic/organic separation. J. Membr. Sci. 2005, 263, 77.

[17] M. M. Nasef. Gamma radiation-induced graft copolymerization of styrene onto poly(ethyleneterephthalate) films. J. Appl. Polym. Sci. 2000, 77, 1003.

[18] L. Xie, Y. Xie, Q. Wu, M. Wang, Q. Wu, X. Zhou, X. Ge. Effect of Poly(acrylic acid)-Modified Poly(ethylene terephthalate) on Improving the Integrated Mechanical Properties of Poly(ethylene terephthalate)/Elastomer Blend. Ind. Eng. Chem. Res. 2015, 54, 4748.

[19] A. Jinno, Y. Ogasawara, T. Hashimoto, M. Mitsumoto, T. M. Chang, M. Sone, H. Kurosu. Solid-state ^{13}C NMR spectroscopic study of supercritical CO_2 catalyzation treated polyethylene terephthalate textiles for platinum metallization. J. supercrit. fluids, 197, 2023, 105896.

[20] J. Sohma, C. Qun, W. Yuanshen, Q. Xue-Wen, M. Shiotani. Solid-state high-resolution ^{13}C-NMR study of crosslinks in heavily gamma-irradiated polyethylene. Radial. Phys. Chem., Vol. 37. No. 1, 1991, 47-51.

[21] G. Y. N. Chan, M. G. Looney, D. H. Solomon, S. Veluayitham. The Synthesis of Novel Hybrid Monomers. Aust. J. Chem., 1998, 51, 31-35.

[22] Z. G. Gök, M. Inal, O. Bozkaya, M. Yigitoglu, I. Vargel. Production of 2-hydroxyethyl methacrylate-g -poly(ethylene terephthalate) nanofibers by electrospinning and evaluation of the properties of the obtained nanofibers. J. Appl. Polym. Sci. 2020, 137, 41.

Chapter 3: Sound-Absorbing, Thermal-Insulating Material Based on Poly(methylsiloxane) Xerogel and Cellulose Nanofibers

1. Introduction

A typical property that indicates the performance of a porous sound-absorbing material is its sound absorption coefficient. A high-performance porous sound absorber generally has a mixed structure of a solid phase as its base material and a fluid phase consisting of braided channels with diameters ranging from several tens of micrometers to several millimeters; its sound absorption properties depend on its microstructure [1–5].

Another typical property that arises from a porous structure is thermal conductivity. A high-performance porous thermal insulator generally has a mixed structure comprising a solid phase as its base material and a fluid phase consisting of independent spaces with diameters ranging from several tens of nanometers to several tens of micrometers; its thermal insulation properties also depend on its microstructure [6–8]. Thus, porous sound absorbers and porous thermal insulators are similar; they differ in the microstructures they offer for high performance, specifically the size and connectivity of their fluid phases. The difference in the size scale of the fluid phase makes it difficult to achieve compatibility between the two materials at high dimensions.

Materials with excellent dual performance have been studied with experiments. Specifically, nanofibers and nanofiber-based composites have been investigated in the literature in the past decade. Materials such as polyacrylonitrile (PAN) [9], polyvinylidene fluoride [10], cellulose [11], polyurethane [12], and thermoplastic polyurethane (TPU)/polystyrene (PS) [13] were used either alone as nanofibers or as a part of compo-site for sound absorption properties. For example, Karaca et al. showed a thermal conductivity of 0.050 W/(m·K) and a sound absorption coefficient of 0.5–0.6 around 1000 Hz with TPU/PS-BSE nanofibers fabricated with electrospinning solutions. Zahra et al. also

summarized research trends in silica aerogel-based materials for acoustic applications [14]. For example, hot-pressed formed plates via the dry-mixing of silica aerogel with polyvinylbutyrale (PVB) showed a sound absorption coefficient of about 0.2 around 1000 Hz at a thickness of 10 mm. Polyethylene terephthalate (PET) nonwoven-silica aerogel blankets had a sound absorption coefficient of about 0.1 around 1000 Hz at a thickness of 5 mm. On the other hand, these studies point out the lack of mathematical modeling to understand key physical mechanisms that can explain the observed acoustical behavior of aerogels.

Therefore, we have developed a computational microstructure modeling approach that predicts three properties of porous materials: sound absorption, thermal insulation, and vibration damping (**Figure 3-1**) [15]. Vibration damping is an important property that affects the ride and feel of a vehicle, but it is not the subject of this study.

In this study, we developed a porous material with excellent sound absorption and thermal insulation using this computational microstructure modeling approach. The porous material was obtained in a sol–gel process from organoalkoxysilanes and cellulose nanofibers (CNFs), namely, a composite xerogel of poly(methylsiloxane) (PMS) and CNF.
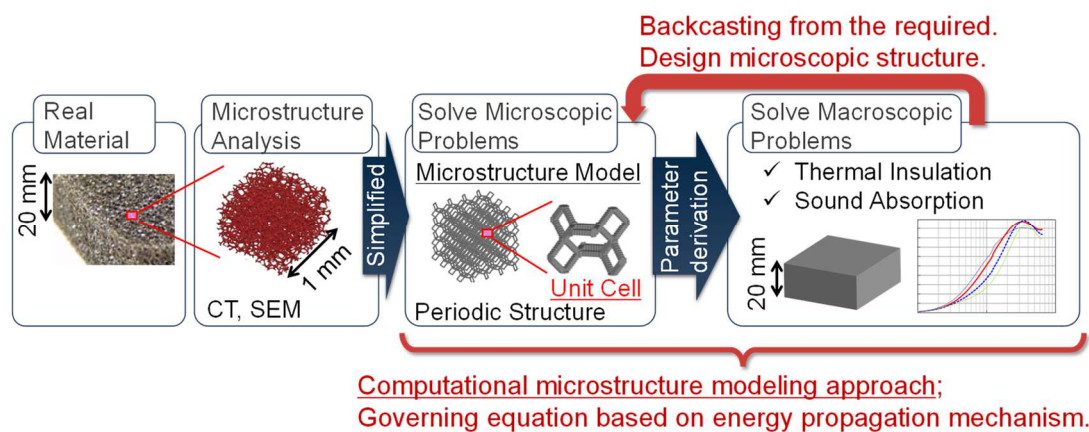
Figure 3-1. Development of high-performance multifunctional materials by materials model-based research.

2. Materials and Methods

2.1 Computational Microstructure Modeling Approach to Designing Porous Materials

The sound absorption and heat conduction phenomena occurring in the solid and fluid phases inside porous materials are formulated using the homogenization method. This section outlines the microstructural design model of such sound absorption phenomenon.

The sound absorption model considers the viscosity of the fluid phase and attenuation due to heat dissipation. Homogenization is applied using asymptotic expansion to directly obtain the equivalent properties necessary to predict the macroscopic proper-ties of the porous sound-absorbing material from its microstructure. These equivalent properties are then applied to a model of porous sound absorbers to determine the macroscopic properties of the material, such as its sound absorption coefficient, as de-scribed by Yamamoto et al. [16].

Consider the porous sound-absorbing material with a periodic microstructure shown in **Figure 3-2**. For the microscale governing equations, the equilibrium, constitutive, and displacement–strain relations of a linear elastic body are applied to the solid phase. The linearized Navier–Stokes equations are applied to the flow field of the fluid phase, which is assumed to exhibit microdisplacement. The temperature field of the flu-id phase follows the first law of thermodynamics. Because the specific heat of the solid phase is sufficiently high compared with that of the fluid phase, the temperature field of the solid phase is assumed to be in equilibrium. The law of conservation of mass and an equation of state are considered the governing equations. Velocity, vertical stress, and temperature continuity conditions are imposed at the boundary between the solid and fluid phases. Assuming an asymptotically expanded solution and substituting it in-to the microscale governing equations, we obtain microscale boundary value problems. Macroscopic properties, such as equivalent density, are obtained by volume-averaging the solutions obtained from solving these equations. The macroscale governing equations for the solid and fluid phases are derived by averaging the microscale governing

39

equations. Performance indicators, such as the sound absorption coefficient, are deter-mined by solving these equations.
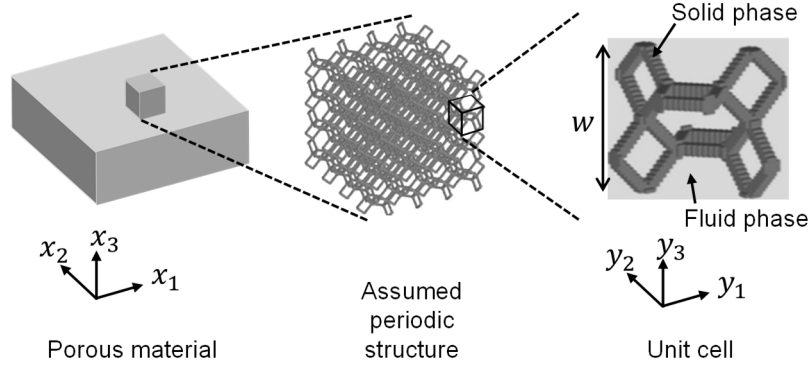
Figure 3-2. Schematic diagram of homogenization of sound-absorbing poroelastic material.

The microscale governing equations of a porous sound-absorbing material are described. The solid phase is an isotropic linear elastic body, the fluid phase is a viscous fluid with a compressible viscosity coefficient μ^f, and all fluid phases are assumed to be connected. The governing equations for the solid phase are expressed as Equation (1), where ω is angular frequency, u_i^s is the displacement of the solid phase, ρ^s is the mass density, c_{ijkl}^s is the elasticity tensor, ε_{kl}^s is the distortion, and σ_{ij}^s is the stress.

$$-\rho^s \omega^2 u_i^s = \frac{\partial \sigma_{ij}^s}{\partial x_j}, \ \sigma_{ij}^s = c_{ijkl}^s \varepsilon_{kl}^s, \ \varepsilon_{kl}^s = \frac{1}{2}\left(\frac{\partial u_k^s}{\partial x_l} + \frac{\partial u_l^s}{\partial x_k}\right) \tag{1}$$

The velocity and mass density of the fluid phase are denoted as v_i^f and δ^f, respectively. The governing equations for the flow field of the fluid phase are expressed in terms of the linearized Navier–Stokes equations, given that they are of a small amplitude:

$$\rho^f j\omega v_i^f = \frac{\partial \sigma_{ij}^f}{\partial x_j}, \ \sigma_{ij}^f = -p^f \delta_{ij} + 2\mu^f \dot{\varepsilon}_{ij}^f - \frac{2}{3}\mu^f \delta_{ij} \dot{\varepsilon}_{kk}^f, \ \dot{\varepsilon}_{ij}^f = \frac{1}{2}\left(\frac{\partial v_i^f}{\partial x_j} + \frac{\partial v_j^f}{\partial x_i}\right) \tag{2}$$

The specific heat of the solid phase is sufficiently high compared with that of the fluid phase, so

the temperature T_0 can be assumed to be in equilibrium. Then, only the fluid phase needs to be considered for the temperature field, and the governing equation can be expressed as follows according to the first law of thermodynamics:

$$-\frac{\partial q_i^f}{\partial x_i} = j\omega \rho^f C_v^f \tau^f + (j\omega \rho^f R\tau^f - j\omega p^f), \ q_i^f = -\kappa_{ij}^f \frac{\partial \tau^f}{\partial x_j}, \tag{3}$$

where τ^f is the temperature variation, C_v^f is the constant-volume specific heat, R is the gas constant, q_i^f is the heat flow velocity, and κ_{ij}^f is the thermal conductivity. The law of conservation of mass and equation of state for the fluid phase can be expressed as follows:

$$\rho^f \frac{\partial v_i^f}{\partial x_i} + j\omega \delta^f = 0, \ \frac{p^f}{p^f} = \frac{\delta^f}{\rho^f} + \frac{\tau^f}{T^f}. \tag{4}$$

The boundary conditions at the boundary Γ^{sf} between the solid and fluid phases are written in terms of the continuity of velocity, boundary vertical stress, and temperature as follows:

$$j\omega u_i^s = v_i^f, \ \sigma_{ij}^s n_j^s + \sigma_{ij}^f n_j^f = 0, \ \tau^f = 0, \tag{5}$$

where n_i^s and n_i^f are the unit normal vectors of the solid and fluid phases, respectively, outward to the domain at Γ^{sf}.

Assuming that the microstructure is periodic, let Y be the unit cell and l be the size of the unit cell ($l = w$ in **Figure 3-2**). The representative macroscale length L is the wavelength of the porous material, and the ratio of the representative microscale length to the representative macroscale length is $\varepsilon = l / L$. Let $\boldsymbol{x}$ be the macroscale spatial variable and $\boldsymbol{y} = \boldsymbol{x}/\varepsilon$ ($\varepsilon \ll 1$) be the microscale spatial variable. Asymptotic expansion solutions are possible; Gilbert and Mikelić [17] and Clopeau et al. [18] applied two-scale convergence theory to a problem of porous materials. For the state quantities u_i^s, v_i^f, p^f, τ^f, and δ^f, the author assumes the asymptotic expansion solution of Sanchez-Palencia [19] as follows:

$$u_i^s = u_i^{s(0)}(\boldsymbol{x}, \boldsymbol{y}) + \varepsilon u_i^{s(1)}(\boldsymbol{x}, \boldsymbol{y}) + \varepsilon^2 u_i^{s(2)}(\boldsymbol{x}, \boldsymbol{y}) + \cdots, \tag{6}$$

$$v_i^f = v_i^{f(0)}(\boldsymbol{x}, \boldsymbol{y}) + \varepsilon v_i^{f(1)}(\boldsymbol{x}, \boldsymbol{y}) + \varepsilon^2 v_i^{f(2)}(\boldsymbol{x}, \boldsymbol{y}) + \cdots, \tag{7}$$

41

$$p^f = p^{f(0)}(\mathbf{x}, \mathbf{y}) + \varepsilon p^{f(1)}(\mathbf{x}, \mathbf{y}) + \varepsilon^2 p^{f(2)}(\mathbf{x}, \mathbf{y}) + \cdots, \tag{8}$$

$$\tau^f u_i^s = \tau^{f(0)}(\mathbf{x}, \mathbf{y}) + \varepsilon \tau^{f(1)}(\mathbf{x}, \mathbf{y}) + \varepsilon^2 \tau^{f(2)}(\mathbf{x}, \mathbf{y}) + \cdots, \tag{9}$$

$$\delta^f u_i^s = \delta^{f(0)}(\mathbf{x}, \mathbf{y}) + \varepsilon \delta^{f(1)}(\mathbf{x}, \mathbf{y}) + \varepsilon^2 \delta^{f(2)}(\mathbf{x}, \mathbf{y}) + \cdots, \tag{10}$$

where all terms on the right-hand side are periodic with respect to $\mathbf{y}$ (Y-periodic).

Applying the Galerkin method to a relational expression of the order of ε^{-1} for the solid phase, the author obtains the following boundary value problem for the Y-periodic characteristic function $\chi_i^{kl}(\mathbf{y})$:

$$\int_Y \left(c_{ijkl}^s - c_{ijpq}^s \frac{\partial \chi_p^{kl}(\mathbf{y})}{\partial y_q} \right) \frac{\partial \delta u_i^s}{\partial y_j} dY = 0. \tag{11}$$

The characteristic function $\chi_i^{kl}(\mathbf{y})$ can be obtained by solving the above equation under the condition $\int_Y \chi_i^{kl}(\mathbf{y}) = 0$ to exclude rigid-body displacements.

Consider the relative velocity $w_i^{f(0)} = v_i^{f(0)} - j\omega u_i^{s(0)}$ of the fluid phase to the solid phase on the order of ε^0 and replace $v_i^{f(0)}$ with $w^{f(0)} + j\omega u_i^{s(0)}$. From the relation on the order of ε^{-1}, the author obtains the following microscale boundary value problem for the flow field of the fluid phase:

$$\int_Y \rho^f j\omega \xi_i^k(\mathbf{y}) \delta w_i^f dY + \int_Y \mu^f \frac{\partial \xi_i^k(\mathbf{y})}{\partial y_j} \frac{\partial \delta w_i^f}{\partial y_j} dY + \int_Y \frac{1}{3} \mu^f \frac{\partial \xi_i^k(\mathbf{y})}{\partial y_i} \frac{\partial \delta w_i^f}{\partial y_i} dY$$

$$- \int_Y \frac{\partial \xi_i^k(\mathbf{y})}{\partial y_i} \delta p^f dY - \int_Y \frac{\partial \delta w_i^f}{\partial y_i} \pi^k(\mathbf{y}) dY = \int_Y \delta \xi_k^k(\mathbf{y}) dY \tag{12}$$

where $\xi_i^k(\mathbf{y})$ and $\pi^k(\mathbf{y})$ are the Y-periodic characteristic functions of relative velocity and pressure, respectively. $\xi_i^k(\mathbf{y}) = 0$ at Γ^{sf}. $\xi_i^k(\mathbf{y})$ and $\pi^k(\mathbf{y})$ are obtained by implement the condition $\int_Y \pi^k(\mathbf{y}) dY = 0$ to exclude the constant-pressure component.

From the relation for the temperature $\tau^{f(0)}$ of the fluid phase on the order of ε^0, the author obtains the following boundary value problem:

$$\int_Y \frac{1}{j\omega \rho^f c_p^f} \kappa_{ij}^f \frac{\partial \zeta(\mathbf{y})}{\partial y_j} \frac{\partial \delta \tau^f}{\partial y_i} dY + \int_Y \zeta(\mathbf{y}) \delta \tau^f dY = \int_Y \delta \tau^f dY, \tag{13}$$

where $\zeta(\mathbf{y})$ is a Y-periodic characteristic function with respect to temperature; the isothermal condition $\zeta(\mathbf{y}) = 0$ is satisfied at Γ^{sf}.

The characteristic function $\chi_i^{kl}(\mathbf{y})$ in unit cell Y, obtained by solving the corresponding boundary value problem, is volume averaged. The homogenized elastic tensor $\langle c_{ijkl}^S \rangle$ of the solid phase is obtained using the following formula:

$$c_{ijkl}^H = \frac{1}{|Y|} \int_Y \left[c_{ijkl}^S - c_{ijpq}^S \frac{\partial \chi_p^{kl}(\mathbf{y})}{\partial y_q} \right] dY, \tag{14}$$

where $|Y|$ is the volume of the unit cell Y of the porous material.

The equivalent density ρ_{ki}^{fc} of the fluid phase is obtained by volume averaging the $\xi_i^k(\mathbf{y})$ of the fluid phase Y^f in the unit cell:

$$\rho_{ki}^{fc} = \frac{1}{j\omega} \langle \xi_i^k(\mathbf{y}) \rangle_{Y^f}^{-1}, \tag{15}$$

where $|Y^f|$ is the volume of the fluid phase Y^f in the unit cell and $\langle \ \ \rangle_{Y^f}$ is the volume average of Y^f.

The equivalent volumetric modulus of elasticity K^f of the fluid phase is obtained by volume averaging the $\zeta(\mathbf{y})$ of the fluid phase Y^f in the unit cell as follows:

$$K^f = \frac{\gamma^f P^f}{\gamma^f - (\gamma^f - 1)\langle \zeta(\mathbf{y}) \rangle_{Y^f}}. \tag{16}$$

The obtained macroscopic properties are then used to derive the macroscale governing equations for the solid and fluid phases, respectively, as follows [20]:

$$\frac{\partial \hat{\sigma}_{ij}^{s(0)}}{\partial x_j} + \bar{\rho}\omega^2 u_i^{s(0)} - \rho_0^f \omega^2 d_i^k u_k^{s(0)} - j\omega d_i^k \frac{\partial \psi^{f(0)}}{\partial x_k} + j\omega\phi \frac{\partial \psi^{f(0)}}{\partial x_i} + j\omega k_{ij}^H \frac{\partial \psi^{f(0)}}{\partial x_j} = \quad (17)$$
$$0,$$

$$\frac{d_i^k}{\rho_0^f} \frac{\partial^2 \psi^{f(0)}}{\partial x_k \partial x_i} + \omega^2 \left(\theta^f + \frac{\phi}{K^f} \right) \psi^{f(0)} - j\omega d_i^k \frac{\partial u_k^{s(0)}}{\partial x_i} + j\omega\phi \frac{\partial u_i^{s(0)}}{\partial x_i} + j\omega\theta^{s,pq}\varepsilon_{pq}^{s(0)} = 0, \quad (18)$$

where $\psi^{f(0)}$ is the potential function, defined as $p^{f(0)} = -j\omega\psi^{f(0)}$; $\hat{\sigma}_{ij}^{s(0)}$ is the stress in the solid phase without considering its coupling with the fluid phase; ϕ is the porosity; and $\bar{\rho}$ is the average mass density of the porous material, $(1 - \phi)\rho^s + \phi\rho_0^f$. c_{ijkl}^H, k_{ij}^H and $\theta^{s,pq}$ are the homogenized

macro properties of the solid phase (homogenized elastic tensors). θ^f, K^f and d_i^k are the homogenized macro properties of the fluid phase:

$$\hat{\sigma}_{ij}^{s(0)} = c_{ijkl}^H \varepsilon_{kl}^{s(0)}, \; k_{ij}^H = \frac{1}{|Y|} \int_Y c_{ijkl}^s \frac{\partial \eta_k(y)}{\partial y_l} dY, \; \theta^{s,pq} = \frac{1}{|Y|} \int_Y \frac{\partial \chi_k^{pq}(y)}{\partial y_k} dY. \quad (19)$$

$$\theta^f = \frac{1}{|Y|} \int_Y \frac{\partial \eta_k(y)}{\partial y_k} dY, \; d_i^k = \rho^f j\omega \langle \xi_i^k(y) \rangle. \quad (20)$$

The normal-incidence sound absorption coefficient is derived through Equation (21) using the acoustic tube model shown in **Figure 3-3** and by formulating the porous sound-absorbing material using the homogenized macroscopic properties (c_{ijkl}^H, k_{ij}^H, $\theta^{s,pq}$, θ^f, K^f, and d_i^k) and the macroscale governing equations (Equations (17) and (18)):

$$\alpha = 1 - |R|^2, \; R = \frac{e^{-jk^a(l_2-l_1)} - \frac{p_1}{p_2}}{\frac{p_1}{p_2} - e^{jk^a(l_2-l_1)}} e^{jk^a 2l_2}, \quad (21)$$

where k^a is the frequency of air. p_1 and p_2 are the sound pressures at distances l_1 and l_2, respectively, from the surface of the porous sound-absorbing material in the acoustic tube.
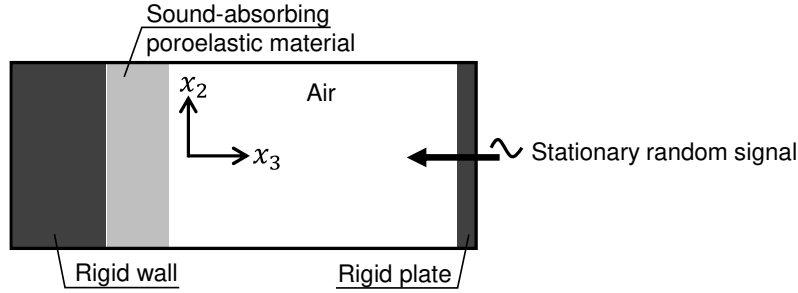
Figure 3-3. Acoustic tube model for calculating sound absorption coefficients at normal incidence.

2.2 Application of Computational Microstructure Modeling to Porous Materials

As shown in **Figure 3-4a**, a porous sound-absorbing material absorbs sound by con-verting the energy of sound waves entering the material into thermal energy through viscoelastic damping in the solid phase and through viscous damping and heat dissipation at the boundary between the fluid and solid phases. In other words, the more numerous the boundaries between the fluid and solid phases,

the greater the sound absorption. Furthermore, the effect of flow resistance emerges when sound waves

can penetrate the porous sound-absorbing material. Both of these requirements can be fulfilled by a

high-performance, porous, sound-absorbing material with a mixed structure consisting of a solid phase

as the base material and a fluid phase consisting of channels ranging from several tens of micrometers

to several millimeters.
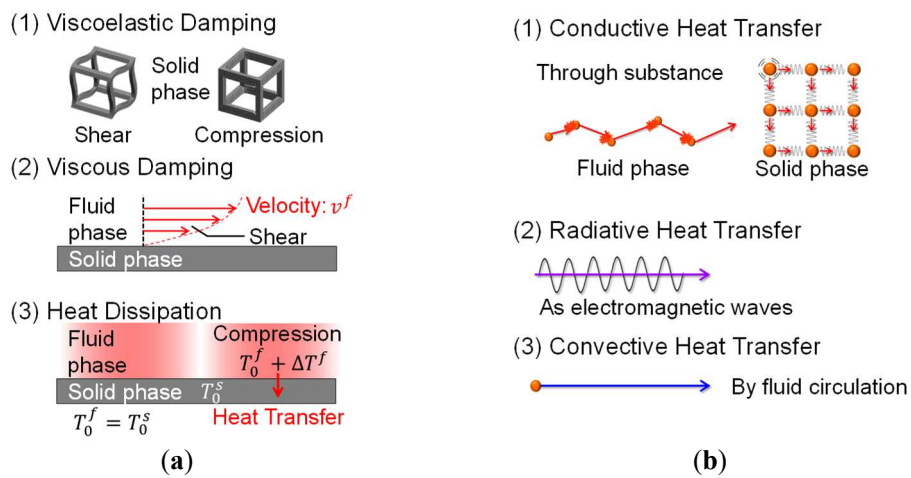
Figure 3-4. Mechanisms inside porous materials: (a) sound absorption and (b) heat transfer.

As shown in **Figure 3-4b**, a porous thermal-insulating material insulates by decreasing

contributions from the heat propagation paths inside the material: heat conduction in the solid and

fluid phases, heat radiation, and heat convection. Therefore, heat con-duction in the solid phase and

heat radiation and heat convection in the fluid phase can be reduced by a high-performance porous

insulation material that has a structure comprising a solid phase with a minimal volume fraction and a

fluid phase consisting of in-dependent spaces with diameters of less than several tens of micrometers.

Drastic sup-pression of the heat conduction in the fluid phase requires a mixed structure composed of

a fluid phase consisting of spaces with diameters on the order of tens of nanometers (about 70 nm or

less at atmospheric pressure); these diameters are less than the mean free path of air in the standard

state. Thus, in general, high-performance porous thermal-insulating materials do not function as sound absorbers because they do not have channels through which sound waves can pass, or the spaces in the fluid phase are too minute for sound waves to penetrate. Therefore, achieving both high sound absorption and high thermal insulation in the same material using the conventional approach is difficult.

In this chapter, we develop a porous material with excellent sound absorption and thermal insulation properties by materializing a sound absorption mechanism that does not allow sound waves to penetrate the material, which addresses this problem. Specifically, this porous material absorbs sound by causing the solid phase to vibrate violently when sound waves are incident, thereby inducing relative velocity and viscous damping at the boundary between the fluid and solid phases. The microscopic structure of this material is designed using the model shown in Section 2.1, and its performance is confirmed.

2.3 Preparation of Porous Materials and Performance Evaluation Methods

A prototype porous composite material consisting of PMS xerogel and CNFs was fabricated to resemble the microstructure and Young's modulus of the porous sound absorber model calculated in Section 3.1. The fabrication procedure accorded with Yamasaki et al. [21].

The normal-incidence sound absorption coefficients of the prepared xerogel specimens were measured using a WinZacMTX (Nihon Onkyo Engineering Co., Ltd., Tokyo, Japan; per JIS A 1405-2 [22] and ISO 10534-2 [23]). The inner diameter of the acoustic tube was 40 mm, and the measurement frequency range was 200–4800 Hz. The shape of the specimens was adjusted so that the specimens could be set in the tube without resistance and compression by pressing lightly with a finger. Furthermore, the sound absorption coefficient measurement was repeated several times after shaving a little around the specimens, and the final measurement results were obtained after confirming that

46

the resonant behavior was no longer present.

The flow resistance per unit thickness was measured using an AirReSys (Nihon Onkyo Engineering Co., Ltd. per ISO 9053-1 [24]). To prevent air leakage from around the specimens, the specimens were clamped in a special ring-shaped jig and set in the tube. At this time, the thickness was measured using a caliper to ensure that the specimens were not compressed. The differential pressure before and after the specimen was read when air flowed through the specimen at a velocity of 0.5 mm/s. The results were normalized using the flow velocity and specimen thickness.

The Young's and loss modulus were measured using a modulus measurement system (Nihon Onkyo Engineering Co., Ltd.). The specimen was placed on the base plate of a shaker, and a mass plate was placed on top of the specimen to construct a spring–mass system in the thickness direction. Resonance was generated by vibrating the base plate, and Young's modulus was calculated using the resonance frequency and the thickness of the specimen. The loss factor was calculated using the full width at half maximum of the peak near the resonance frequency.

The pore size distribution was determined using an AutoPore IV 9500 mercury intrusion porosimeter (Micromeritics Instruments Corporation, Norcross, GA, USA). A measurement specimen sized approximately 0.03–0.04 g was placed in a sealed glass container for measurement. The mercury intrusion pressure ranged from approximately 1 kPa to 400 MPa, and the measurement mode was pressure boosting. In this measurement method, specimens may be compressed during the measurement. Therefore, the pore size distribution in this measurement is for reference only.

Thermal conductivity was measured in a room under standard conditions using a simple measurement apparatus equipped with a heat flux sensor, thermocouples, an electric heater, and a thermal insulator, as shown in **Figure 3-5**. The heat flux sensor and a thermocouple were placed on the heater, which supplied a constant heat quantity. The test specimen, which was covered with an insulation material with a thermal conductivity of 0.0313 W/(m·K), was placed on the heater and the

thermocouple, and a thermocouple and a 1 mm-thick resin plate was placed on the test specimen for measurement. Thermal conductivity was derived from the measured heat flux and the temperatures above and below the specimen. Since this measurement apparatus is a simplified system, heat flow leaks out of the system. The thermal conductivity of the thermal-insulating material was 0.0313 W/(m·K) according to a steady-state thermal conductivity measurement system (HFM436/3/1 Lambda, NETZSCH-Gerätebau GmbH, Selb, Germany; per JIS A 1412-2 [25] and ISO 8301 [26]) and 0.0469 W/(m·K) according to this simple measurement apparatus. Therefore, as a reference value, a calibrated value of thermal conductivity was also calculated, assuming a constant percentage of heat flowing out of this simple system to measure thermal conductivity.
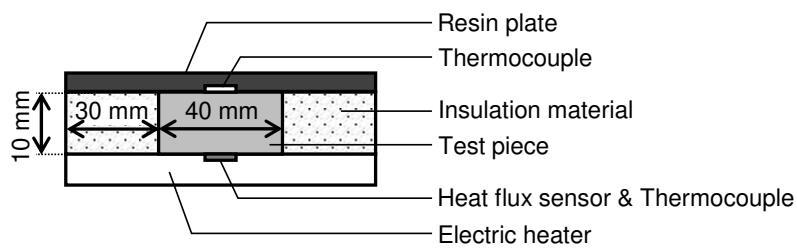
Figure 3-5. Simple thermal conductivity measurement apparatus.

3. Results and Discussion

3.1 Predicted Sound Absorption Coefficients

In this chapter, we made the solid phase vibrate violently due to incident sound waves to induce relative velocity and viscous damping at the boundary between the fluid and solid phases as a sound absorption mechanism without sound wave penetration, which is unlike the conventional method shown in Section 2.2. The main result of this verification is the goal of this study. The normal-incidence sound absorption coefficient was calculated using the model shown in Section 2.1 to verify the abovementioned concept. The Kelvin cell model in **Figure 3-6** was used to represent the

microstructure of the porous sound-absorbing material. Its unit cell (**Figure 3-6b**) consisted of a rectangle and a hexagon with bar-like ligaments. Given the same lengths w of the three sides of the unit cell ($w_x = w_y = w_z = w$), the sizes of the square and hexagonal vacancies were approximately 1/3w and 2/3w, respectively. The lengths w of the three sides of the unit cell were varied from 1 to 10 μm (the average pore size was approximately 0.5–5.2 μm), which are almost impenetrable to sound waves. The material of the ligaments was glass, and the material properties of the joints between ligaments were set, as shown in **Table 3-1**.

(a)   (b)
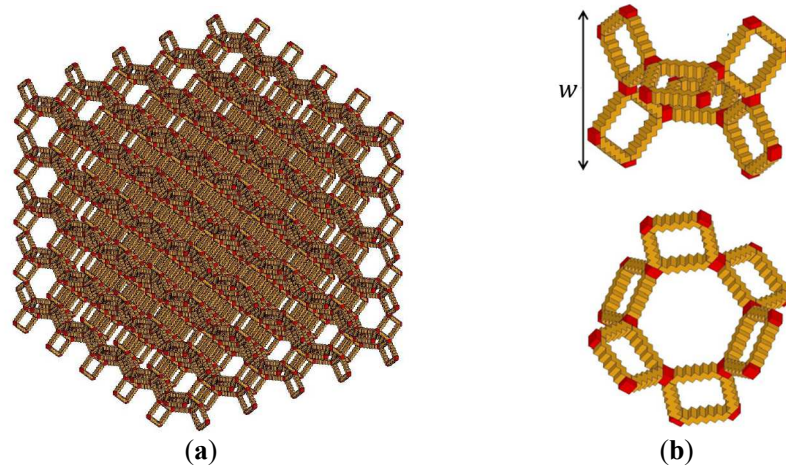
Figure 3-6. Calculation model of the microstructure of simulated porous material: (a) periodic structure and (b) unit cell.

Table 3-1. Material properties of ligaments and joints in calculation model.

	Young's Modulus (GPa)	Poisson's Ratio	Density (kg/m³)	Loss Factor
Glass	71.6	0.23	2200	0.002
Rubber 1	0.1	0.35	1100	0.3
Rubber 2	0.1	0.35	1100	0.1
Rubber 3	0.1	0.35	1100	0.5
Rubber 4	0.01	0.35	1100	0.3
Rubber 5	1	0.35	1100	0.3

Figure 3-7 shows the spectra of the predicted sound absorption coefficients. Table 3-2 shows the average sound absorption coefficients in the 1/3-octave band from 500 to 3150 Hz and from 1000 to 5000 Hz, commonly required for sound-absorbing materials in the automotive field.

(a)

(b)

(c)

(d)

(e)

(f)
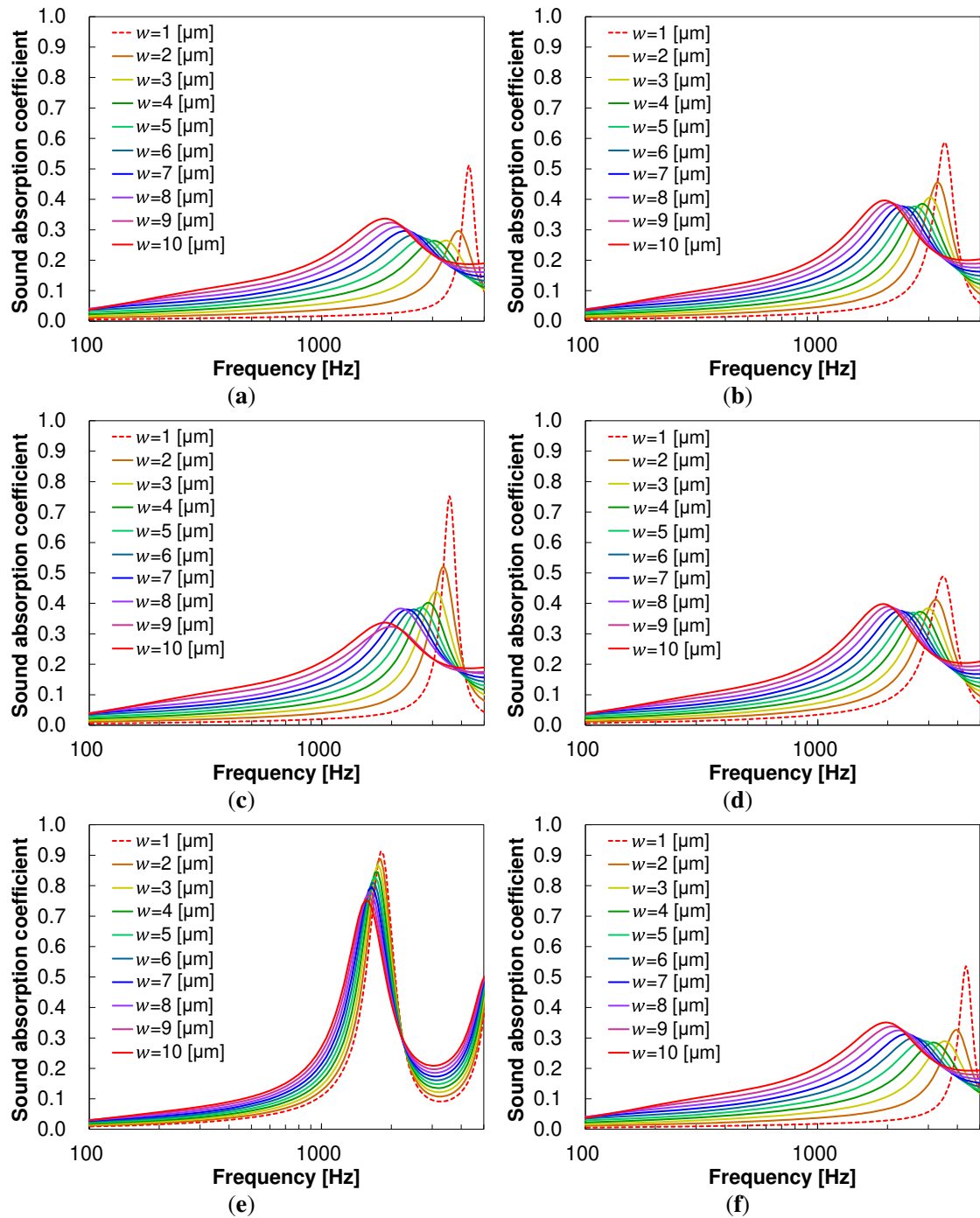
Figure 3-7. Spectra of predicted sound absorption coefficients of simulated porous material: (a) glass; (b) rubber 1; (c) rubber 2; (d) rubber 3; (e) rubber 4; and (f) rubber 5.

Table 3-2. Average 1/3-octave band absorption coefficients from 500 to 3150 Hz and from 1000 to 5000 Hz.

	500–3150 Hz Average α @ w = 1 μm	1000–5000 Hz Average α @ w = 1 μm	500–3150 Hz Average α @ w = 10 μm	1000–5000 Hz Average α @ w = 10 μm
Glass	0.02	0.07	0.23	0.25
Rubber 1	0.08	0.12	0.25	0.27
Rubber 2	0.06	0.10	0.23	0.25
Rubber 3	0.09	0.13	0.25	0.28
Rubber 4	0.22	0.29	0.31	0.39
Rubber 5	0.03	0.08	0.23	0.25

In the sound absorption coefficient spectra of both glass (**Figure 3-7a**) and rubber 1 (**Figure 3-7b**), the peak shifts to the higher-frequency side and narrows as w decreases. This peak shift is caused by the resonance frequency of the ligaments shifting to the higher-frequency side as w reduces and the bar-like ligaments become thinner and lighter. The narrowing of the peak is caused by a decrease in the number of sound waves penetrating the sound absorber, which reduces the contribution of viscous damping and heat dissipation due to air vibration and increases the contribution of viscoelastic damping and viscous damping due to the resonance of the sound absorber. Moreover, the sound absorption coefficient peaks are higher for all w values when the bonding points between the ligaments have rubber-like material properties. This may be due to (1) an increase in viscoelastic damping caused by the distortion of the rubber at the joint or (2) an increase in viscous damping caused by an increase in the resonance amplitude of the ligament due to a smaller ratio of the spring constant at the joint to the ligament weight. The results were compared by varying only the loss factor or Young's modulus at the joint to determine the cause.

First, the sound absorption coefficient spectra of rubber 1 (**Figure 3-7b**), rubber 2 (**Figure 3-7c**),

and rubber 3 (**Figure 3-7d**), which differ only in loss factor, were compared. The results show that a lower loss factor at the joint makes the peak of the sound absorption coefficient more intense. Given a larger contribution of viscoelastic damping caused by the distortion of the rubber at the joint, a higher loss factor at the joint improves the peak value due to the higher thermal conversion effect caused by the distortion. On the contrary, given a larger contribution of viscous damping caused by the larger amplitude of the ligament resonance, a lower loss factor at the joint enhances the peak value because the resonance is not suppressed. Therefore, the contribution of viscous damping to the sound absorption phenomenon is higher than that of viscoelastic damping. The average sound absorption coefficients of rubber 1, rubber 2, and rubber 3 in the 1/3-octave band were also compared (**Table 3-2**). The results show that the average sound absorption coefficient is slightly higher at higher loss factors at the joint. This is because a higher loss factor at the joint widens the resonance frequency of the ligament, which in turn widens the frequency range of the sound absorption coefficient peak, resulting in a slightly larger average sound absorption coefficient.

Next, the sound absorption coefficient spectra of rubber 1 (**Figure 3-7b**), rubber 4 (**Figure 3-7e**), and rubber 5 (**Figure 3-7f**), which differ only in the Young's modulus, were compared. The peak frequency of the sound absorption coefficient shifts to the lower-frequency side at smaller Young's moduli at the joint; the peak value is significantly high for rubber 4 in particular. This peak shift to the lower-frequency side is caused by the shift of the resonance frequency of the ligament to the lower-frequency side due to the decrease in the spring constant of the joint. The improvement in the peak value is caused by the amplification of the viscous damping at the boundary between the ligament and the stagnant air inside the sound-absorbing material, which occurs as the ratio of the spring constant of the joint to the ligament weight decreases and the resonance amplitude of the ligament increases.

These results suggest that the sound absorption performance can be improved by increasing the resonance amplitude of the ligament and amplifying the viscous damping at the boundary between the

fluid and solid phases, thereby verifying the concept of a sound absorption mechanism without sound wave penetration.

3.2 Performance Evaluation Results

Figure 3-8 shows a scanning electron microscopy (SEM) image of the PMS xerogel. Preparation of a high-porosity structure using only a PMS network with varied material properties of the ligaments and joints is difficult. Therefore, we developed a composite of PMS xerogel and CNFs.
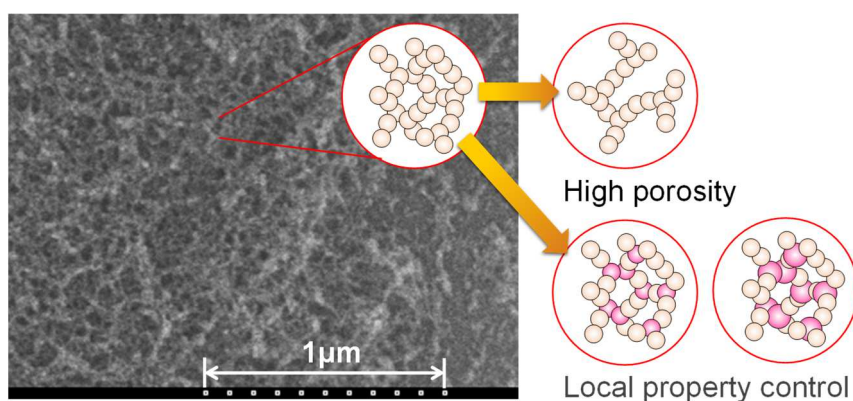
Figure 3-8. Scanning electron microscopy image of poly(methylsiloxane) (PMS) xerogel.

The CNF–PMS xerogel composite was synthesized using the raw material formulation in **Table 3-3** as follows: A CNF dispersion was mixed with a 5 mmol/L aqueous acetic acid solution, and the mixture was stirred using a stirrer at 1150 rpm for 15 min at room temperature. Urea and n-hexadecylammonium bromide (CTAB) were then dissolved in the mixture, and dimethyldimethoxysilane (DMDMS) and methyltrimethoxysilane (MTMS) were added to the mixture for hydrolysis. The samples were allowed to gel and age at 80 °C, washed, solvent-exchanged, and dried to obtain dried samples. Finally, the samples were dried at 120 °C for 1 h. The CNF dispersions used were Rheocrysta (2 wt% aqueous dispersions of CNFs oxidized using 2,2,6,6-

tetramethylpiperidine-1-oxyl; DKS Co., Ltd., Kyoto, Japan) and hydrophobic CNF dispersions prototyped by DKS Co., Ltd.

Table 3-3. Raw material formulation of composite cellulose nanofibers (CNFs) and PMS xerogel. CTAB—n-hexadecylammonium bromide; MTMS—methyltrimethoxysilane; DMDMS—dimethyldimethoxysilane.

	Original PMS Xerogel	Diluted PMS Xerogel	CNF PMS Xerogel	Hydrophobic CNF PMS Xerogel
CTAB/g	0.4	0.2	0.2	0.2
Urea/g	3.0	3.0	3.0	3.0
Acetic acid/ml	10	10	10	10
CNF dispersion/g	0	0	1.0	0.2
MTMS/ml	3.0	1.5	1.5	1.5
DMDMS/ml	2.0	1.0	1.0	1.0

The appearance of the produced PMS xerogels is shown in **Figure 3-9**. The original PMS xerogel (**Figure 3-9a**) was synthesized as a homogeneous dry gel. Its porosity, calculated using the bulk and skeletal densities, was 89.5%. The aged and diluted PMS xero-gel (**Figure 3-9b**), in which the amount of alkoxysilane precursors was decreased to half its volume to increase its porosity, did not form a gel structure after aging; it remained in solution form. The CNF–PMS xerogel composite (**Figure 3-9c**), in which the amount of alkoxysilane precursors was also decreased to half its volume, was synthesized as a dry gel. However, it was mechanically weak, and its surface was damaged when something came in contact with the specimen. Its porosity was 94.2%. The hydrophobic CNF–PMS xerogel composite (**Figure 3-9d**) was a tougher dry gel than the CNF–PMS xerogel composite. Its porosity was 93.2%. A moderate interaction or inter-dispersion was observed between the sol framework and CNFs, and the toughness of the gel depended on the balance between them.
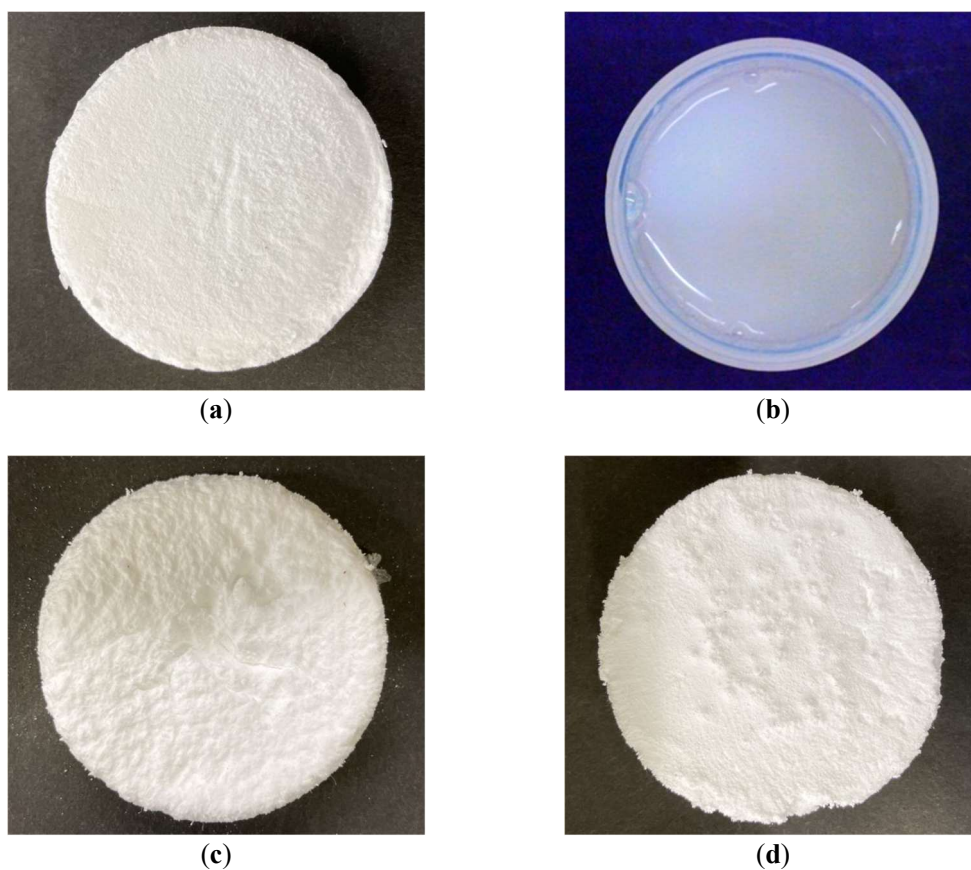
Figure 3-9. External appearance of synthesized PMS xerogels: (a) original PMS xerogel; (b) diluted PMS xerogel after aging; (c) CNF–PMS xerogel composite; and (d) hydrophobic CNF–PMS xero-gel composite.

SEM images of the original PMS xerogel and the hydrophobic CNF–PMS xerogel composite are shown in **Figure 3-10**. In the original PMS xerogel, gel particles with diameters of several micrometers are strung together to form the three-dimensional porous structure. The hydrophobic CNF–PMS xerogel composite comprises gel particles with a broad size distribution (diameters ranging from several hundred nanometers to several micrometers). No fibrous structures are observed. The CNF is the substance that adheres to the periphery of the gel particles to the extent that it covers the particle shape of the gel particles (**Figure 3-10d**). The hydrophobic CNF–PMS xerogel composite has a higher porosity than the original PMS xerogel, suggesting that the CNFs also

function as binders. The CNFs are sparsely distributed, indicating that gel particles are exposed in places. As shown in Kobayashi et al. [27], it can be inferred that gel particles coated with C-C bond-dominated CNFs exhibit a higher modulus than the exposed gel particles.
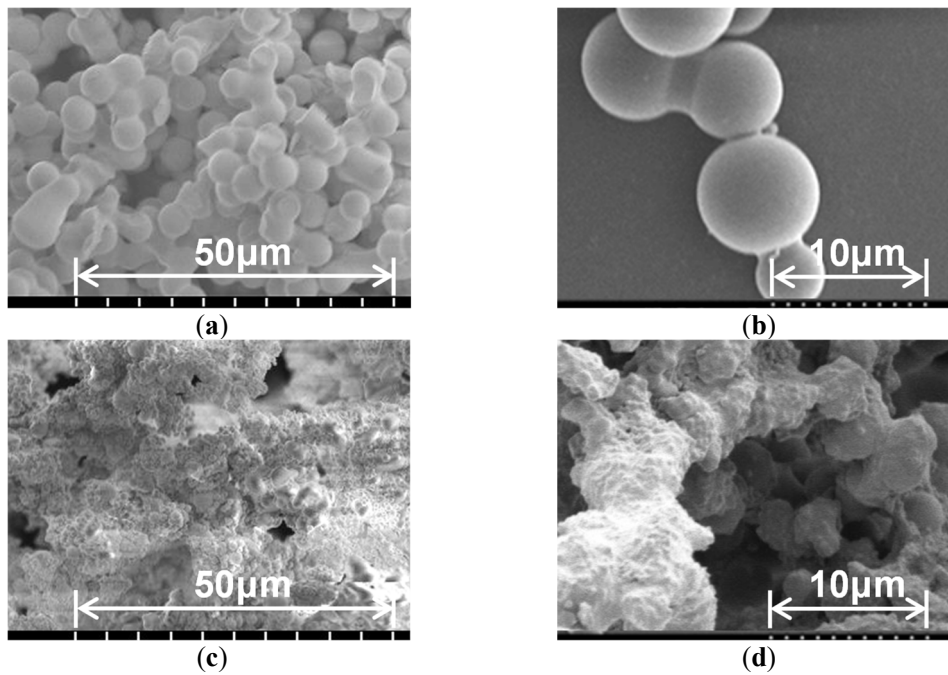
Figure 3-10. SEM images of synthesized PMS xerogels: (a) original PMS xerogel; (b) original PMS xerogel; (c) hydrophobic CNF–PMS xerogel; (d) hydrophobic CNF–PMS xerogel.

Table 3-4 shows the measured properties of the original PMS xerogel and the hydrophobic CNF–PMS xerogel composite, and **Figure 3-11** shows their measured normal-incidence sound absorption coefficients. The hydrophobic CNF–PMS xerogel composite exhibits an average sound absorption coefficient of 0.45 from 500 to 3150 Hz. This value is higher than that of the original PMS xerogel despite the smaller thickness of the hydrophobic composite; it is also approximately 1.7 times that of a porous sound-absorbing material commonly used in automobiles (3M Thinsulate; Table 4). The Young's modulus of the hydrophobic CNF–PMS xerogel composite is 1/20 times that of the original PMS xerogel. The loss factor of the hydrophobic CNF–PMS xerogel composite is four times that of

56

the original PMS xerogel. The raw material formulation and synthesis conditions of the polysiloxane network are equivalent, and the molecular structure and physical properties of the network are considered to be almost the same. Therefore, the difference in loss factor suggests that the hydrophobic CNF–PMS xerogel composite has a higher fraction of mechanically flexible sites, causing more enhanced sound dissipation at the flexible sites. From these results and **Figure 3-10d**, we infer that the hydrophobic CNF–PMS xerogel composite forms a structure similar to the rubber 4 model (Section 3.1), with rigid sites where the gel particles are covered with CNFs and flexible sites where the gel particles are exposed.

Moreover, as shown in the calculation model of rubber 4 in Section 3.1, the ligament of the hydrophobic specimen resonates more easily, which improves the sound absorption coefficient. The sound absorption coefficient of the hydrophobic CNF–PMS xerogel composite does not decrease at frequencies above 1000 Hz and remains high. The flow resistance per unit thickness is 1.35×10^6 N·s/m^4 for the original PMS xerogel and 5.54×10^5 N·s/m^4 for the hydrophobic CNF–PMS xerogel composite, suggesting that the hydrophobic specimen with higher porosity is penetrated by sound waves to a greater extent. This helps enhance the sound absorption coefficient in the high-frequency range. The peak diameter in the pore size distribution of the original PMS xerogel is 8.1 μm, which is larger than the upper limit considered in the calculation model, namely, $w = 10$ μm (the average pore size is approximately 5.2 μm). In addition, the pore size may be measured smaller than the actual due to the deformation of this material during the measurement. Therefore, the flow resistance is lower than expected.
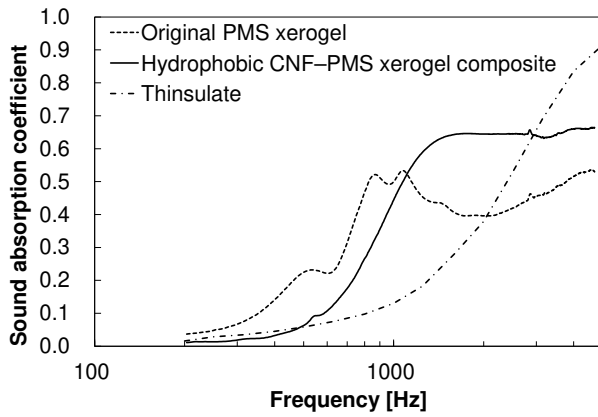
Figure 3-11. Measured normal-incidence sound absorption coefficients of synthesized PMS xerogels.

Table 3-4. Properties of original PMS xerogel and hydrophobic CNF–PMS xerogel composite.

	Original PMS Xerogel	Hydrophobic CNF PMS Xerogel	3M^{TM} Thinsulate^{TM} (St. Paul, MN, USA)
Porosity [%]	89.5	93.2	-
Pore size distribution Peak size [μm]	8.1	-	-
Thickness [mm]	10	8	10
Flow resistivity [N s/m^4]	1.35×10^6	5.54×10^5	-
Bulk Density [kg/m^3]	168.2	88.4	-
Young's modulus [Pa]	3.0×10^4	1.5×10^3	-
Loss factor	0.250	0.939	-
500–3150 Hz Average Sound absorption coefficient	0.39	0.45	0.27
1000–5000 Hz Average Sound absorption coefficient	0.43	0.62	0.49
Thermal conductivity [W/(m·K)]	0.0371 (0.0248)	0.0378 (0.0252)	0.0536 (0.0358)

The thermal conductivity of the original PMS xerogel is 0.0371 W/(m·K) (the calibrated value is 0.0248 W/(m·K)), which was measured using the simple thermal conductivity measurement apparatus

shown in **Figure 3-5**. The thermal conductivity of the hydrophobic CNF–PMS xerogel composite, also measured using the simple apparatus, is 0.0378 W/(m·K) (the calibrated value is 0.0252 W/(m·K)). Although this is a reference value, this is approximately 1.4 times the insulation performance of 3M Thinsulate. Therefore, a porous material with both excellent sound absorption and thermal insulation was developed through computational microstructure modeling.

4. Conclusions

A hydrophobic CNF–PMS xerogel composite was developed by computational microstructure modeling. Compared with the original PMS xerogel, the hydrophobic composite material exhibited excellent sound absorption while maintaining high thermal insulation and high porosity. This material can be used in unexposed parts, such as the inside of interior parts of automobiles, and demonstrates excellent sound absorption and thermal insulation properties. In addition, the material may be strengthened by improving the interaction or inter-dispersion between the PMS framework and CNFs. A tougher version of this material can be used in the parts subjected to harsh conditions in the future, such as prime movers and automobile drive units.

5. References

[1] Gao, K.; van Dommelen, J.A.W.; Geers, M.G.D. Investigation of the effects of the microstructure on the sound absorption performance of polymer foams using a computational homogenization approach. Eur. J. Mech. A Solids 2017, 61, 330–344.

[2] Gao, K.; van Dommelen, J.A.W.; Göransson, P.; Geers, M.G.D. A homogenization approach for characterization of the fluid–solid coupling parameters in Biot′s equations for acoustic poroelastic materials. J. Sound Vib. 2015, 351, 251–267.

[3] Zieliński, T.G. Microstructure-based calculations and experimental results for sound absorbing porous layers of randomly packed rigid spherical beads. J. Appl. Phys. 2014, 116, 034905 .

[4] Perrot, C.; Chevillotte, F.; Tan Hoang, M.; Bonnet, G.; Bécot, F.-X.; Gautron, L.; Duval, A. Microstructure, transport, and acoustic properties of open-cell foam samples: Experiments and three-dimensional numerical simulations. J. Appl. Phys. 2012, 111, 014911.

[5] Lee, C.-Y.; Leamy, M.J.; Nadler, J.H. Frequency band structure and absorption predictions for multi-periodic acoustic com-posites. J. Sound Vib. 2010, 329, 1809–1822.

[6] Shrestha, S.S.; Tiwari, J.; Rai, A.; Hun, D.E.; Howard, D.; Desjarlais, A.O.; Francoeur, M.; Feng, T. Solid and gas thermal conductivity models improvement and validation in various porous insulation materials. Int. J. Therm. Sci. 2023, 187, 108164.

[7] Zhou, Y.; Huang, B.; Cao, B.-Y. Vibrational modes with long mean free path and large volumetric heat capacity drive higher thermal conductivity in amorphous zeolitic imidazolate Framework-4. Mater. Today Phys. 2021, 21, 100516.

[8] Qiu, B.; Bao, H.; Zhang, G.; Wu, Y.; Ruan, X. Molecular dynamics simulations of lattice thermal conductivity and spectral phonon mean free path of PbTe: Bulk and nanostructures. Comput. Mater. Sci. 2012, 53, 278–285.

[9] Davoudabadi, F.M.; Jamshidi, A.M.; Jeddi, A.A. Sound absorption of warp knitted spacer fabrics based on knit structure and nanofiber enhancement. J. Ind. Text. 2022, 51, 1539–1557 .

[10] Wu, C.M.; Chou, M.H. Polymorphisim, piezoelectricity and sound absorption of electrospun PVDF membranes with and without carbon nanotubes. Compos. Sci. Technol. 2016, 127, 127–133.

[11] Shen, L.; Zhang, H.; Lei, Y.; Chen, Y.; Liang, M.; Zou, H.   Hierarchical pore structure based on cellulose nanofiber/ melamine composite foam with enhanced sound absorption performance. Carbohydr. Polym. 2021, 255, 117405.

[12] Zhao, X.D.; Ying, W. Optimization and characterization of polyurethane electro-spun nano-membranes used for the surfaces of sound absorbent multi-layer sheets. J. Macromol. Sci. Phys. B 2021, 60, 647–662.

[13] Neslihan, K.; Ilkay, O.Y.; Nuray, U.; Aysen, O.; Cafer, K. Sound absorption and thermal insulation properties of composite thermoplastic polyurethane/polystyrene (TPU/PS) nanofiber web and TPU nanofiber web and PS-extracted TPU/PS microfi-ber web. J. Ind. Text. 2022, 51, 7963S–7982S.

[14] Zahra, M.S.; Hasina, B.; Stefan, S.; Kirill, V.H.; Wim, J.M. A review on silica aerogel-based materials for acoustic applica-tions. J. Non-Cryst. Solids 2021, 562, 120770.

[15] Katsura, D.; Yamamoto, T.; Yamakawa, K.; Hatakeyama, N.; Miura, R.; Okajima, J.; Inaba, K.; Ishizawa, Y.; Ochiai, H.; Yu-kawa, H.; et al. Development of thermal management and noise/vibration control material model tech-nology by model-based research (MBR) 1st report. In Proceedings of the JSAE Annual Congress (Spring) Proceedings, Online, 26–28 May 2021; p. 20215301.

[16] Yamamoto, T.; Maruyama, S.; Terada, K.; Izui, K.; Nishiwaki, S. A generalized macroscopic model for sound absorbing po-roelastic media using a homogenization method. Comput. Methods Appl Mech Eng 2011, 200, 251–264.

[17] Gilbert, R.P.; Mikelić, A. Homogenizing the acoustic properties of the seabed: Part I. Nonlinear. Anal. 2000, 40, 185–212.

[18] Clopeau, T.; Ferrín, J.L.; Gilbert, R.P.; Mikelić, A. Homogenizing the acoustic properties of the seabed, part II. Math. Comput. Model. 2001, 33, 821–841.

[19] Sanchez-Palencia, E. Non-homogeneous Media and Vibration Theory, Lecture Notes in Physics; Springer: Berlin/Heidelberg, Ger-many, 1980; Volume 127.

[20] Yamamoto, T.; Maruyama, S.; Terada, K.; Izui, K.; Nishiwaki, S. Prediction of sound absorption coefficients of poroelastic media by the homogenization method. In Proceedings of the 40th International Congress and Exposition on Noise Control Engineering 2011, INTER-NOISE, Osaka, Japan, 4–7 September 2011; Volume 2011, pp. 1989–1996.

[21] Yamasaki, S.; Sakuma, W.; Yasui, H.; Daicho, K.; Saito, T.; Fujisawa, S.; Isogai, A.; Kanamori, K. Nanocellulose xerogels with high porosities and large specific surface areas. Front. Chem. 2019, 7, 316.

[22] JIS A 1405-2:2007; Acoustics -- Determination of sound absorption coefficient and impedance in impedance tubes -- Part 2: Transfer-function method. Japanese Industrial Standards Committee; Tokyo, Japan, 2007.

[23] ISO 10534-2:2023; Acoustics -- Determination of acoustic properties in impedance tubes -- Part 2: Two-microphone technique for normal sound absorption coefficient and normal surface impedance. International Organization for Standardization; Ge-neva, Switzerland, 2023.

[24] ISO 9053-1:2018; Acoustics -- Determination of airflow resistance -- Part 1: Static airflow method. International Organization for Standardization; Geneva, Switzerland, 2018.

[25] JIS A 1412-2:1999; Test method for thermal resistance and related properties of thermal insulations -- Part 2 : Heat flow meter apparatus. Japanese Industrial Standards Committee; Tokyo, Japan, 1999.

[26] ISO 8301:1991; Thermal insulation -- Determination of steady-state thermal resistance and related properties -- Heat flow meter apparatus. International Organization for Standardization;

Geneva, Switzerland, 1991.

[27] Kobayashi, Y.; Saito, T.; Isogai, A. Aerogels with 3D Ordered Nanofiber Skeletons of Liquid-CrystallineNanocellulose Deriv-atives as Tough and Transparent Insulators. Angew. Chem. Int. Ed. 2014, 53, 10394–10397.

Chapter 4: Sound-Absorbing, Thermal-Insulating Material Based on Non-Woven Fabrics Mixed with Aerogel Particles

1. Introduction

Thermal conductivity is a key indicator of the performance of thermal-insulating materials. High-performance porous thermal insulation insulates by reducing the heat conduction pathways inside the material: heat conduction in solids, heat conduction in gases, heat convection in gases, and heat radiation. Therefore, it is recognized that the thermal conductivity of a thermal-insulating material depends on the structure inside the material [1–3]. Specifically, the porosity or bubble ratio should be increased to reduce heat conduction in solids, or heat conduction path of solids should be lengthened. Furthermore, to reduce heat conduction in gases, heat conduction in gases, and heat radiation, the diameter of porosity and bubbles should be reduced from tens of nanometers to tens of micrometers, or each space should be made independent of the other. On the other hand, the sound absorption coefficient is a key indicator of the performance of sound-absorbing materials. High-performance porous sound-absorbing materials absorb sound by converting sound wave energy into heat energy through viscoelastic damping in solids and viscous damping and heat dissipation at the boundary between gas and solid, which is caused by sound wave penetration into the material. Therefore, it is recognized that, as with thermal insulation, the sound absorption coefficient of a sound-absorbing material depends on the structure inside the material [4–8]. Specifically, to improve viscoelastic damping in solids, the loss factor of the solid should be increased, or the solid should be more easily distorted. Furthermore, to improve viscous damping and heat dissipation at the boundary between gas and solid, the boundary area between gas and solid should be increased, or the path of the gas through which sound waves pass should be lengthened. Increasing the boundary area between gas and solid inside the material or lengthening the path of the gas makes it more difficult for sound waves to

penetrate the material. Balancing the two, the diameter of porosity and bubbles should be reduced from tens of micrometers to several millimeters in diameter, and each space should be connected to form a flow path for sound waves to pass through. Thus, it is difficult to achieve both thermal and acoustic properties for porous sound-absorbing materials and porous thermal-insulating materials because the size and structure of the porosity and bubbles for optimum performance are very different.

In recent years, experimental studies have been conducted on nanofiber-based composite materials that achieve both thermal and acoustic properties: Polyvinylidene fluoride by Wu et al. (2016) [9], cellulose by Shen et al. (2021) [10], polyurethane by Zhao et al. (2021) [11], thermoplastic polyurethane (TPU)/polystyrene (PS) by Karaca et al. (2022) [12], polyacrylonitrile (PAN) by Farahani et al. (2022) [13], and other materials have been studied. For example, a study by Karaca et al. on TPU/PS-BSE nanofibers prepared using electrospinning solutions [12] showed that they achieve both 0.050 W/(m·K) as thermal conductivity and 0.5–0.6 as the sound absorption coefficient at about 1000 Hz. Experimental studies have also been conducted on silica aerogel-based materials that achieve both thermal and acoustic properties. With regard to silica and silica–polymer hybrid aerogels, polyimide–silica aerogel composites by Yan et al. (2014) [14], sodium dodecyl sulfate-doped gelatin–silica hybrid aerogels by Sachithanadam et al. (2016) [15], monolithic aerogels and granular aerogels by Merli et al. (2018) [16], and other materials have been studied. With regard to silica aerogel–textiles composites, non-woven polyethylene terephthalate (PET)–silica aerogel blankets by Oh et al. (2009) [17], non-woven PET–aerogel composites by Küçük et al. (2012) [18], cotton non-woven fabric–silica aerogel blanket by Motahari et al. (2015) [19], silica aerogel blanket prepared from sols with varying silica content by Ramamoorthy et al. (2017) [20], aerogel–polyethylene (PE)/PET non-woven bonded blankets by Yang et al. (2019) [21], in situ synthetic silica aerogel/PET blankets by Talebi et al. (2019) [22], glass fiber blankets impregnated with aerogel powder (2–40 μm particle size) by Zahra et al. (2021) [23], and other materials have been studied. For example, a study by Zahra et al. on glass fiber

blankets impregnated with aerogel powder [23] showed that the sound absorption coefficient above 700 Hz can only reach about 0.4 at a thickness of 10 mm. Despite these developments, there remains a significant gap in mathematical modeling to comprehend the key physical mechanisms behind the acoustic behavior of aerogels.

Therefore, the authors employed a computational microstructural modeling approach based on materials model-based research (MBR) [24, 25] to predict the thermal insulation and sound absorption properties of porous materials. This method facilitated the development of a porous material that exhibits exceptional thermal insulation and sound absorption properties. The material was engineered by integrating aerogel particles, which are characterized by multiple independent spaces with diameters of several tens of nanometers, into a polyethylene terephthalate (PET) fiber non-woven fabric. The appropriate particle size and particle shape and blending ratio were crucial for achieving the desired properties. The result is a non-woven fabric with heat-insulating and sound-absorbing properties that has improved performance with aerogel particles.

In Chapter 3, we discussed a material that insulates and absorbs sound by damping sound waves through vibration in a structure containing fine porous and soft sites. In this study, by incorporating nanoporous ellipsoidal particles with long sides ranging from tens to hundreds of microns into non-woven fabrics with voids of similar dimensions, we enhanced the labyrinthine nature of the sound waves' traversal through the material. This structure allows the nanoporous particles to provide thermal insulation, while the microporous voids facilitate sound absorption, achieving superior performance in both aspects.

2. Materials and Methods

2.1 Computational Microstructure Modeling Approach Applied to Porous Materials

The computational microstructure modeling approach to predicting the sound absorption properties of porous materials involves the asymptotic homogenization method. This method accounts for the viscosity in the fluid phase and the attenuation due to heat dissipation. It enables the direct derivation of equivalent properties from the microstructure, which is essential for predicting the dynamic properties of the porous absorber. These equivalent properties, when applied to a model of the porous sound absorber, allow for the determination of macroscopic properties such as the sound ab-sorption coefficient. For details on the equations required for each calculation, please refer to Chapter 3. The equations required to derive equivalent properties (microscopic properties) from the microstructure of the porous material and to derive the sound absorption coefficient of the porous material (macroscopic properties) from the derived equivalent properties were implemented in COMSOL Multiphysics (Ver. 5.6, Comsol AB, Stockholm, Sweden). COMSOL Multiphysics with this implemented equation was used to calculate the microscopic and macroscopic properties in this study.

Porous sound absorbers convert the energy of incoming sound waves into heat through viscoelastic damping in the solid phase, viscous damping at the boundary be-tween the fluid and solid phases, and heat dissipation. The effectiveness of sound absorption increases with the number of boundaries between the fluid and solid phases within the material. Therefore, a finer skeletal diameter, ideally at the level of several micrometers, enhances the performance of the sound-absorbing material, although it must also allow for sound wave penetration. Conversely, the skeletal diameter of a high-performance heat insulator should be at the nanometer level to form independent spaces of several tens of nanometers. Since these requirements are inherently contradictory, a novel structure was devised that combines aerogel particles with multiple independent spaces of several tens of nanometers in diameter

within the mesh-like channels of the non-woven fabric. This allows for effective sound wave penetration. Using the computational microstructural modeling approach, we designed optimal shapes, particle sizes, and quantities of aerogel particles for this porous material and confirmed their performance (**Figure 4-1**). The meshing sequence for the microstructure was physics-controlled mesh, and for the calculation of microscopic properties, the minimum element size of the solid section was set to be 10 µm or less. In the calculation of macroscopic properties, physics-controlled mesh was also used, and the minimum element size was set to be 9 mm or less.
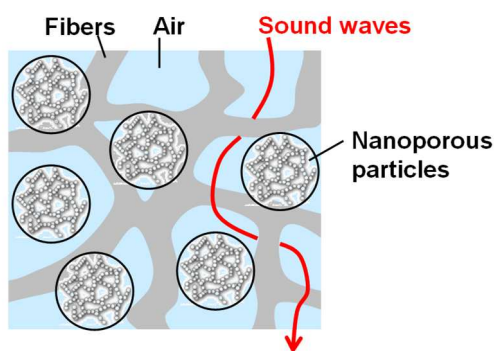
Figure 4-1. Structure of the devised porous material.

2.2 Preparation of Porous Materials and Performance Evaluation Methods

A material mirroring the microstructure of the porous sound-absorbing material modeled in Section 2.1 was fabricated. Specifically, non-woven fabrics incorporating particles were produced by mixing pre-mixed polyethylene terephthalate (PET) fibers with a diameter of approximately 7 µm at 60 wt% and low-melt PET fibers with a diameter of approximately 14 µm at 40 wt%.

Sample Opener OP-400 (Takeuchi Seisakusho Co., Ltd., Osaka, Japan) was used for fiber opening and mixing (**Figure 4-2a**). The feed conveyor was set at 0.25 m/min and the cylinder roller at 600 rpm. Each fiber clump, pre-measured to a predetermined ratio, was mixed by hand and placed on the feed

conveyor so that it was evenly distributed. The sample opener was used to open and mix the fibers twice.

Sample Roller Card SRC-400 (Takeuchi Seisakusho Co., Ltd., Osaka, Japan) was used to card the mixed fibers (**Figure 4-2b**). The feed conveyor was set at 0.25 m/min, the cylinder roller at 300 rpm, and the doffer roller at 5 m/min. The fibers mixed by the Sample Opener were placed evenly on the feed conveyor. Carding was performed twice to produce a PET non-woven base sheet with a width of 40 cm and an areal density of approximately 4 g/m^2.

A prototype powder feeder (Takeuchi Seisakusho Co., Ltd., Osaka, Japan) for this study was used to spread particles onto a non-woven base sheet (**Figure 4-2c**). The powder feeder is equipped with a rotating rubber spatula that shears the particles between the spatula and the walls of the particle stock case and feeds the particles. The bottom of the particle stock case has a hole whose size can be changed, allowing particles of a predetermined size or smaller to be spread at a predetermined rate on a non-woven base sheet with a width of 40 cm. Aerogel particles (Aerogel P100, 0.1 to 4 mm diameter, approximately 0.15 g/cm^3, Cabot Corporation, Boston, MA, USA) were used. The elasticity of the rubber spatula and the rotation speed were adjusted so that the particle shape and size distribution were within the target range. A PET non-woven base sheet was passed under the powder feeder at a feed rate of 5 m/min to produce a particle spread PET non-woven base sheet.

The base sheets were stacked to achieve the targeted bulk density, preheated at 150 °C for 10 min, and then cold pressed to 10 mm thickness with a flat die at 80 °C. Thus, a 300 × 300 mm PET non-woven fabric test piece and an aerogel particle-mixed non-woven fabric test piece were prepared. A specimen of the same dimensions was also prepared by laminating one side of this non-woven fabric with a high-airflow-resistance skin material (thickness: 0.20 mm) [26], developed jointly with MAEDAKOSEN CO., LTD. (**Figure 4-3**).

The bulk density, fiber content, and particle content of the test pieces were measured using an electronic balance after the specimens were placed in a crucible and heated in an electric furnace at 600 °C for 4 h and then sufficiently cooled. Fiber and particle content were derived from the results of the same measurements on test pieces with 100% fiber content and 100% particle content, respectively.

Structural analysis of the test pieces was performed using an X-ray CT nano3DX (Rigaku Corporation, Tokyo, Japan).

The normal-incidence sound absorption coefficient was measured using the Impedance Tube Kit Type 4206 (Brüel & Kjær, Nærum, Denmark; per ISO 10534-2 [27]). The measurement frequency range was 50–1600 Hz. The measurements were calculated in 1/3-octave bands. The inner diameter of the acoustic tube was 100 mm. The diameter of the specimen was adjusted so that the specimen could be set into the acoustic tube without resistance. Furthermore, the ambient shape of the specimen was fine-tuned, and the sound absorption coefficient measurement was repeated to confirm that the resonance behavior was no longer present, and the final measurement results were obtained.

Flow resistivity, which influences the sound absorption coefficient, was measured using the airflow resistivity meter SIGMA (Mecanum Inc., Sherbrooke, QC, Canada; per ISO 9053-1 [28]). Pressure drop data were measured when air flowed through the specimen at a low flow velocity of 0.5 mm/s. Flow resistivity was calculated from the measured pressure drop, flow velocity, and specimen thickness.

Thermal conductivity was measured using the steady-state thermal conductivity measuring device HFM436/3/1 Lambda (NETZSCH-Gerätebau GmbH, Selb, Germany; per ISO 8301 [29]).
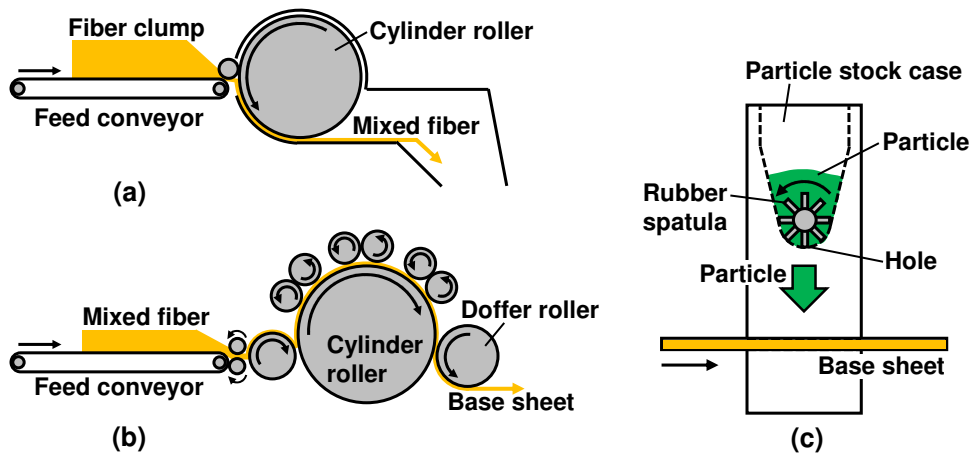
Figure 4-2. Non-woven base sheet making equipment: (a) Sample Opener; (b) Sample Roller Card; (c) Prototype Powder Feeder.
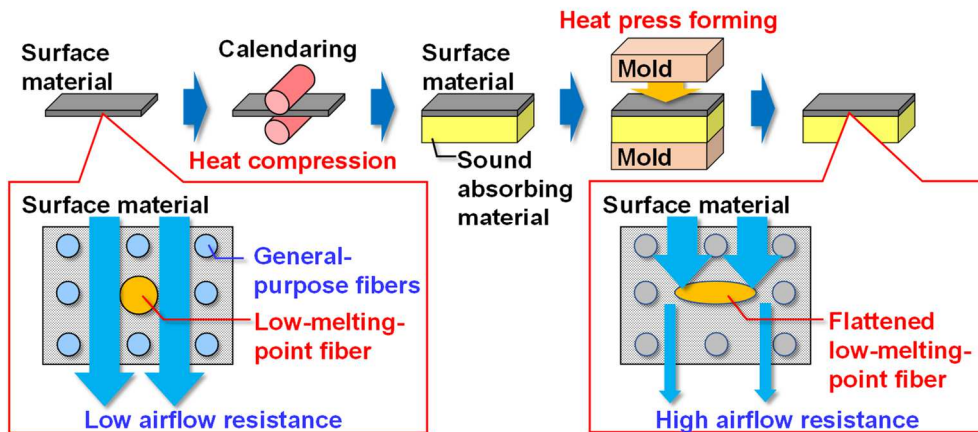
Figure 4-3. High-airflow-resistance surface material laminated to this non-woven fabric.

3. Results and Discussion

3.1 Prediction Calculation Result of Sound Absorption Coefficient

The computational geometry is depicted in **Figure 4-4**. The modeled structure mimics a non-woven fabric with a fiber diameter of 10 µm and a porosity of 99%, with a uniform unit cell size of w = 1000 µm ($w_x = w_y = w_z = w$) (**Figure 4-4a**). Particle A in the model presented in **Figure 4-4b** is a sphere with a diameter of 220 µm, while particle B in **Figure 4-4c** is an ellipsoid measuring 440×880

× 27.5 µm. Particles A and B have equivalent volumes. **Figure 4-4d** illustrates the geometry of **Figure 4-4a** augmented with a fiber mass equivalent to four particles A. The specific gravity of the fiber is assumed to be 1.38 g/cm^3 (PET), and that of particles A and B is 0.15 g/cm^3 (aerogel). The bulk densities of each configuration and the positions of the centers of gravity of the particles are detailed in **Table 4-1**.
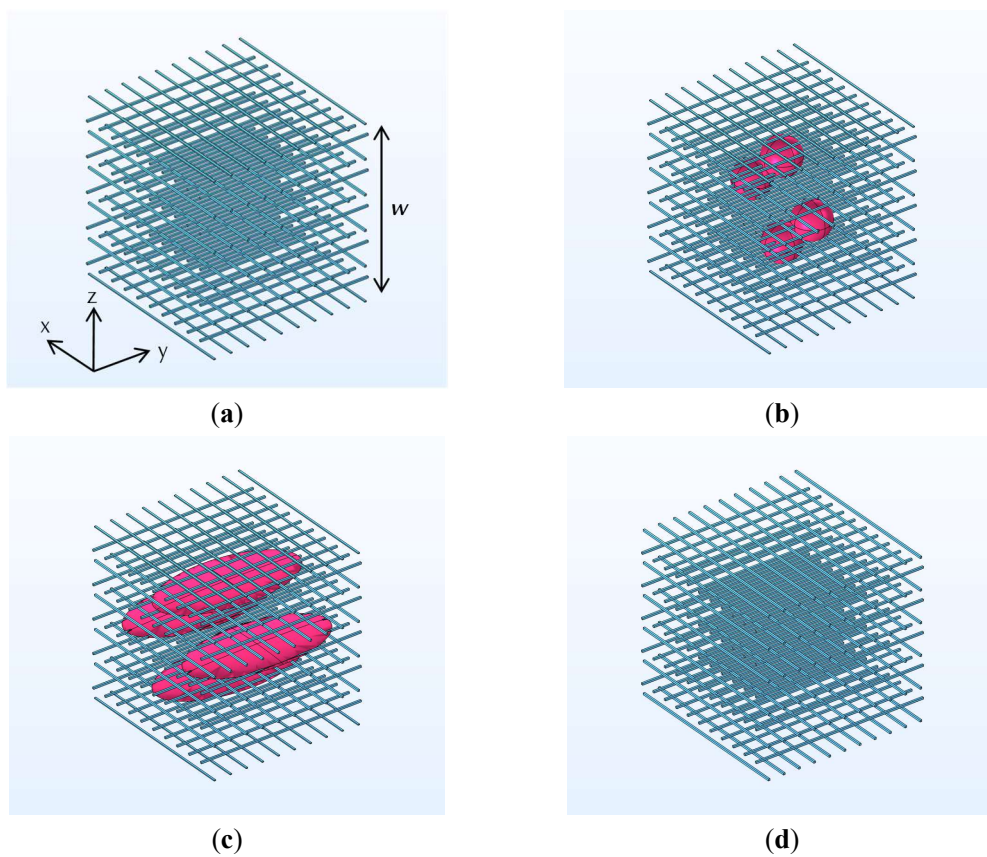
Figure 4-4. Computational geometry: (a) non-woven fabric 1; (b) composite 1 (particle A mixed non-woven fabric); (c) composite 2 (particle B mixed non-woven fabric); (d) non-woven fabric 2.

Table 4-1. Calculation conditions.

	Fiber Diameter (µm)	Density of Fiber (g/cm³)	Density of Particle (g/cm³)	Bulk Density (kg/m³)	Particle Content (wt%)	Particle Shape/pcs.	Center of Gravity (x,y,z)
Non-woven fabric 1 Figure 3a	10	1.38	-	13.8	-	-/0	-
Composite 1 Figure 3b	10	1.38	0.15	16.8	19.5	Particle A /4	(250,500,500) (750,500,500) (500,500,250) (500,500,750)
Composite 2 Figure 3c	10	1.38	0.15	16.8	19.5	Particle B /4	(250,500,500) (750,500,500) (500,500,250) (500,500,750)
Non-woven fabric 2 Figure 3d	10	1.38	-	16.7	-	-/0	-

The predictive analysis of the sound absorption coefficient spectrum for a specimen thickness of 10 mm across 1/3-octave bands is illustrated in **Figure 4-5**. **Table 4-2** presents the results, showing average sound absorption coefficients derived from the spectra between 500–1600 Hz, 500–3150 Hz, and 1000–5000 Hz. The sound absorption spectra of non-woven fabric 1 and composite 1 were nearly identical. However, a divergence in sound absorption coefficients between non-woven fabric 1 and composite 2 became evident above 400 Hz, with composite 2 demonstrating enhanced sound absorption, particularly in the frequency band above 1000 Hz. This indicates that spherical particles in a non-woven fabric with a bulk density of approximately 13.8 kg/m³ and a particle content rate of about 20 wt% minimally affect the sound absorption coefficient. In contrast, the inclusion of elliptical flattened particles of equivalent weight and volume significantly improves sound absorption. This suggests that particle shape plays a crucial role in influencing the sound absorption coefficient.

Comparing non-woven fabric 2 and composite 2, composite 2 exhibited superior sound absorption, particularly in the higher-frequency range. It was observed that the inclusion of elliptical flattened particles may enhance the sound absorption effect relative to the weight, compared to materials composed solely of fibers. This improvement is believed to stem from the elliptical flattened particles

increasing the flow resistivity and tortuosity of the non-woven fabric, which in turn enhances sound absorption (**Figure 4-6**).
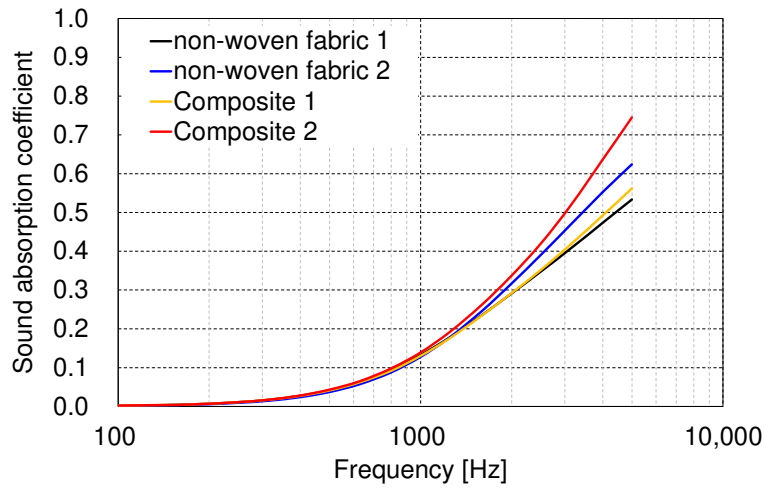
Figure 4-5. Spectra of predicted sound absorption coefficients of the computational geometry.

Table 4-2. Average sound absorption coefficient predicted from calculations.

Title 1	500–1600 Hz Average Sound Absorption Coefficient	500–3150 Hz Average Sound Absorption Coefficient	1000–5000 Hz Average Sound Absorption Coefficient
Non-woven fabric 1	0.12	0.20	0.33
Composite 1	0.12	0.20	0.33
Composite 2	0.13	0.23	0.41
Non-woven fabric 2	0.12	0.21	0.36
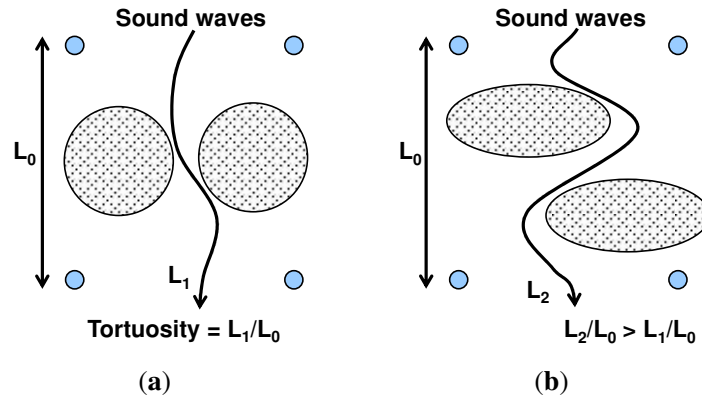
Figure 4-6. Shape of mixed aerogel particles and tortuosity inside the porous material: (a) Spherical particles; (b) Elliptical flattened particles.

3.2 Performance Evaluation Result

Based on the calculation results from Section 3.1, we developed a technique to blend flattened aerogel particles oriented against the thickness direction and fabricated aerogel particle-mixed non-woven fabric. Specifically, while producing thin non-woven fabrics using a carding machine, we laid flattened aerogel particles onto these thin fabrics and then laminated them to create non-woven fabrics with the particles aligned along the thickness direction.

Figure 4-7 presents photographs of test specimens: PET non-woven fabric with a bulk density of 16.2 kg/m^3, PET non-woven fabric with a bulk density of 87.2 kg/m^3, and Thinsulate, a commonly used automotive sound-absorbing material composed of the fabricated non-woven fabric and the aerogel particle-mixed non-woven fabric. The particle content of the aerogel particle-mixed non-woven fabric was approximately 21.7 wt%, closely matching the 19.5 wt% particle content of particles A and B used in the calculation geometry.

Figure 4-8 displays the results from the CT analysis of the internal structure of the PET non-woven fabric 1 and the aerogel particle-mixed non-woven fabric, examining fiber-to-fiber distances and particle size distribution. PET non-woven fabric 1, with a bulk density of 16.2 kg/m^3, showed a peak

distribution of the distance between fibers at about 30 µm. However, the aerogel particle-mixed non-woven fabric, with a bulk density of 87.2 kg/m^3, also showed a peak at 30 µm but with fiber distances extending up to 180 µm, indicating wider inter-fiber spacing in areas where particles are present. The median particle diameter, calculated from particle volume assuming a spherical shape, was about 240 µm (particle volume: approximately 7.24×10^6 µm^3). This volume is closely aligned with the volume of particles A and B used in the calculation geometry, which is 5.58×10^6 µm^3 (particle diameter: 220 µm).
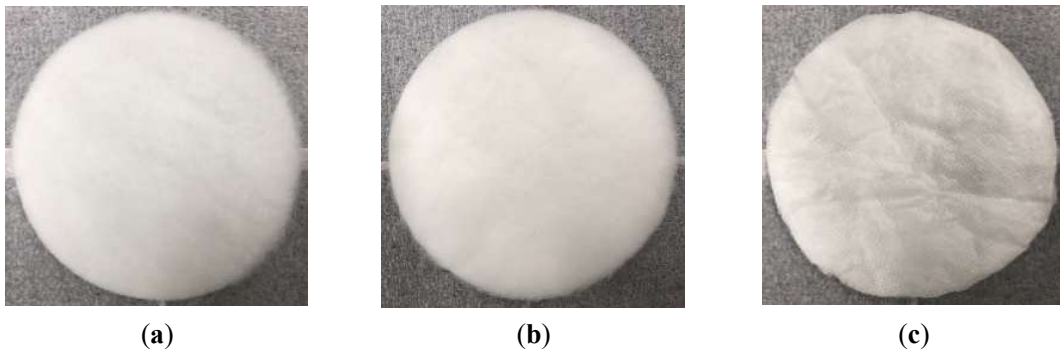
Figure 4-7. External appearance of non-woven fabric: (a) polyethylene terephthalate (PET) non-woven fabric 1; (b) particle-mixed non-woven fabric; (c) Thinsulate.

(a)

75
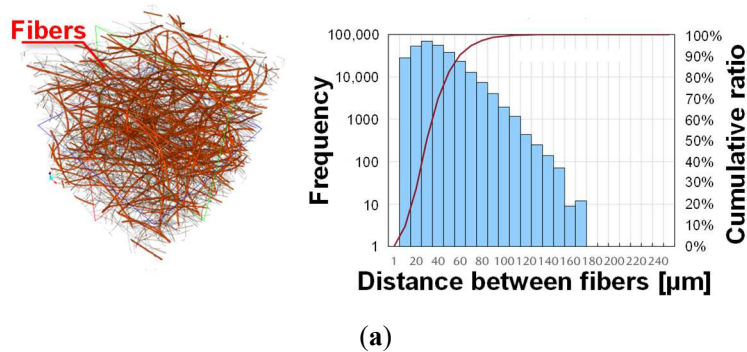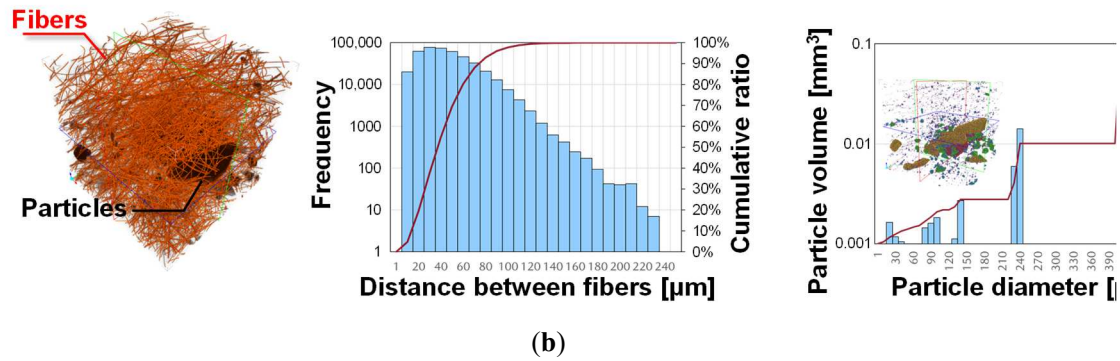
Figure 4-8. Distance between fibers of non-woven fabric and particle size distribution of mixed aerogel particles: (a) PET non-woven fabric 1; (b) particle-mixed non-woven fabric.

The measured sound absorption coefficients of PET non-woven 1 and PET non-woven 2, with bulk densities of 16.2 and 100.5 kg/m^3, respectively, and of aerogel particle-mixed non-woven fabric, with a bulk density of 87.2 kg/m^3, and of Thinsulate are shown in **Figure 4-9**. PET non-woven fabric 2 demonstrated a higher sound absorption coefficient across a broader frequency range of 100–1600 Hz compared to PET non-woven fabric 1. Additionally, there was no reduction in sound absorption coefficient at higher frequencies up to 1600 Hz.

From this, we conclude that PET non-woven fabric is effective in improving the sound absorption coefficient below 1600 Hz for bulk densities up to 100.5 kg/m^3. Conversely, the non-woven fabric mixed with aerogel particles demonstrates a higher sound absorption coefficient across most frequency bands of 100–1600 Hz than the PET non-woven fabric 2 with a bulk density of 100.5 kg/m^3, despite having a lower bulk density of 87.2 kg/m^3. This indicates that the aerogel particles contribute to enhancing the sound absorption coefficient.
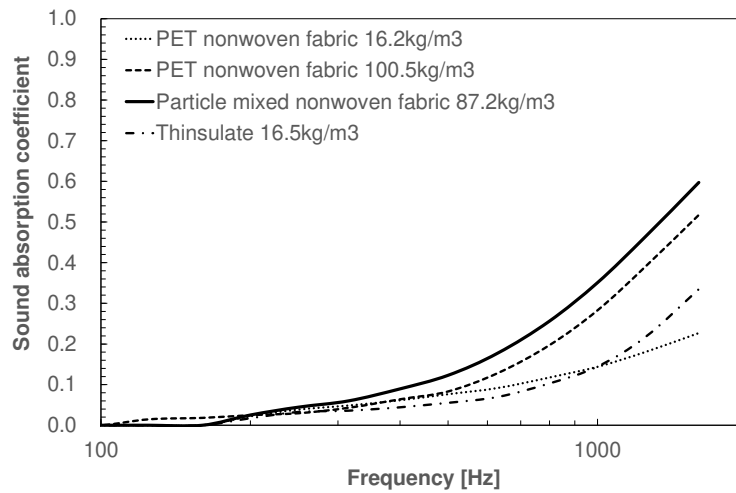
Figure 4-9. Measured normal-incidence sound absorption coefficients of particle-mixed non-woven fabric.

Figure 4-10 displays the sound absorption coefficient measurements for a test specimen of the same shape, where a skin material with high airflow resistance was laminated on one side of the prepared non-woven fabric. Like the PET non-woven fabric, the aerogel particle-mixed non-woven fabric also showed an improvement in sound ab-sorption coefficient, as predicted by the Biot model. Therefore, we deduce that the sound absorption mechanism of non-woven fabrics mixed with aerogel particles aligns with Biot's theory.

Table 4-3 presents the average sound absorption coefficient in the 500–1600 Hz range and the measured flow resistivity, which are critical in automotive noise reduction for enhancing speech clarity. In this PET non-woven fabric, the airflow resistance increases with increasing bulk density up to 100.5 kg/m^3, and correspondingly, the average sound absorption coefficient in the 500–1600 Hz range also increases. However, the aerogel particle-mixed non-woven fabric exhibits a higher average sound absorption coefficient in the 500–1600 Hz range than PET non-woven fabric 2, despite its lower airflow resistance. The lack of peaks at specific frequencies in the sound absorption spectrum of the aerogel particle-mixed non-woven fabric in **Figure 4-9** suggests that inertia and viscoelastic loss of

solids are unlikely to influence the results. From these observations, we infer that the inclusion of aerogel particles enhances the tortuosity, viscous characteristic length, or thermal characteristic length, thereby improving the sound absorption coefficient. The average sound absorption coefficient in the range of 500–1600 Hz was about 2.8 times higher than that of Thinsulate in the specimen made of non-woven fabric mixed with aerogel particles and laminated with a skin material with high airflow resistance.
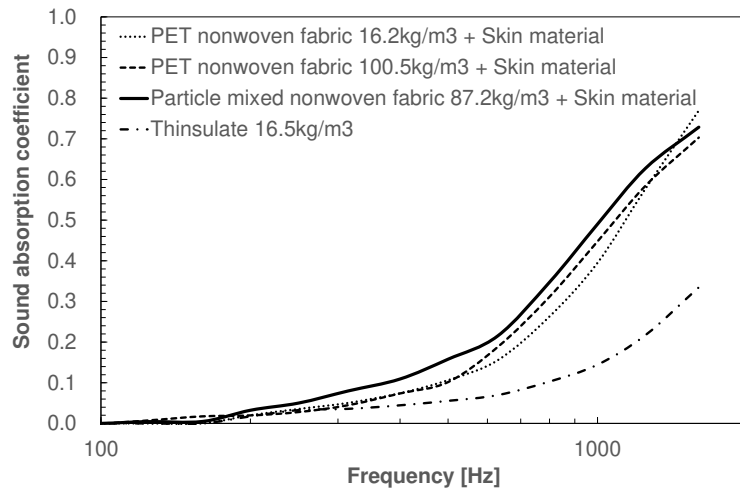
Figure 4-10. Measured normal-incidence sound absorption coefficients of particle-mixed non-woven fabric + skin material.

Table 4-3. Properties of particle-mixed non-woven fabric.

	Bulk Density of Non-Woven Fabric (kg/m³)	Thickness (mm)	500–1600 Hz Average Sound Absorption Coefficient	W/Skin Material 500–1600 Hz Average Sound Absorption Coefficient	Airflow Resistance @0.5 mm/s (Pa·s/m)
PET non-woven fabric 1	16.2	10.1	0.14	0.38	102
PET non-woven fabric 2	100.5	10.3	0.27	0.39	1500
Particle-mixed non-woven fabric	87.2	10.0	0.33	0.43	1200
Thinsulate	16.5	10.0	0.15	-	-

The thermal conductivities of PET non-woven fabric 1, PET non-woven fabric 2, and non-woven fabric mixed with aerogel particles as well as the thermal conductivity measured when the bulk density is altered by compressing the non-woven fabric within a steady-state thermal conductivity measurement device are presented in **Figure 4-11**. PET non-woven fabric reaches a thermal conductivity of about 0.029 W/(m·K) even when the bulk density is increased to approximately 130 kg/m^3. Conversely, the non-woven fabric mixed with aerogel particles exhibited a thermal conductivity of about 0.026 W/(m·K), confirming that the aerogel particles enhance the thermal insulation properties of the aerogel particle-mixed non-woven fabric as intended. Compared to Thinsulate, the thermal insulation property of the aerogel particle-mixed non-woven fabric was approximately 1.4 times higher.
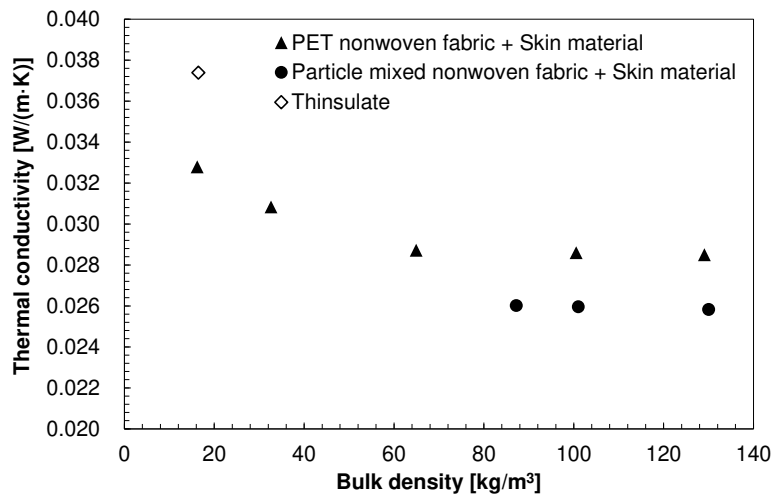
Figure 4-11. Measured thermal conductivity of particle-mixed non-woven fabric + skin material.

4. Conclusions

We developed a non-woven fabric mixed with aerogel ellipsoidal particles that significantly enhances acoustic properties. The thermal conductivity of this material was equivalent to still air (0.026 W/(m·K)), and the average sound absorption coefficient of this material at 500–1600 Hz at a

thickness of 10 mm was more than twice that of Thinsulate, a common sound-absorbing material for automobiles. When applied throughout a vehicle's interior, this material is expected to reduce noise by approximately 40% and improve fuel efficiency by around 4% due to a roughly 30% reduction in energy consumption for air conditioning, although the total weight of the sound-absorbing and thermal-insulating materials may increase.

The porous material with fine porous and soft sites described in Chapter 3 exhibited excellent heat insulation and sound absorption properties but were brittle and prone to damage. Consequently, their use in automobiles was restricted to locations not exposed to physical stresses. The new aerogel particle-mixed non-woven fabric integrates nanoporous ellipsoidal particles, with long sides ranging from tens to hundreds of microns, into non-woven fabrics with voids of similar dimensions. This composition enhances its resistance to shock and vibration. Additionally, the application of a skin material reduces particle shedding, allowing its use in parts exposed to harsh conditions including external areas and drive units.

5. References

[1] Shrestha, S.S.; Tiwari, J.; Rai, A.; Hun, D.E.; Howard, D.; Desjarlais, A.O.; Francoeur, M.; Feng, T. Solid and gas thermal conductivity models improvement and validation in various porous insulation materials. Int. J. Therm. Sci. 2023, 187, 108164.

[2] Zhou, Y.; Huang, B.; Cao, B.-Y. Vibrational modes with long mean free path and large volumetric heat capacity drive higher thermal conductivity in amorphous zeolitic imidazolate Framework-4. Mater. Today Phys. 2021, 21, 100516.

[3] Qiu, B.; Bao, H.; Zhang, G.; Wu, Y.; Ruan, X. Molecular dynamics simulations of lattice thermal conductivity and spectral phonon mean free path of PbTe: Bulk and nanostructures. Comput. Mater. Sci. 2012, 53, 278–285.

[4] Gao, K.; van Dommelen, J.A.W.; Geers, M.G.D. Investigation of the effects of the microstructure on the sound absorption performance of polymer foams using a computational homogenization approach. Eur. J. Mech. A Solids 2017, 61, 330–344.

[5] Gao, K.; van Dommelen, J.A.W.; Göransson, P.; Geers, M.G.D. A homogenization approach for characterization of the fluid–solid coupling parameters in Biot's equations for acoustic poroelastic materials. J. Sound. Vib. 2015, 351, 251–267.

[6] Zieliński, T.G. Microstructure-based calculations and experimental results for sound absorbing porous layers of randomly packed rigid spherical beads. J. Appl. Phys. 2014, 116. https://doi.org/10.1063/1.4890218.

[7] Perrot, C.; Chevillotte, F.; Tan Hoang, M.; Bonnet, G.; Bécot, F.-X.; Gautron, L.; Duval, A. Microstructure, transport, and acoustic properties of open-cell foam samples: Experiments and three-dimensional numerical simulations. J. Appl. Phys. 2012, 111. https://doi.org/10.1063/1.3673523.

[8] Lee, C.-Y.; Leamy, M.J.; Nadler, J.H. Frequency band structure and absorption predictions for multi-periodic acoustic com-posites. J. Sound. Vib. 2010, 329, 1809–1822.

[9] Wu, C.M.; Chou, M.H. Polymorphism, piezoelectricity and sound absorption of electrospun PVDF membranes with and without carbon nanotubes. Compos. Sci. Technol. 2016, 127, 127–133.

[10] Shen, L.; Zhang, H.; Lei, Y.; Chen, Y.; Liang, M.; Zou, H. Hierarchical pore structure based on cellulose nanofiber/melamine composite foam with enhanced sound absorption performance. Carbohydr. Polym. 2021, 255, 117405.

[11] Zhao-Xuan, D.; Ying, W. Optimization and characterization of polyurethane electro-spun nano-membranes used for the surfaces of sound absorbent multi-layer sheets. J. Macromol. Sci. B 2021, 60, 647–662.

[12] Neslihan, K.; Ilkay, O.Y.; Nuray, U.; Aysen, O.; Cafer, K. Sound absorption and thermal insulation properties of composite thermoplastic polyurethane/polystyrene (TPU/PS) nanofiber web and TPU nanofiber web and PS-extracted TPU/PS microfiber web. J. Ind. Text. 2022, 51, 7963S–7982S.

[13] Davoudabadi Farahani, M.; Jamshidi Avanaki, M.; Jeddi, A.A. Sound absorption of warp knitted spacer fabrics based on knit structure and nanofiber enhancement. J. Ind. Text. 2022, 51, 1539–1557.

[14] Yan, P.; Zhou, B.; Du, A. Synthesis of polyimide cross-linked silica aerogels with good acoustic performance. RSC Adv. 2014, 4, 58252–58259.

[15] Sachithanadam, M.; Joshi, S.C. Effect of granule sizes on acoustic properties of protein-based silica aerogel composites via novel inferential transmission loss method. Gels 2016, 2, 11.

[16] Merli, F.; Anderson, A.M.; Carroll, M.K.; Buratti, C. Acoustic measurements on monolithic aerogel samples and application of the selected solutions to standard window systems. J. Appl. Acoust. 2018, 142, 123–131.

[17] Oh, K.W.; Kim, D.K.; Kim, S.H. Ultra-porous flexible PET/Aerogel blanket for sound absorption and thermal insulation. Fibers Polym. 2009, 10, 731–737.

[18] Küçük, M.; Korkmaz, Y. The effect of physical parameters on sound absorption properties of natural fiber mixed nonwoven composites. Text. Res. J. 2012, 82, 2043–2053.

[19] Motahari, S.; Javadi, H.; Motahari, A. Silica-aerogel cotton composites as sound absorber. J. Mater. Civ. Eng. 2015, 27, 04014237.

[20] Ramamoorthy, M.; Pisal, A.; Rengasamy, R.; Rao, A.V. In-situ synthesis of silica aerogel in polyethylene terephthalate fibre nonwovens and their composite properties on acoustical absorption behavior. J. Porous Mater. 2018, 25, 179–187.

[21] Yang, T.; Xiong, X.; Venkataraman, M.; Mishra, R.; Nov, J.; Militký, J. Investigation on sound absorption properties of aero-gel/polymer nonwovens. J. Text. I 2019, 110, 196–201.

[22] Talebi, Z.; Soltani, P.; Habibi, N.; Latifi, F. Silica aerogel/polyester blankets for efficient sound absorption in buildings. Constr. Build. Mater. 2019, 220, 76–89.

[23] Mazrouei-Sebdani, Z.; Begum, H.; Schoenwald, S.; Horoshenkov, K.V.; Malfait, W.J. A review on silica aerogel-based materials for acoustic applications. J. Non-Crystal Solids 2021, 562, 120770.

[24] D. Katsura; T. Yamamoto; K. Yamakawa; N. Hatakeyama; R. Miura; J. Okajima; K. Inaba; Y. Ishizawa; H. Ochiai; H. Yukawa; K. Murashige; J. Katagihara; J. Tomotsu; T. Ishimoto; J. Ohshita. Development of thermal management and noise/vibration control material model technology by model-based research (MBR); 1st report JSAE Annual Congress (Spring) proceedings, 2021; p. 20215301.

[25] K. Yamakawa; T.Yamamoto; D. Katsura; M. Inoue; N. Hatakeyama; R. Miura; J. Okajima; K. Inaba; Y. Ishizawa; H. Yukawa; H. Ito; T. Ishimoto; J. Ohshita. Development of Vibration Control Material Model Technology by Model Based Research (MBR). Transactions of the Society of Automotive Engineers of Japan, 2022, Volume 53, Issue 5, Pages 886-891.

[26] D. Katsura; K. Yamakawa. Development of flow resistance control technology for sound absorbing material surface by model-based research (MBR); JSAE Annual Congress (Spring) proceedings, 2023; p. 20235296.

[27] ISO 10534-2:2023; Acoustics—Determination of Acoustic Properties in Impedance Tubes—Part 2: Two-Microphone Technique for Normal Sound Absorption Coefficient and Normal Surface Impedance. International Organization for Standardization: Geneva, Switzerland, 2023.

[28] ISO 9053-1:2018; Acoustics—Determination of Airflow Resistance—Part 1: Static Airflow Method. International Organization for Standardization: Geneva, Switzerland, 2018.

[29] ISO 8301:1991; Thermal Insulation—Determination of Steady-State Thermal Resistance and Related Properties—Heat Flow Meter Apparatus. International Organization for Standardization: Geneva, Switzerland, 1991.

Chapter 5: Conclusion

In this thesis, the author has developed an innovative porous material with both high thermal insulation and high sound absorption properties to achieve carbon neutrality, one of the most important challenges in the automotive industry. It is recognized that both sound absorption and thermal conductivity depend on the internal structure of the material. In general, high-performance thermal insulation porous materials require the space of the fluid phase to be narrow to suppress heat conduction in gases. On the other hand, the fluid phase space is too narrow for sound waves to penetrate, so it cannot function as a sound-absorbing material. Therefore, achieving both high thermal insulation and high sound absorption in the same material using the conventional approach is difficult. Therefore, the author devised a structure in which sound waves do not need to penetrate the porous material, and sound absorption occurs only when sound waves collide with the porous material. The author also devised a structure in which the space inside the porous material is divided into spaces through which sound waves cannot penetrate and spaces through which they can. The space through which sound waves cannot penetrate is used to create thermal insulation properties, and the space through which sound waves can penetrate is used to create sound absorption properties by complicating the pathways. In order to efficiently confirm the effectiveness of the devised structure, as the fundamental technologies, the author has developed a technology for analyzing the low specific gravity and fine three-dimensional structure inside materials and quantitatively analyzing the characteristics of the structure, which has been difficult in the past, and a technology for calculating the sound absorption coefficient and thermal conductivity of porous materials based on the three-dimensional structure inside the materials. By utilizing the fundamental technologies, the author has efficiently developed a high-performance thermal-insulating and sound-absorbing porous material with the target performance.

Specifically, Chapter 1 provides an overview of previous studies on thermal-insulating and sound-absorbing materials to clarify the purpose of this paper.

In Chapter 2, the author described a new method to enhance the contrast of X-ray CT images of organic polymer materials. The author confirmed that gamma-ray irradiation of poly (ethylene terephthalate) (PET) fibers in dichloromethane containing 2-bromoethyl methacrylate, 2-chloroethyl methacrylate, or 4-bromostyrene results in the grafting of halogen-containing oligomeric chains onto the PET fibers. Focused ion beam scanning electron microscopy (FIB-SEM) and time-of-flight secondary ion mass spectrometry (TOF-SIMS) analyses revealed a homogeneous distribution of bromine atoms within the 2-bromoethyl methacrylate-modified PET fibers, not only on the surface. This uniform incorporation translated to a significant improvement in X-ray CT image contrast compared with pristine fibers. Similar treatment of polypropylene pellets also enhanced the contrast of their X-ray CT images. This is a new simple and effective method to enhance the X-ray CT image contrast and potentially applicable to various polymer materials including polymer composites and porous polymer materials, readily allowing the observation of their 3D microstructures finely.

In Chapter 3, the author described a new porous material that absorbs sound waves without requiring sound waves to penetrate the porous material; sound waves simply impinge on the porous material. By applying computational microstructure modeling to porous materials, it was clear that the sound absorption performance can be improved by increasing the resonance amplitude of the ligament (solid phase) and amplifying the viscous damping at the boundary between the fluid and solid phases. This confirmed the concept of a sound absorption mechanism without sound wave penetration. A hydrophobic cellulose nanofiber–poly(methylsiloxane) xerogel composite was fabricated to resemble the microstructure and Young's modulus of the calculated model. The porous material was found to have both high sound absorption in the frequency range above 1000 Hz (sound absorption coefficient of above 0.44) and high thermal insulation equivalent to still air (0.026 W/(m·K)). This material can

be used in unexposed parts, such as the inside of interior parts of automobiles, and demonstrates excellent sound absorption and thermal insulation properties. In addition, the material may be strengthened by improving the interaction or inter-dispersion between the PMS framework and CNFs. A tougher version of this material can be used in the parts subjected to harsh conditions in the future, such as prime movers and automobile drive units.

In Chapter 4, the author described a new porous material in which the space inside the porous material is divided into spaces through which sound waves cannot penetrate and spaces through which they can. The space through which sound waves cannot penetrate is used to create thermal insulation properties, and the space through which sound waves can penetrate is used to create sound absorption properties by complicating the pathways. In this material, the thermal insulation property was created by particles with nano-porosity through which sound waves cannot penetrate, and the sound absorption property was created by making other spaces where sound waves can penetrate. By making the particles flat, the path of the space through which sound waves can penetrate is extended in a complex manner, thereby improving sound absorption. This mechanism was confirmed by applying computational microstructure modeling to porous materials and changing the shape of the composite particles. A non-woven fabric composed of flattened ellipsoidal particles with nano-porosity was fabricated to resemble the microstructure of the calculated model. Furthermore, it was confirmed that the sound absorption coefficient was improved by laminating this porous material with a high-airflow-resistance skin material (thickness: 0.20 mm). This porous material laminated with the high-airflow-resistance skin material was found to have both high sound absorption in the frequency range above 1000 Hz (sound absorption coefficient of above 0.5) and high thermal insulation equivalent to still air (0.026 W/(m·K)), achieving the target performance. The porous material with fine porous and soft sites described in Chapter 3 exhibited excellent heat insulation and sound absorption properties but were brittle and prone to damage. Consequently, their use in automobiles was restricted to locations

not exposed to physical stresses. This non-woven fabric composed of flattened ellipsoidal particles with nano-porosity integrates nanoporous ellipsoidal particles, with long sides ranging from tens to hundreds of microns, into non-woven fabrics with voids of similar dimensions. This composition enhances its resistance to shock and vibration. Additionally, the application of a skin material reduces particle shedding, allowing its use in parts exposed to harsh conditions including ex-ternal areas and drive units.

From the above, by utilizing the developed fundamental technologies, the author has efficiently developed these high-performance thermal-insulating and sound-absorbing porous materials. When applied throughout a vehicle's interior, these materials are expected to reduce noise by approximately 40% and improve fuel efficiency by around 4% due to a roughly 30% reduction in energy consumption for air conditioning, although the total weight of the thermal-insulating and sound-absorbing materials may increase. The establishment of technology for mass production of these materials is expected to expand their application in the automotive industry. In addition, not only the automotive industry, but also various industries such as transportation (railroads, aircraft, etc.), living spaces, home appliances, and medical care, are working to achieve a higher level of compatibility between carbon neutrality and improved safety and comfort, and solving the problems of energy conservation and noise has become one of the most important issues in modern society. These porous materials have the potential to help solve problems in these industries, and the application of these materials is expected to expand in the future. Finally, the developed fundamental technologies can be utilized without the need for a special computing environment or skills, making it a highly versatile technology that can be put to practical use at the development sites of small and medium-sized component manufacturers. Educational activities for local manufacturers in these fundamental technologies are already underway through the Digital Manufacturing Education and Research Center. The author expects that these fundamental technologies will be utilized by these

manufacturers in the future and that these manufacturers will continuously create innovative

technologies to achieve carbon neutrality.

List of publications

1. T. Nakaya; <u>D. Katsura</u>; K. Kawakami; K. Komaguchi; Y. Adachi; E. Tanabe; J. Ohshita. Gamma-ray-induced modification of poly(ethylene terephthalate) and polypropylene solid materials with halogen-containing olefins for X-ray CT image contrast enhancement. Journal of Applied Polymer Science. (Chapter 2)

2. <u>D. Katsura</u>; T. Maeda; K. Kanamori; T. Yamamoto; J. Ohshita. Sound-Absorbing, Thermal-Insulating Material Based on Poly(methylsiloxane) Xerogel and Cellulose Nanofibers. Appl. Sci. 2024, Volume 14, Issue 6, 2570. (Chapter 3)

3. <u>D. Katsura</u>; H. Ochiai; M. Kawabe; T. Yamamoto; J. Ohshita. Sound-Absorbing, Thermal-Insulating Material Based on Non-Woven Fabrics Mixed with Aerogel Particles. Appl. Sci. 2024, Volume 14, Issue 13, 5368. (Chapter 4)

This doctoral thesis includes contents reproduced from the papers listed above with permission of the publishers.

Acknowledgments